INTERFACES AT CRYSTALLINE METAL GATE/HIGH-*K* OXIDE/SI STACKS: CHARACTERIZATIONS AND ATOMISTIC MODELING

DONG YUFENG

NATIONAL UNIVERSITY OF SINGAPORE

2006

INTERFACES AT CRYSTALLINE METAL GATE/HIGH-*K* OXIDE/SI STACKS: CHARACTERIZATIONS AND ATOMISTIC MODELING

DONG YUFENG

(B. Sc., M. Sc., Chongqing Univ.)

A THESIS SUBMITTED

FOR THE DEGREE OF DOCTOR OF PHILOSOPHY

DEPARTMENT OF PHYSICS

NATIONAL UNIVERSITY OF SINGAPORE

Acknowledgements

I would like to thank my advisor **Prof. Feng Yuan Ping** for providing me the opportunity to have an adventure into the world of atomistic modeling. He not only taught me nearly everything I know about first-principles calculations but also shared with me his wisdom, insight and humor throughout these years. It has been a great life experience to study under his guidance.

I would like to thank my advisor **Dr. Wang Shijie** for his guidance, advice and kindness through my thesis work. He has taught me nearly all the hands-on experimental skills I have on XPS and TEM and always encouraged me to think independently. His enthusiasm to science and consistency to work will keep inspiring me in my future career.

I would also like to show my appreciation to my advisor **Prof. Alfred Huan** for the many invaluable discussions. His passion for the profession has been an inspiration.

Special thanks to **Li Qin** and **Mi Yanyu**, great partners to work with. I have enjoyed all the helpful discussions with them. They make my Ph.D career a happy memory.

Special thanks to the group members in Prof. Feng's group, **Dr. Huang Min, Zhao Fangfang, Dr. Sun Yiyang, Dr. Liu Lei, Pan Hui, Wu Rongqin, and Peng Guowen** for their valuable discussions and suggestions.

Special thanks to the staffs in MSCL cluster in IMRE for their support throughout the years: **Dr. Chai Jianwei, Dr. Pan Jisheng, Chow Shue Yin, and Zheng Yuebing**.

Many thanks to my parents for their unselfish love, support and many sacrifices throughout my life, which have made my education possible.

Finally, I would like to express my deep appreciation for my best friend and fiancée, **Qiu Yang** who has support my graduate study with her endless love.

Table of Contents

Abstract

The continual downscaling of semiconductor devices into the “nano” era requires not only the replacement of silicon dioxide (SiO_2) gate dielectric by high dielectric constant (high-*k*) materials, but also that of polycrystalline Si (poly-Si) gate electrodes by metal gates. In this work, characteristics of interfaces at crystalline metal/high-*k* oxide/silicon stacks have been studied by combinational methods of *x*-ray photoemission spectroscopy (XPS), high resolution transmission electron microscopy (HRTEM) and first-principles calculations based on density functional theory (DFT).

The epitaxial ZrO_2/Si (001) interface structure grown by pulsed laser deposition (PLD) was determined on atomic scale to be a high-symmetry cube-on-cube structure using HRTEM. The interface band alignment at the epitaxial ZrO_2/Si interface was accurately measured by XPS using a core-level-based method. Meanwhile, various interface structures based on the HRTEM images have been studied by first-principles calculations. The relative stability of the various structures was compared in terms of interface formation energy. The strain modes (free-standing and Si-substrate modes) effects and interface structure effects on band offsets were discussed. It was found that interface structures and band alignments are deposition-process-dependant, which gives explanations for the discrepancy in measured band alignments for different ZrO_2/Si stacks.

For the metal gate/high-*k* oxide interface, the effective work functions (WF) of metal gate were found to be tunable by controlling the interface structures or chemical species. In oxygen-rich or -deficient conditions, the variation of metal Ni effective WF

was found to be as large as 0.76 eV. The effects of interface chemical bonding on interface band alignments were demonstrated by both XPS measurements and first principles calculations. In addition, a novel method for chemical tuning of metal effective WF for the metal gate/high-*k* oxide interface was proposed. That is, a heterovalent metal interlayer was included between the metal gate and the high-*k* oxide. A tunability as wide as 2.8 eV was achieved for the effective WF which far exceeds the required tuning range. Furthermore, a general chemical tuning trend was established for most of the transition metals considered, that is, effective metal WF increases linearly with the electronegativity of the interfacial metal atom. The experimental results for Ni/Al/ZrO_2 interface are in good agreement with that from the theoretical predictions. The results provide a practical way of modifying the band alignments for metal gate/high-*k* oxide interfaces to satisfy the engineering requirement for the metal gate technology.

List of Tables

Chapter 3

Chapter 4

Chapter 5

List of Figures

Publications

1. **Y. F. Dong**, Y. Y. Mi, Y. P. Feng, A. C. H. Huan, and S. J. Wang, "*Ab initio* studies on Schottky barrier heights at metal gate/$LaAlO_3$(001) interfaces", *Appl. Phys. Lett.* (2006), accepted.
2. Q. Li, **Y. F. Dong**, S. J. Wang, A. C. H. Huan, J. W. Chai., Y. P. Feng, and C. K. Ong, "Evolution of Schottky barrier heights at Ni/HfO_2 interfaces", *Appl. Phys. Lett.* **88**, 222102 (2006).
3. **Y. F. Dong**, S. J. Wang, Y. P. Feng and A. C. H. Huan, "Chemical tuning of band alignments for metal gate/high-κ oxide interfaces", *Phys. Rev. B* **73**, 045302 (2006)**.**
4. S. J. Wang, J. W. Chai, **Y. F. Dong**, Y. P. Feng, J. S. Pan, and A. C. H. Huan, "Effect of nitrogen incorporation on the electronic structure and thermal stability of HfO_2 gate dielectric", *Appl. Phys. Lett.* **88**, 192103 (2006).
5. C. Liu, E. F. Chor, L. S. Tan, and **Y. F. Dong**, "Structural and electrical characterization of pulsed-laser-deposition-grown Sc_2O_3/GaN heterostructures", *Appl. Phys. Lett.* **88**, 222123 (2006).
6. **Y. F. Dong**, S. J. Wang, Y. Y. Mi, Y. P. Feng and A. C. H. Huan, "First-principles studies on the initial growth of Ni on MgO(001) surface", *Surf. Sci*. **600**, 2154 (2006).
7. **Y. F. Dong**, S. J. Wang, J. W. Chai, Y. P. Feng and A. C. H. Huan, "Impact of interface structure on Schottky-barrier height for Ni/ZrO_2(001) interfaces", *Appl. Phys. Lett.* **86**, 132103 (2005).
8. **Y. F. Dong**, Y. P. Feng, S. J. Wang and A. C. H. Huan, "First-principles study of ZrO_2 /Si interfaces: energetics and band offsets", *Phys. Rev. B* **72**, 045327 (2005).
9. S. J. Wang, **Y. F. Dong**, A. C. H. Huan, Y. P. Feng and C. K. Ong, "The epitaxial ZrO_2 on silicon as alternative gate dielectric: film growth, characterization and electronic structure calculations", *Mater. Sci. Eng. B* **118**, 122 (2005).
10. Y. Y. Mi, S. J. Wang, **Y. F. Dong**, J. W. Chai, J. S. Pan, A. C. H. Huan, and C. K. Ong. "Evolution of Fermi level and Schottky Barrier Height at Ni/MgO(001) interfaces", *Surf. Sci*. **599**, 255 (2005).
11. S. J. Wang, A. C. H. Huan, Y. L. Foo, J. W. Chai, J. S. Pan, Q. Li, **Y. F. Dong**, Y. P. Feng, and C. K. Ong, "Energy-band alignments at ZrO_2 / Si, SiGe, and Ge interfaces", *Appl. Phys. Lett.* **85**, 4418 (2004).

Chapter 1

Introduction

1.1 MOSFET scaling

Over the past 40 years, the semiconductor industry has witnessed phenomenal growth in productivity and performance. This improvement is primarily achieved by means of the scaling of semiconductor devices to ever smaller dimensions. The scaling of semiconductor devices follows the famous Moore's law, [1] which predicts that the number of components per chip doubles every eighteen months. However, in the past few years, traditional transistor and capacitor materials, silicon dioxide (SiO_2), and polycrystalline silicon (poly-Si) have been pushed to their fundamental material limits and further scaling cannot continue without the introduction of new materials. The gate dielectric in metal-oxide-semiconductor (MOS) devices has emerged as the most difficult challenges for future device scaling.[2]

The most important semiconductor device is the complementary metal-oxide-semiconductor (CMOS) field effect transistor (FET). However, the most serious scaling-related problems occur in the MOSFET stacks. That is for gate electrode (poly-Si) and the gate dielectric layer (SiO_2) between the gate electrode and the Si channel, as shown in Fig. 1.1. According to the latest International Technology Roadmap for Semiconductors (ITRS),[3] the next generation of Si-based MOSFETs will require gate dielectric layer with the thicknesses around 1.0 nm, both for the high performance logic applications (like microprocessors for personal computers) and low operation power logic applications (like wireless applications). With present advanced technology to grow ultrathin SiO_2 film on Si with high quality SiO_2-Si interfaces,

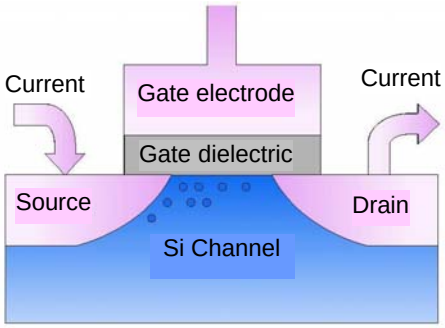

Fig. 1.1 Schematic diagram of a metal-oxide-semiconductor field effect transistor (MOSFET). The source and drain are connected by applying a bias to the gate causing a Si surface inversion layer through which current can flow.

there appears to be no reason why 1.0 nm SiO_2 cannot be manufactured.[4] However, the problem arising from the scaling of the SiO_2 layer thickness mainly concerns the leakage current flowing through the MOS structures. It is now clear that in the ultrathin SiO_2 gate layers (thickness typically below 2.0 nm), charge carriers can flow through the gate dielectrics by a quantum mechanical direct tunneling mechanism,[5] as shown in Fig. 1.2. The tunneling probability increases exponentially as the thickness of the SiO_2 layer decreases. This results in a large increase of the leakage current flowing through the gate dielectric layer as its thickness decreases to below 2 nm. For example, the leakage current density exceeds 100 A cm^{-2} at V_{OX}=1 V in a 1 nm thick SiO_2 layer (V_{OX} being the potential drop across the dielectric layer). [6] The leakage current specifications from ITRS requires that the minimum leakage current should be lower than 10 A cm^{-2} and 10^{-2} A cm^{-2} for high performance and low operation power devices respectively, which correspond to 1.6~1.4 nm thickness of SiO_2 for high performance circuits and 2.5~2.2 nm for low operating power circuits.

It is clear that the SiO_2 dielectric layer scaling is limited by the leakage current problem and it is an urgent task to introduce new dielectric material to replace SiO_2 as the gate dielectrics. [7, 8]

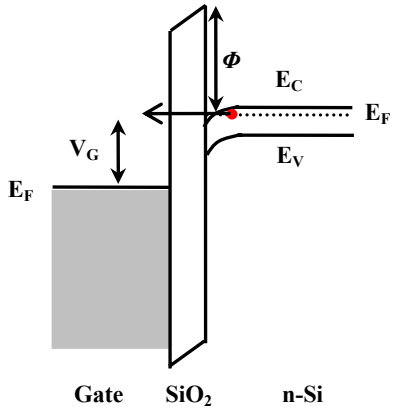

Fig. 1.2 Schematic energy band diagram of a metal gate/SiO_2/*n*-Si MOS structure, illustrating direct tunneling of electrons from the Si substrate to the gate by applying gate voltage V_G.

1.2 High-*k* dielectrics

The solution to the above scaling induced gate leakage current problem is to replace conventional SiO_2 gate dielectric layer by a new material with higher dielectric constant (high-*k*), which can offer thicker physical thickness while keeping the same gate capacitance. From an electrical point of view, the MOS structures behave like a parallel plate capacitor. Ignoring quantum mechanical and depletion effects from a Si substrate and poly-Si gate electrode, the capacitance of this parallel plate is given by

$$C = \frac{k\varepsilon_0 A}{t_{OX}} \tag{1.1}$$

where *k* is the relative dielectric constant of the gate dielectric material (3.9 for SiO_2), A is the area of the capacitor, and t_{OX} is the thickness of the dielectric. An increase in the gate dielectric capacitance will result in an increase of the drive current and thus improve the performance of MOSFET devices.[9] From Eq. (1.1), increasing C can be achieved by either decreasing t_{OX} or increasing *k*. While the former is prohibited by the factor that the SiO_2 layer thickness approaches it limit, the latter can be fulfilled by using a new insulator with a higher relative dielectric constant than SiO_2, or high-*k* material.

With the conventional SiO_2 gate dielectric replaced by high-*k* material, it is convenient to define an equivalent oxide thickness (EOT) and rewrite the expression of C in terms of EOT as

$$C = \frac{k_{SiO_2}\varepsilon_0 A}{EOT} \tag{1.2}$$

with EOT defined as $EOT = \frac{k_{SiO2}}{k_{high-k}} t_{high-k}$, k_{SiO_2} as the dielectric constant of SiO_2 (3.9), k_{high-k} as the dielectric constant of high-k material, and t_{high-k} as the thickness of the high-*k* material.

The benefit of using high-*k* materials is obvious: with thicker physical thickness (t_{high-k}) for the same EOT, the leakage current flowing through the device can be reduced by several orders of magnitude. However, the alternative high-*k* material that could replace SiO_2 as gate dielectric in advanced semiconductor technologies should satisfy a long list of requirements, [10, 11] *e.g.*: (i) a sufficiently large energy band gap and band offsets with Si, providing high energy barriers at the dielectric/Si interfaces, in order to reduce leakage current; (ii) good thermal stability in contact with Si, preventing the formation of a thick SiO_x interfacial layer and the formation of silicide layers; (iii) good quality interface with the Si channel, which means a low number of intrinsic defects at the dielectric/Si interfaces; (iv) good film morphology, avoiding the formation of polycrystalline films and grain boundaries; (v) compatibility with the fabrication process. With the criteria established above for the choice of high-*k* oxide, lists of possible candidates can now be introduced and discussed.

Intensive studies have been carried out to find the appropriate high-*k* dielectrics, either in amorphous phase or epitaxial on Si substrate to satisfy the above list of requirements. [12, 13, 14] For amorphous candidates, Al_2O_3, Y_2O_3, Pr_2O_3, ZrO_2, HfO_2,

$LaAlO_3$, and Zr and Hf silicates have been studied intensively. For example, Guha *et al.* [15] showed that Al_2O_3 gate oxide has a low leakage current and good thermal stability on Si. The only problem with Al_2O_3 is its low dielectric constant (~ 9). For Y_2O_3 gate oxide, Narayanan *et al.* [16] proved that a SiO_2 interfacial layer will form at Y_2O_3/Si interface during the post-growth annealing stage, which plus its relatively low *k* value (~15) made Y_2O_3 not an appropriate candidate for long-term solution. For the rest of the above promising amorphous candidates, *e. g.* Pr_2O_3, ZrO_2, HfO_2, and $LaAlO_3$, the major problems are related to the difficulties in keeping the material amorphous even after post-deposition high temperature processing, and growing very thin alternative gate dielectrics on silicon without the formation of substantial SiO_2 at the interface (subcutaneous oxidation) during deposition and without the need to cap the film *in situ* to prevent such SiO_2 formation upon air exposure after growth. The former, crystallization of amorphous dielectric layers, would create grain boundaries which serves as the fast paths for gate leakage current, and for oxygen and some dopant atoms diffusion into the gate dielectric and even MOSFET channel region, making the interface inhomogeneous; while the latter, formation of interfacial low-*k* layer, would increase the EOT and compromise the benefit using high-*k* dielectrics. One common way to keep the dielectric material amorphous is to add a good glass-former (such as SiO_2 and Al_2O_3) to those candidates, which will increase the crystallization temperature, but decrease the desired dielectric constant. For the suppression of the subcutaneous oxidation, only a few groups have reported the gate dielectrics on Si without substantial formation of interfacial low-*k* layer without capping the film before exposure to air.[17]

A totally different way to obtain the alternative high-*k* material is to grow crystalline dielectric oxide thin films epitaxially on Si substrate with no interfacial

low-*k* layer. As a layer-sequenced structure, the long-standing problem of growing a commensurate crystalline oxide interface with silicon was partially solved by the pioneering work of McKee *et al.* [18] In their endeavor, alkaline earth and perovskite oxides were grown in perfect registry on the (001) surface of silicon, totally avoiding the amorphous silica phase that normally forms when silicon is exposed to an oxygen containing environment. This ability to grow crystalline oxide on Si with an atomically sharp interface is of great importance. Especially with the continual scaling of MOS devices, an amorphous low-*k* interface layer (SiO_2 or metal silicate) between the high-*k* dielectric and Si channel will no longer be tolerable for long-run, and epitaxial crystalline metal oxide with atomically well-defined interface with Si will be required ultimately. For epitaxial crystalline high-*k* dielectric candidates, $SrTiO_3$ on silicon structure has attracted considerable attention because the small lattice mismatch (1.6%) ensures a good physical interface structure with no interfacial defects. [19] High quality epitaxial $SrTiO_3$ thin films have been successfully grown on Si(001) substrate using MBE methods. [20, 21] Unfortunately, the conduction band offset (CBO) between $SrTiO_3$ and Si was so small (~ 0.1 eV) [22] that the induced large leakage current will be too large to be acceptable.

Although the low electron barrier (CBO) for $SrTiO_3$/Si interface made $SrTiO_3$ an inappropriate candidate, other epitaxial metal oxide on Si structures have continually attracted intensive studies, because it may be a way to resolve the thermal stability problem related to amorphous high-*k* candidates, primarily owing to the commensurate physical correspondence of the epitaxial semiconductor/oxide interface without any defects.[23] In addition to the single crystalline $SrTiO_3$/Si structure, intensive studies have also been carried out to obtain epitaxial Zr or Hf oxides on Si because such materials satisfy the band offset requirements. Wang *et al.* [24, 25] have obtained a high

symmetry cube-on-cube ZrO_2/Si interface structure using pulsed laser deposition (PLD) method. Although the epitaxial interface structure is atomically sharp with no interfacial amorphous layer, there are still many dislocations at the interface to relax the lattice-mismatch induced interfacial stress. Epitaxial yttrium-stabilized HfO_2 thin films were also deposited on Si(001) by PLD method.[26] The epitaxial relationship is the same as that for ZrO_2/Si(001) interfaces obtained by Wang *et al.* [24, 25] However, the epitaxial HfO_2/Si interface is not atomically flat, suggesting possible interface reaction, and is far away from a high quality interface. Therefore, the atomic structure of metal oxide and Si interface remains to be understood, which is essential for the epitaxial growth of Zr or Hf oxides thin films on Si with high quality interface. [27, 28, 29]

1.3 Metal gates

For the gate electrode side, the conventional gate electrode material, poly-Si, which has been the workhorse in semiconductor gate technology for over 30 years, also faces challenge with the down-scaling of CMOS devices. [30, 31, 32] Poly-Si is a good metal for current generation CMOS devices, but it is not the best one. Its low charge carrier density near the gate electrode/dielectric interface (less than 10^{21} carriers per cm^3) gives rise to a depletion layer at the gate/dielectric interface under gate inversion condition, as shown in Fig. 1.3. This depleted layer (~ 0.4 nm in thickness) introduces an additional

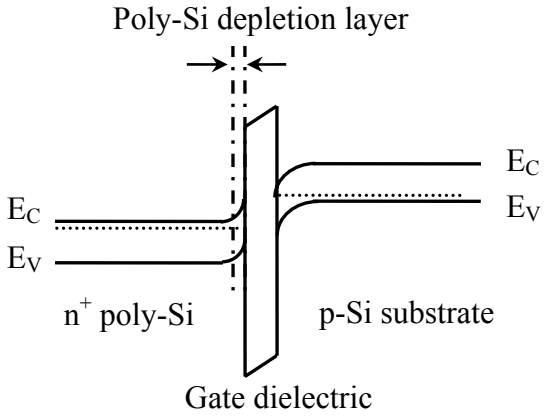

Fig. 1.3 Schematic energy band diagram of an N-MOS device showing the depletion layer in the poly-Si gate.

capacitance that is in series with the gate dielectric capacitance. This additional capacitance reduces the net gate capacitance and degrades short channel effects. This is intolerable for the coming sub-65 nm MOSFET because such a depletion layer will contribute to the increase of dielectric thickness and compromise the effort in the reduction of EOT. Therefore, it becomes essential to replace the poly-Si by new metal materials with higher charge carrier densities.[33] In addition to the gate depletion problem, it was found that poly-Si is not stable on high-*k* dielectric and the interface reaction can produce silicides, which compromise the work function and dielectric integrity of the gate stack.[34] Further more, it was reported that interfacial bonding (Si-metal bonds or oxygen vacancies) would pin the Fermi level at undesired energy positions.[35] For these reasons, it is necessary to investigate metal or metallic compounds as gate electrodes (metal gates) for MOSFET devices.

Candidate metal materials, or metal gates, to replace poly-Si as the gate electrodes[36] should have (i) tunable work functions; (ii) compatibility with the underlying dielectric material and (iii) high carrier concentrations. The latter two requirements are obvious. As for the work function requirement, gate electrodes for *n*-channel MOSFET (NMOS) and *p*-channel MOSFET (PMOS) devices must have work functions near Si conduction band edge (4.1 eV) and valence band edges (5.2 eV) respectively, in order to achieve optimum device performance for the conventional planar bulk CMOS devices. This requirement is easily fulfilled in poly-Si by an appropriate substrate and poly-Si gate doping, but has proved difficult to be met in case of metal gates.[37] Many promising metal gate electrode systems have been proposed, including elemental metals, metal alloys, metal nitrides, metal silicon nitrides, and metal silicides.

Refractory metal nitrides, tantalum nitride (TaN), hafnium nitride (HfN) and

titanium nitride (TiN) are considered promising for gate electrode application because of their excellent diffusion barrier properties and high melting point. But their effective work functions on high-*k* dielectric oxide were found to be pinned near the middle of Si band gap. [38] In addition, thermal stability studies of metal nitrides have revealed that a non-homogenous reaction layer is typically formed between the metal nitrides and the underlying dielectric at annealing temperature above 900^{o}C. [39] Due to these problems, approaches to stabilize metal nitrides have been evaluated. Suh *et al.* [40] found that TaN alloy can be further stabilized by the addition of silicon, forming metal silicon nitrides, which not only improves the diffusion barrier properties but also retards grain growth compared to TaN films. However, to achieve low work function for NMOS devices, Si content must be increased, which leads to the formation of high work function $TaSi_2$ during high temperature processing.[41] Such a dilemma requires the careful optimization of Si and N contents.

An alternate approach in obtaining low work function films for NMOS applications is by alloying element metals, for example, alloying low and high work function metals. This approach avoids the use of N, which can diffuse under high temperature processing, or Si, which can lead to the formation of di-silicides with large work functions. Matsukawa *et al.* [42] implemented the work function control of metal gate electrodes with Al-Ni alloys but found that the interdiffusion of Ni/Al stack would cause a significant inhomogeneity of work function. Misra *et al.* [43] obtained a non-linear relationship between work function and Ru-Ta along composition. The values of work function can be tuned from 4.2 to 5.0 eV, which makes it possible for this alloy to be used as gate electrode for both N- and P-MOSFET devices by controlling the alloy composition.

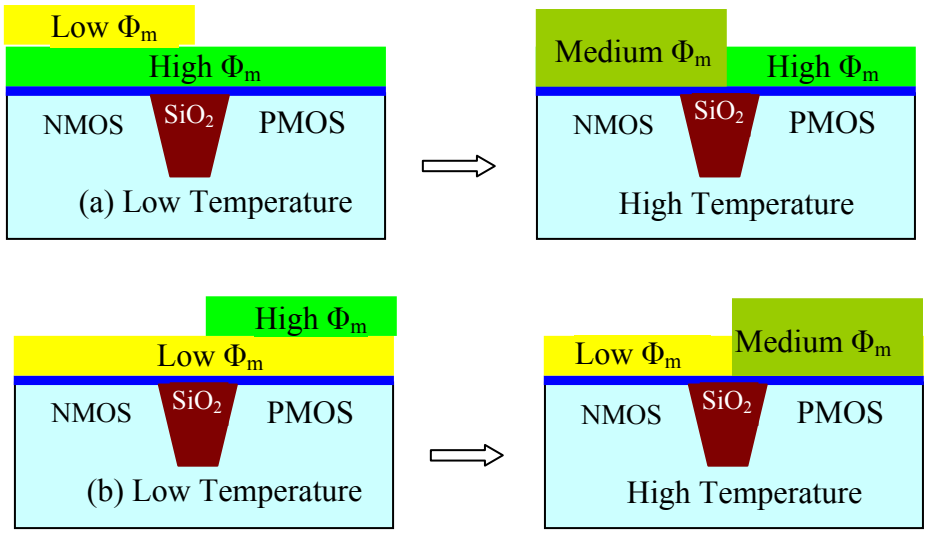

Fig. 1.4 Integrating approach for dual metal work function metal gate CMOS. (a) a high WF layer on the bottom and a low WF on top, whereas (b) the opposite approach.

Although materials with nearly correct vacuum work functions (WF) (~4.1 eV or ~ 5.2 eV) can be either synthesized as discussed above or simply selected from the periodic table, it is the integration of any two metals (one for PMOS and another for NMOS) in a CMOS fabrication flow that makes the application of metal gate so challenging. The most straightforward method of introducing two metals in a CMOS-integrated circuit is the dual metal gate process.[44] However, this approach exposes the gate dielectric to metal etchant which will cause damage and thinning on gate oxides. Therefore, intensive studies are being carried out to introduce dual work functions by manipulating the metal electrode interface in order to simplify integration. For instance, two different metal stacks and their interdiffusion have been investigated.[45] Two possible configurations of this metal interdiffusion approach are shown in Fig. 1.4. The proposed approach starts with deposition of low WF metal/high WF metal stacks. Then the top low WF metal layer is removed from the PMOS regions via etching. The following high temperature anneals are performed to produce a metal alloy layer above

the NMOS region, as shown in Fig. 1.4 (a). The Ta/Ru stacks with Ta as the top metal layer have been investigated by Lee *et al.* [46] Although the Ru-Ta alloy is stable with the underlying dielectric, the amount of work function tuning range (~0.4 eV) is insufficient for bulk CMOS devices. Lu *et al.* [47] also investigated the method to adjust the gate work function of an MOS structure by stacking two metals with different vacuum work functions. They demonstrated that metal/metal bilayer structure both on SiO_2 and HfO_2 dielectrics can be used to modulate the gate electrode work function over 1 eV range for a variety of metal stacks, Nb/W, Ti/W, and Ti/Pt, by controlling the thickness of the bottom metal layer. One interesting finding in Lu *et al.*'s work is that a thin bottom layer of ~1 nm is sufficient to change the work function from one metal to the other. This result is consistent with the *ab initio* simulations of bilayer stacks which shows that the transition of metal vacuum work function occurs over the first 1-3 monolayer. [48] However, there is no guarantee that the rule obtained from vacuum work function, the electron barrier between metal and vacuum, is directly applicable for Schottky barrier height, or effective work function, the electron barrier between metal and dielectrics. Actually, it was found that the effective work function of a metal depends on the underlying gate dielectrics and could differ appreciably from the metal work function in vacuum ($\Phi_{m,vac}$).[49] Experimental studies have indicated that metals with a tunable range of vacuum work function larger than the band gap of Si (1.12 eV) are necessary for effective integration of metal gates with high-*k* oxides. This result exasperates the selection and integration of metal gates.

In order to identify the right metal gate material and the alternative high-*k* dielectric, it is essential to understand and control the two interfaces at the atomic scale, the front interface between metal gate electrode and high-*k* dielectric and the back

interface between high-*k* dielectric and Si.

1.4 Band alignments at high-k oxide/Si and metal/high-k oxide interfaces

Band discontinuity is one of the most important parameters for semiconductor interfaces.[50, 51] The transport properties in heterojunctions devices are controlled by the electronic band profiles at the interfaces, namely the valence and conduction band offsets (VBO and CBO) in the case of semiconductor heterojunctions and the n-type (for electrons) and p-type (for holes) Schottky barrier heights (SBH) in the case of metal/semiconductor interfaces (see Fig. 1.5). Concerning the high-*k* dielectrics applications, the conduction and valence band offset between high-*k* oxide and Si channel should be larger than 1.0 eV, while the n-type SBH (for electrons) or effective work function of metal gate on high-*k* dielectrics between high-*k* oxide and metal gate electrodes (or effective work function of metal gate on high-*k* dielectrics) should be tunable to a range of ~ 1.1 eV (the magnitude of Si band gap).

1.4.1 Band offsets at high-*k* oxide/Si interfaces

The conduction (valence) band offset between the dielectric and Si channel acts as an electrical barrier for the electrons (holes) in Si channel and it should be large enough to minimize carrier injection into the conduction band states of the dielectric. Normally, a minimum requirement of 1.0 eV for CBO and VBO is needed and the high-*k* gate dielectric candidates with CBO or VBO smaller than 1.0 eV are not considered for further applications. However, many oxides with large dielectric constant have band gaps much smaller than 8.8 eV of silicon dioxide. How the oxide and silicon bands line up critically affects the capacitance-voltage characteristics and

transport properties of the MOS devices. So it is very important to accurately determine the band offsets for high-*k* dielectric materials on Si substrate.

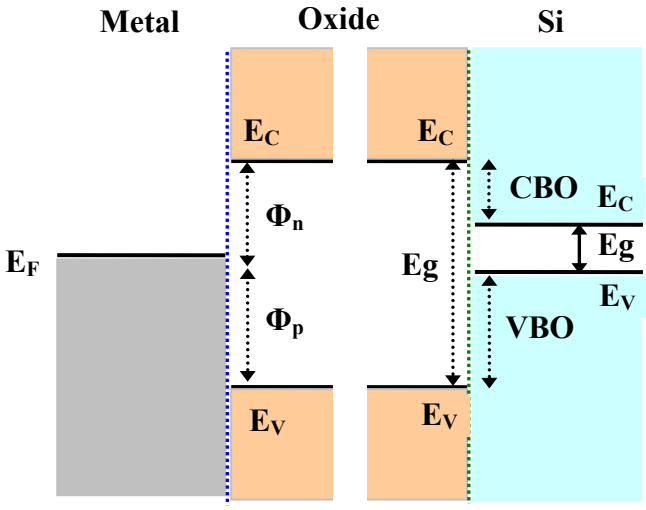

Fig. 1.5 Schematic band diagrams for metal/oxide/Si stacks. Definitions of band offsets (VBO and CBO) and of Schottky barrier heights (Φ_n and Φ_p) are shown.

Photoemission spectroscopy is a powerful local probe that has been used to determine reliable band offsets for numerous heterojunction systems in the past decades. Specially, a XPS core-level based method proposed by Kraut *et al.* [52] exploits the longer sampling depth of XPS (up to ~10 nm) while overcoming its limited experimental energy resolution as compared to synchrotron radiation photoemission techniques. Kraut's method has been widely used to accurately determine the valence band offset between ultrathin high-k dielectric film and Si substrate in the past few years. Chambers *et al.* [53] used the XPS core-level-based method to directly measure the valence band offset at epitaxial $SrTiO_3$/Si interfaces. They found that the entire band discontinuity lies at the valence band edge and the conduction band offset is very small that, far lower than the minimum requirement.

Their band offset measurement immediately precludes the possibility of applying $SrTiO_3$ as a high-*k* dielectric material if there were no further atomic-level band gap engineering method at the interface to equalize the valence and conduction band offsets.

The asymmetric distribution of band offsets (with the majority of discontinuity occurring at the valence band edges) is a main character for most high-*k* dielectric materials. For ultrathin ZrO_2 film on Si interfaces, Wang *et al.*[54,55] used x-ray photoemission method to measure the VBO to be ~3.0 eV, while the CBO is as small as ~1.7 eV. This result is close to that obtained by Miyazaki *et al.*[56] Puthenkovilakam and Chang[57] reported a more asymmetric distribution of band offsets for ultrathin ZrO_2 films grown by atomic layer deposition (ALD) method, with the magnitude of ~3.7 eV for VBO and only ~0.8 eV for CBO. Such low CBO (< 1.0 eV) indicates the limitation of ZrO_2 grown by the mentioned ALD method as an alternative high-*k* gate dielectrics. For ultrathin HfO_2 film on Si interfaces, the situation is similar because of the similar character of Zr and Hf. Using high-resolution angle-resolved photoelectron spectroscopy, Oshima *et al.*[58] determined the valence band offset for HfO_2/Si interfaces to be ~3.0 eV, versus ~ 1.7 eV for the conduction band offset. Alloying ultrathin Al and Hf oxide films (Hf-Al-O) on Si substrate strengthens the asymmetric distribution. For Hf-Al-O/Si interfaces, Jin *et al.*[59] obtained a valence band offset of 3.6 eV, versus ~ 1.3 eV for the CBO.

While the conduction band offsets for ZrO_2 and HfO_2 on Si seems large enough for high-*k* gate dielectric applications, the strong asymmetric distribution of band offsets for $SrTiO_3$/Si interfaces brings forward an important task, that is, how to fulfill the band gap engineering at the interfaces to obtain a positive, and large enough conduction band offset for $SrTiO_3$/Si interfaces. Theoretically, Först *et al.*[60]

demonstrated that atomic control of interfacial structures can improve the electronic properties of the interface to meet technological requirements. They increased the CBO of the $SrTiO_3$/Si interface from near zero to ~1.0 eV by controlling the chemical environment. This sizable change of CBO results from a local interface dipole formed by the interfacial polarized bonds. However, we noticed there may be a possible pitfall in Först's first-principles calculations, that is, the calculated VBOs did not include any many-body correction, which can be as high as 1.0 eV for metal oxide/Si heterostructures. If such many body corrections were counted in, the achieved increase of CBO would be nearly canceled out, and the resulting CBO (near zero eV) is in good agreement with the XPS results from Chambers *et al.* [22] Nevertheless, the demonstrated ability of tuning the band alignments between high-*k* oxide and Si by Först *et al.* [60] is still very encouraging and has wide applications in engineering high-*k* dielectric/Si interfaces and other semiconductor heterostructures. In this thesis, we will show how sensitively the band offsets between high-*k* oxide and silicon depend on interface structures and strain states of the two bulk materials (Si and ZrO_2).

1.4.2 Barrier heights at metal gate/high-*k* oxide interfaces

For metal gates replacing conventional poly-Si as the gate electrodes, a major stumbling block is the difficulty in identifying gate materials which can locate the dielectric/Si interface Fermi energy near the Si conduction (or valence) band edges for NMOS (or PMOS) devices. Here, an effective work function of metal gates ($\Phi_{m,eff}$) is defined as the location of the energy position of metal gate Fermi level in the band gap of Si channel, as shown in Fig. 1.6. Notice the vacuum discontinuity ($\mathbf{\Delta_1}$ and $\mathbf{\Delta_2}$) at the two interfaces. In typical semiconductor text books, the band diagrams of an MOS diode in thermal equilibrium are often simplified and the energy bands are aligned only

using the electron affinity of the materials in the two sides.[61] Thus the vacuum levels there are continuous. As we will discuss below, this corresponds to the Schottky limits, not the general situation.

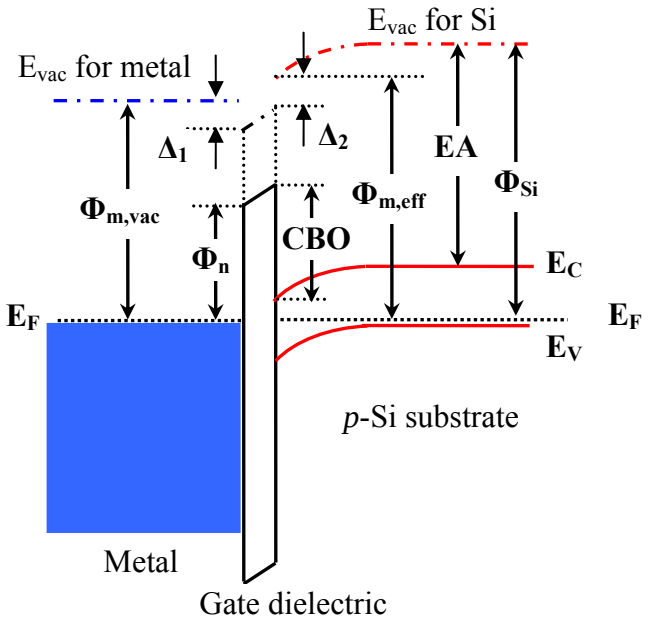

Fig. 1.6 Energy band diagram of a MOS diode in thermal equilibrium. $\mathbf{E_{vac}}$ is the vacuum level. $\mathbf{\Phi_{m,vac}}$ is the vacuum work function of metal gate. $\mathbf{\Phi_{m,eff}}$ is the effective work function of metal gate on gate dielectric. $\mathbf{\Phi_{Si}}$ is the work function of *p*-Si substrate. $\mathbf{\Phi_n}$ is the barrier height between metal and gate dielectric. **CBO** is the conduction band offset between gate dielectric and Si. **EA** is the electron affinity of Si (~4.05 eV). $\mathbf{\Delta_1}$ and $\mathbf{\Delta_2}$ denote the vacuum level discontinuity at the two interfaces.

For real MOS capacitors, it is not an easy job to evaluate the effective work function accurately because it is determined by the band alignments at two interfaces which are very complex. The most common way to extract the effective work function of metal gates is varying the thickness of the dielectric layer and plotting the capacitor flat band voltage (V_{FB}) versus the effective oxide thickness (EOT) of the dielectric layer. The flat-band condition means no charge induced in the semiconductor and V_{FB} is expressed as $V_{FB} = (\Phi_{eff.m} - \Phi_{Si}) + V_{oxide}$ with V_{oxide} the potential across the oxide

dielectric layer. By assuming that V_{oxide} only originates from the fixed charge at the dielectric/Si interface (Q_f , can be positive or negative, depending on the specific interface.), V_{FB} can be re-expressed as $V_{FB} = (\Phi_{eff.m} - \Phi_{Si}) - Q_f \times EOT / \varepsilon_{SiO_2}$. The thickness series (EOT) of dielectric layer allows one to extract the effective work function and fixed charge at the dielectric/Si interface. This capacitance-based method needs no detailed information concerning the band alignments at the two interfaces, *e.g.*, barrier height for metal/dielectric interface and dielectric/silicon interface. However, appropriate interfacial structures at the dielectrics/Si interfaces and the corresponding charge distributions should be carefully considered.

The effective work function can also be obtained by measuring the barrier height for metal/dielectric interface and dielectric/silicon interface separately, expressed by $\Phi_{m,eff} = \Phi_n - CBO + EA$, where Φ_n is the n-type Schottky barrier height between metal gate electrode and high-k gate dielectric, CBO is the conduction band offset between high-*k* gate dielectric and Si, as shown in Fig. 1.5., and EA is the electron affinity of Si (4.05 eV), which is the energy difference between the vacuum level and Si conduction band maximum (CBM). We note that the above definition is for a flat band condition, where the surface charge induced band banding is negligible within the interface-specific region (several nanometers). For a given high-*k* oxide/Si interface, the effective work function is only determined by the band alignment at metal gate/high-*k* oxide interface, or Φ_n.

"What determines the magnitude of Schottky barrier height Φ_n at metal/semiconductor interfaces?" is a question which has troubled scientists for decades. [62] The first attempts to understand the rectifying properties of metal/semiconductor interfaces are the views attributed to Schottky himself and also to

Mott. [63] The famous Schottky-Mott relationship, $\Phi_n = \Phi_{m,vac} - EA$, states that the SBH depends on the vacuum work function of metal ($\Phi_{m,vac}$) and the semiconductor electron affinity (EA). The simple Schottky-Mott picture did not take into account the local electronic structures at the interface but only considered the "pseudo-bulk" properties, $\Phi_{m,vac}$ and EA. Here, "pseudo-bulk" means that although based on the bulk electronic structures of the two materials, they are measured by performing experiments on their surfaces and thus are surface-sensitive.

In real metal gate/high-*k* dielectric interfaces, the simple Schottky-Mott relationship is rarely realized. Instead, the dependence of SBH on metal vacuum work function was found not as sensitive as predicted by Schottky-Mott relationship. A term, "Fermi level pinning", has often been used to describe the insensitivity of the experimental SBH to the metal vacuum work function. One popular model proposes that the SBH is modulated by the metal induced gap states (MIGS). [64] MIGS are the evanescent states of metal wavefunctions tunneling into the forbidden band gap of semiconductor. Tersoff [65] claimed that if the MIGS decay length is large, the variation of metal Fermi level would be screened efficiently within several atomic layers in the semiconductor side at the interface. This MIGS screening induced Fermi level pinning effect is described by[66]

$$\Phi_n = S(\Phi_{m,vac} - \Phi_{CNL}) + (\Phi_{CNL} - EA) \tag{1.3}$$

where S is the so-called Schottky pinning parameter which is characteristic of semiconductor, with S=1 describing the Schottky-Mott picture and S=0 describing the Barding limit of strong pinning, and Φ_{CNL} is the energy position of charge neutrality level (CNL) of the semiconductor with respect to the vacuum level. CNL is defined as the energy above which the surface states are empty. One may wonder how MIGS are

related to CNL. Notice that MIGS are actually Bloch states of the bulk semiconductor with complex wave vector. The most important assumption in the MIGS or CNL model is that the MIGS (the exponentially decaying bulk states) of the semiconductor are the main component of the surface (or interface) states, irrespective of the type of metal. In MIGS theory, both pinning parameter S and the energy position of CNL can be estimated from the bulk properties of the semiconductor only. Mönch[67] found that pinning parameter S can be estimated from the empirical formula

$$S = [1 + 0.1(\varepsilon_\infty - 1)^2]^{-1} \tag{1.4}$$

where ε_∞ is the electronic component of the dielectric constant of semiconductor. A wide gap material would tend to have a smaller ε_∞ and thus pin less. To estimate the energy position of charge neutrality level, Robertson[68] used Tersoff's idea[69] and associated it with the branch points of the complex band structure of the dielectric. The branch point is located by calculating the zero of Green functions of the band structure, taken over the Brillion zone. However, this method to find the CNL using direct integration of density of states are in general not in good agreement with the result from the calculation of actual complex band structures. [70] Thus, how to evaluate the energy position of CNL in the fundamental band gap of high-*k* material is still an open question.

The above MIGS model is appealing because it offers a simple scheme to predict SBH from the bulk properties of the two components (metal and semiconductor) only, with no need for the detail interface information, *e.g.*, interface structures or chemical compositions.

However, the MIGS model only reflects one side of the coin. [71] In addition to the contribution of MIGS for the SBH, there is another contribution, a short range part, the

polarized interface bonding.[72] The polarized interface bonds forms interface dipole, which will shift the energy bands on both sides of the interface and change the SBH. Then, there is a competition between MIGS and interface bonding. If MIGS is large enough, the electrostatic potential from interface bonds or the metal-semiconductor electronegativity difference would be screened efficiently and strong Fermi level pinning is formed. This is the situation that has been demonstrated for metal on covalent or small gap semiconductors (Si, Ge, and GaAs).[73] However, high-*k* dielectric materials are mostly large band gap ionic semiconductors or insulators, where the decay length of MIGS is rather short. It is expected that interface bonding instead of MIGS would play dominant role in deciding the SBHs of metal gate/high-*k* oxide interfaces. Checking this assumption and understanding it on atomic scale is one of the main objectives of this thesis.

To understand the formation mechanism of SBH at metal gate/high-*k* dielectrics, one must measure the effective work function of metal gates ($\Phi_{m,eff}$) or Schottky barrier height accurately. As mention above, a widely used method is to extract the values of effective work function from the relations of flat-band voltage versus equivalent oxide thickness (EOT) for metal gate/high-*k* dielectrics/Si capacitors.[74] In this capacitance-based method, appropriate interfacial structures at the high-*k* dielectrics/Si interfaces and the corresponding charge distributions should be carefully considered.[75] Alternatively, *p*-type SBHs for metal gate/ dielectric interfaces can be directly measured by *x*-ray photoemission method proposed by Kraut *et al.*[76] This method will be applied in this thesis to accurately determine the barrier height between metal/high-*k* oxide interfaces.

1.5 Motivations and scope for present work

Although intensive studies have been carried out on the alternative high-*k* gate dielectric and metal gate materials, there are still many challenges in their application for the future generations of Si-based MOSFET technologies, *e.g.*, growth of high quality interfaces between Si and high-*k* oxides, and tuning the magnitude of the effective work functions for metal gate on high-*k* dielectrics up to a range of 1.1 eV. In order to identify the right alternative high-*k* gate dielectric and metal gate materials, it is essential to understand and control the two interfaces, the front interface between metal gate electrode and high- *k* dielectric, and the back one between high- *k* dielectric and Si substrate, on the atomic scale.

The main objective of this thesis is to investigate how the atomic-level interface structures affect the properties of metal gate/high-*k* dielectric oxide/Si stacks, or how the macroscopic properties (*e.g.*, band alignments for metal gate/high-*k* dielectric oxide and high-*k* dielectric/Si interfaces) are related to the electronic structures on small length scale (*e.g.,* interface bonding). A combined approach of (i) characterization techniques, *e.g.*, transmission electron microscopy (TEM), and *x*-ray photoemission (XPS), and (ii) first principle calculations based on density functional theory (DFT) will be applied. Characterization studies (TEM and XPS) will provide a complete picture for the metal/oxide and oxide/Si interfaces on the atomic scale. The first-principles calculations would offer explanations for the related experimental results and provide insight into the physical mechanism behind the formation of metal/high-*k* oxide and high-*k* oxide/Si interfaces.

It is recognized that high-*k* oxide in amorphous or in single crystalline can both be used as the alternative dielectric material to replace SiO_2. In present study, we will

focus the study on crystalline materials and choose the single crystalline ZrO_2, one of the most promising candidates, as the prototype of high-*k* dielectric material because it has a well defined surface and simple cubic structure, which leads us to focus on interface effects without perturbation from the bulk contribution. In addition, crystalline structure is very appropriate for our first principles calculations where supercell structures are used to mimic the infinite crystalline material.

This thesis is organized as follows:

Chapter 2 briefly introduces the interface characterization techniques (XPS and TEM), the first-principles calculation methods based on density functional theory, and their applications in this study. Chapter 3 describes the investigation of epitaxial ZrO_2 on silicon structure as alternative gate dielectric, including film growth, interface characterization, and electronic structure calculations. Chapter 4 describes the growth and characterizations of epitaxial Ni ultrathin film on ZrO_2 substrate. The interface effects on Schottky barrier height for Ni/ZrO_2 interfaces are studied experimentally and theoretically. Chapter 5 describes the chemical tuning of band alignments for metal gate/high-*k* dielectric interfaces. By including one layer of heterovalent metal between Ni and ZrO2 interfaces, we will study the variation trend of the Schottky barrier for the interface. Finally, chapter 6 presents the summery of this thesis and suggests recommendations for future work.

References

[1] G. E. Moore, Progress in digital integrated electronics. *IEEE IEDM Tech. Dig.* , 11－13 (1975).

[2] R. M. Wallace and G. D. Wilk, Mater. Res. Soc. Bull. **27**, 186 (2002).

[3] The International Technology Roadmap for Semiconductor 2005, URL: http://public.itrs.net.

[4] H. R. Huff, and D. C. Gilmer, *High Dielectric Constant Materials* (Springer, New York, 2004)

[5] M. Depas, B. Vermeire, P. W. Mertens, R. L. van Meihaeghe, and M. M. Heyns, Solid-State Electron. **38**, 1465 (1995).

[6] Michel Houssa, *High-k Gate Dielectrics* (Institute of Physics Publishing, Bristol and Philadelphia, 2004)

[7] A. I. Kingon and S. K. Streiffer, Nature (London) **406**, 1032 (2000).

[8] G. D. Wilk, R. M. Wallace, and J. M. Anthony, J. Appl. Phys. **89**, 5243 (2001).

[9] T. Hori, *Gate Dielectrics and MOS ULSIs* (Springer, New York, 1997)

[10] P. W. Peacock and J. Robertson, Appl. Phys. Lett. **83**, 5497 (2003).

[11] P. W. Peacock and J. Robertson, Phys. Rev. Lett. **92**, 057601 (2004).

[12] H. S. Kim, S. A. Campbell, and D. C. Gilmer, IEEE Electron Dev. Lett. **18**, 465 (1997).

[13] K. Eisenbeiser, J. M. Finder, Z. Yu, J. Ramdani, J. A. Curless, J. A. Hallmark, R. Droopad, W. J. Ooms, L. Salem, S. Bradshaw, and C. D. Overgaard, Appl. Phys. Lett. **76**, 1324 (2000).

[14] A. Fissel, J. Dabrowski, and H. J. Osten, J. Appl. Phys. **91**, 8986 (2002).

[15] S. Guha, E. Cartier, N. A. Bojarczuk, J. Bruley, L. Gignac, and J. Karasinski, J. Appl. Phys. **90**, 512 (2001).

[16] V. Naraynan, S. Guha, M. Copel, N. A. Bojarczuk, P. L. Flaitz, and M. Gribelyuk, Appl. Phys. Lett. **81**, 4183 (2002).

[17] L. F. Edge, D. G. Schlom, R. T. Brewer, Y. J. Chabal, J. R. Williams, S. A. Chambers, C. Hinkle, G. Lucovsky, Y. Yang, S. Stemmer, M. Copel, B. Holländer, and J. Schubert, Appl. Phys. Lett. **84**, 4629 (2005).

[18] R. A. McKee, F. J. Walker, and M. F. Chisholm, Phys. Rev. Lett. **81**, 14 (1998).

[19] X. Zhang, A. A. Demkov, Hao Li, X. Hu, and Yi Wei, Phys. Rev. B **68**, 125323 (2003).

[20] Z. Yu, J. Ramdani, and J. A. Curless, et al., J. Vac. Sci. Technol. B **18** （**4**）, 2139 (2000).

[21] X. M. Hu, H. Li, Y. Liang, Y. Wei, Z. Yu, D. Marshall, J. Edwards, Jr., R. Droopad, X. Zhang, A. A. Demkov, K. Moore, and J. Kulik, Appl. Phys. Lett. **82**, 203 (2003).

[22] S. A. Chambers, Y. Liang, Z. Yu, R. Droopad, J. Ramdani, and K. Eisenbeiser, Appl. Phys. Lett. **77**, 1662 (2000).

[23] R. A. McKee, F. J. Walker, M. Buongiorno Nardelli, W. A. Shelton, and G. M. Stocks, Science **300**, 1726 (2003).

[24] S. J. Wang, C. K. Ong, and S. Y. Xu, et al., Appl. Phys. Lett. **78**, 1064 (2001).

[25] S. J. Wang and C. K. Ong, Appl. Phys. Lett. **80**, 2541 (2002).

[26] J. Y. Dai, P. F. Lee, K. H. Wong, H. L. W. Chan, and C. L. Choy, J. Appl. Phys. **94**, 912 (2003).

[27] V. Fiorentini and G. Gulleri, Phys. Rev. Lett. **89**, 266101 (2002).

[28] Y. F. Dong, Y. P. Feng, S. J. Wang, and A. C. H. Huan, Phys. Rev. B **72**, 045327 (2005).

[29] Clemens J. Först, Karlheinz Schwarz, and Peter E. Blöchl, Phys. Rev. Lett. **95**, 137602 (2005).

[30] Yee-Chia Yeo, Tsu-Jae King, and Chenming Hu, J. Appl. Phys. **92**, 7266 (2002).

[31] V. V. Afanas'ev, M. Houssa, A Stesmans, and M. M. Heyns, J. Appl. Phys. **91**, 3079 (2002).

[32] Y. F. Dong, S. J. Wang, J. W. Chai, Y. P. Feng, and A. C. H. Huan, Appl. Phys. Lett. **86**, 132103 (2005).

[33] R. Lin, Q. Lu, P. Ranade, and C. Hu, IEEE Electron Device Lett. **23**, 49 (2002).

[34] Charles M. Perkins, Baylor B. Triplett, Paul C. McIntyre, Krishna C. Saraswat, and Eric Shero, Appl. Phys. Lett. **81**, 1417 (2002).

[35] C. Hobbs, L. Fonseca, and V. Dhandapani *et al.*, IEEE Symp. on VLSI Technology Tech. Dig. 2-1 (2003).

[36] V. Misra, G. P. Heuss, and H. Zhong, Appl. Phys. Lett. **78**, 4166 (2001).

[37] A. A. Knizhnik, I. M. Iskandarova, A. A. Bagatur'yants, B. V. Potapkin, and L. R. C. Fonseca, J. Appl. Phys. **97**, 064911 (2005).

[38] C. Ren, D. S. H. Chan, X. P. Wang, B. B. Faizhal, M.-F. Li, Y.-C. Yeo, A. D. Trigg, A. Agarwal, N. Balasubramanian, . S. Pan, P. C. Lim, A. C. H. Huan, and D.-L. Kwong, Appl. Phys. Lett. **87**, 073506 (2005).

[39] C. Ren, H. Y. Yu, X. P. Wang, H. H. H. Ma, D. S. H. Chan, M.-F. Li, Y.-C. Yeo, C. H. Tung, N. Balasubramanian, A. C. H. Huan, J. S. Pan, and D.-L. Kwong,, IEEE Electron Dev. Lett. **25**, 123 (2004).

[40] Y. S. Suh, G. P. Heuss, J. H. Lee, and V. Misra, IEEE Electron Dev. Lett. **24**, 439 (2003).

[41] S. B. Samavedam, IEEE International Electron Device Meeting Technical Digest, 4336 (2002).

[42] Takashi Matsukawa, Chiaki Yasumuro, Hiromi Yamauchi, Meishoku Masahara, Eiichi Suzuki, and Seigo Kanemaru, Appl. Phys. Lett. **86**, 094104 (2005).

[43] V. Misra, H. Zhong, and H. Lazar, IEEE Electron Dev. Lett. **23**, 354 (2002).

[44] Y.-C. Yeo, Q. Lu, and P. Ranade, et al., IEEE Electron Device Lett. **22**, 227 (2001).

[45] I. Polishchuk, P. Ranade, T.-J. King, and C. Hu, IEEE Eletron Device Lett. **23**, 200 (2002).

[46] J. Lee, H. Zhong, and Y. -S Suh, et al., IEEE IEDM, 359 (2002).

[47] C. H. Lu, G. M. T. Wong, and M. D. Deal, *et al.*, IEEE Electron Device Lett. **26**, 445 (2005).

[48] Seongjun Park, Luigi Colombo, Yoshio Nishi, and Kyeongjae Cho, Appl. Phys. Lett. **86**, 073118 (2005).

[49] Yee-Chia Yeo, Thin Solid Films **462-463**, 34 (2004).

[50] A. Franciosi and C. van de Walle, Surf. Sci. Rep. **25**, 1 (1996).

[51] M. Peressi, N. Binggeli, and A. Baldereschi, J. Phys. D **31**, 1273 (1998).

[52] E. A. Kraut, R. W. Grant, J. R. Waldrop, and S. P. Kowalczyk, Phys. Rev. Lett. **44**, 1620 (1980).

[53] S. A. Chambers, Y. Liang, Z. Yu, R. Droopad, and J. Ramdani, J. Vac. Sci. Technol. A **19**, 934 (2001).

[54] S. J. Wang, A. C. H. Huan, Y. L. Foo, J. W. Chai, J. S. Pan, Q. Li, Y. F. Dong, Y. P. Feng, and C. K. Ong, Appl. Phys. Lett. **85**, 4418 (2004).

[55] S. J. Wang, Y. F. Dong, A. C. H. Huan, Y.P. Feng, and C. K. Ong., Mater. Sci. Eng. **118**, 122 (2005).

[56] S. Miyazaki, J. Vac. Sci. Technol. B **19**, 2212 (2001).

[57] R. Puthenkovilakam and J. P. Chang, Appl. Phys. Lett. **84**, 1353 (2004).

[58] M. Oshima, S. Toyoda, T. Okumura, J. Okabayashi, H. Kumigashira, K. Ono, M. Niwa, K. Usuda, and N. Hirashita, Appl. Phys. Lett. **83**, 2172 (2003).

[59] H. Jin, H. J. Kang, S. W. Lee, Y. S. Lee, and M. -H. Cho, Appl. Phys. Lett. **87**, 212902 (2005).

[60] C. J. Först, C. R. Ashman, K. Schwarz, and P. E. Blochl, Nature (London) **427**, 53 (2004).

[61] S. M. Sze, *Semiconductor Devices: Physics and Technology* (John Wiley and Sons, 2001)

[62] L. J. Brillson, J. Vac. Sci. Technol. **16**, 1137 (1979).

[63] W. Schottky, R. Stormer, and F. Waibel, Z. Hoch Frequentztechnik **37**, 162 (1931).

[64] S. G. Louie, J. R. Chelikowsky, and M. L. Cohen, Phys. Rev. B **15**, 2154 (1977).

[65] J. Tersoff, Phys. Rev. Lett **52**, 465 (1984).

[66] J. Robertson and C. W. Chen, Appl. Phys. Lett. **74**, 1168 (1999).

[67] W Mönch, Phys. Rev. Lett. **58**, 1260 (1987).

[68] John Robertson, J. Vac. Sci. Technol. B **18**, 1785 (2000).

[69] J. Tersoff, Phys. Rev. B **30**, 4874 (1984).

[70] A. A. Demkov, L. R. C. Fonseca, E. Verret, J. Tomfohr, and O. F. Sankey, Phys. Rev. B **71**, 195306 (2005).

[71] R. T. Tung, Phys. Rev. Lett. **84**, 6078 (2000).

[72] S. Chang, L. J. Brillson, Y. J. Kime, D. S. Rioux, P. D. Kirchner, G. D. Pettit, and J. M. Woodal, Phys. Rev. Lett. **64**, 2551 (1990).

[73] W. Mönch, J. Vac. Sci. Technol. B **17**, 1867 (1999).

[74] Rashmi Jha, Jason Gurganos,, Y. H. Kim, R. Choi, Jack Lee, and Veena Misra, IEEE Electron Device Lett. **25**, 420 (2002).

[75] Hyundoek Yang, Yunik Son, Sungkwon Baek, Hyunsang Hwanga, Hajin Lim, and Hyung-Seok Jung, Appl. Phys. Lett. **86**, 092107 (2005).

[76] E. A. Kraut, R. W. Grant, J. R. Waldrop, and S. P. Kowalczyk, Phys. Rev. B **28**, 1965 (1983).

Chapter 2

Characterization Techniques and Modeling Methods

2.1 X-ray photoemission spectroscopy characterization

2.1.1 Physics basis

Photoelectron spectroscopy utilizes photo-ionization and energy-dispersive analysis of the emitted photoelectrons to study the composition and electronic state of the surface region of a sample. Traditionally, when the technique has been used for surface studies it has been subdivided according to the source of exciting radiation into : (i) *x*-Ray Photoemission Spectroscopy (XPS), using soft x-ray (200-2000 eV) to examine core levels; and (ii) ultraviolet Photoemission Spectroscopy (UPS), using vacuum UV (10-45 eV) radiation to examine valence band.

The physical mechanism behind XPS is the photoelectric effect (observed first by Heinrich Hertz[1] in 1887) and the photoelectric law (proposed by Albert Einstein[2] in 1905). From one-electron model and the conservation of energy, the related energy relation between initial state and final state can be expressed as [3]

$$E(A) + \hbar\omega = E(A^+) + E(e^-) \tag{2.1}$$

or

$$E_{kin} = \hbar\omega - [E(A^+) - E(A)] \tag{2.2}$$

where E_{kin} is the kinetic energy of the photoionized electron, and $[E(A^+)-E(A)]$ is the binding energy when the electron was localized in an orbital. A photoelectron spectrum can be recorded by measuring the kinetic energy (E_{kin}) distribution of the emitted photoelectron using any appropriate electron energy analyzer and calculate photoelectron binding energy (E_B) in electron volts (eV)

$$E_{kin} = \hbar\omega - E_B - \phi + \delta \tag{2.3}$$

where $\hbar\omega$ is the excitation *x*-ray energy, ϕ is the electron spectrometer work function, and δ is the energy shift contributed by net surface charges.

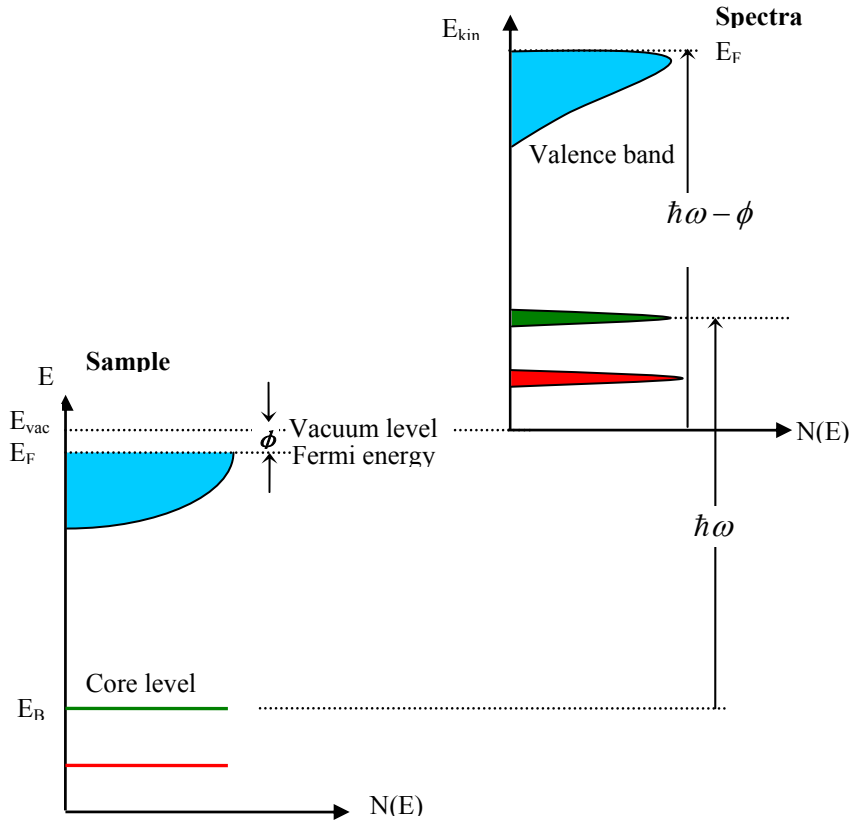

Fig. 2.1 Relation between the energy levels in a metal sample and the electron distribution produced by photons of energy $\hbar\omega$.

Figure 2.1 shows schematically how the energy-level diagram and the energy distribution of photoemitted electrons relate to each other. The solid sample has core levels and a valence band. In the case of metal, the Fermi energy E_F is at the top of the valence band and the energy difference between E_F and vacuum level E_{vac} is the metal work function ϕ. If photoabsorption takes place in a core level with binding energy E_B (E_B =0 at E_F) the photoelectrons can be detected with kinetic energy $E_{kin} = \hbar\omega - E_B - \phi$ in the vacuum. As shown in Fig. 2.1, *x*-ray photoemission spectroscopy is able to provide us information on the electron energy distribution in a material. In actual data accumulation, the reference point for molecules and atoms is taken to be E_{vac}, while in solids E_F is taken as the natural zero. In general, one plots not the kinetic energy but E_B, according to Eq. (2.3).

2.1.2 Important parameters of XPS

Sampling depth The *x*-ray penetrates into the sample with a distance of several μm. However, the depth related to the emission and detection of photoelectrons is much less and the surface sensitivity arises from such small depth. The probability of a detected photoelectron originating from a particular depth *d* is:

$$P(d) = \frac{1}{\lambda} e^{-d/\lambda} \tag{2.4}$$

where λ is the inelastic mean free path (IMFP), a measure of the average distance traveled by an electron through a solid before it is inelastically scattered. From Eq. (2.4), it is estimated that 63% of the photoelectrons are originated from a distance range of $0<d<\lambda$; 23% are from $\lambda<d<2\lambda$ and 9% from $2\lambda<d<3\lambda$. Virtually most (>95%) of the electrons detected come from within 3IMFPs of the surface. Thus 3λ (3 IMFPs) is called “sampling depth” or “information depth”. λ depends on two factors: the initial

kinetic energy of the electron and the nature of the sample. The typical value of λ is less than l nm for electron energies in the range of 15 eV ~ 35 eV, and larger than 2nm for electron energies in the range of 350 eV ~ 1400 eV. This means that XPS, which involves the generation and detection of electrons of such energies, will be surface sensitive. If we collect photoelectrons at more grazing emission angle, the surface sensitivity will increase; this is called angle-resolved XPS.

Detection limit and elemental quantification: Most XPS measurement gives us a relative quantification of surface concentration, and detection limit concerning the concentration of a specific element in the sample is in the range of 0.1%-1%. Also, different elements have different detect sensitivity. The number of photoelectrons per second in a spectra peak is given by

$$I = n/S \tag{2.5}$$

and the number of atoms of the element per cm^3 of the sample is

$$n = I/S \tag{2.6}$$

where S is atomic sensitivity factor. A general expression for determining the atom fraction of any constituent in a sample, Cx, can be written as

$$Cx = (Ix/Sx)/(\Sigma\ Ii/Si) \tag{2.7}$$

where Ix and Sx are the peak area and atomic sensitivity factor of element x respectively.

Energy resolution: In XPS the energy resolution or the full width at half maximum (FWHM) ΔE can be expressed as

$$\Delta E = (\Delta E_n^{\ 2} + \Delta E_p^{\ 2} + \Delta E_a^{\ 2})^{1/2} \tag{2.8}$$

where ΔEn is the intrinsic width of the initial level and the lifetime of the final state, and ΔE_a is the resolving power of electron-energy analyzer. In most cases, the line-

width ΔE_p of source *x*-ray is the major contribution to the overall XPS spectrum resolution. The efficient way to narrow down the width is to use a monochromator gun as equipped in VG ESCA LAB-220i XL system, where a best energy resolution of around 0.45 eV can be achieved. Notice that the energy resolution for XPS introduced here is different from the accuracy of the observed binding energy (BE), which is within 0.02~0.03 eV on an absolute scale over the binding energy range of 0 to 1000 eV for VG ESCA LAB-220i XL system after careful calibration.

2.1.3 Chemical shift primary line and spectral line interpretation

There are three kinds of lines in XPS spectra:

a) Photoelectron lines: the most intense photoelectron peaks are generally symmetrical and are typically the narrowest peaks observed in the spectra.

b) Auger lines: there are groups of peaks in rather complex patterns, main Auger series observed in XPS are KL, LMM, MNN and NOO series.

c) Valence band: lines of low intensity occur in the low binding energy region of 0-20eV. These lines are produced by photoelectron emission from molecular orbital and from solid-state energy bands. From binding energy of photoelectron with reference of Auger lines or valence band one can identify almost all the elements in the periodic table, except H and He. The binding energy of an electron depends on:

1) The level from which photoemission is occurring.
2) The formal oxidation state of the atom.
3) The local chemical and physical environment.

Change in either (2) or (3) gives rise to small shift in the peak position in spectrum, namely, *chemical shifts*. These shifts enable one to obtain information on chemical states from the variations in binding energies of the photoelectrons. In chemistry,

binding energies are frequently correlated with the charge on an atom. The chemical shift between a metal and its oxide very often serves to monitor the surface cleanliness. For example, the absence of oxygen is proven by the absence of the chemically shifted (to larger binding energies) metal oxide line.

2.1.4 XPS instrumentation and application in this study

As shown in photos in Fig 2.2, the XPS facility (VG ESCALAB 220i-XL XPS system) consists of UHV main chamber X-ray gun, a monochromator, an ion-sputtering gun, a flood electron gun, and an energy analyzer. A separate sample preparation chamber is attached to the main chamber. Energy analyzer shown in Fig. 2.2 is the key part of the XPS machine that has both an inner hemisphere and outer hemispheres to produce electronic field. A special arrangement of a series of optical lens system will let electron to be within very small energy dispersion and go across the field to reach the detector so that the signals can be recorded. Our XPS spectrometer was calibrated with pure nickel, gold, silver, and copper by setting Fermi edge, Au $4f_{7/2}$, Ag $3d_{5/2}$, and Cu $2p_{3/2}$ at binding energy of 0.00 ± 0.02 eV, 83.93 ± 0.02 eV, 368.26 ± 0.02 eV, and 932.67 ± 0.02 eV, respectively. Thus, all absolute binding energies are accurate on an absolute scale to within 0.02-0.03 eV over the binding energy range 0-1000 eV, while binding energy differences are accurate on a scale of ± 0.05 eV.

There are two main purposes using XPS in this study: a) to monitor the interface reactions at ZrO_2/Si and Ni/ZrO_2 interfaces; and b) to determine the band alignment at ZrO_2/Si and Ni/ZrO_2 interfaces, with valence band offsets for the former and Schottky barrier height (SBH) for the latter.

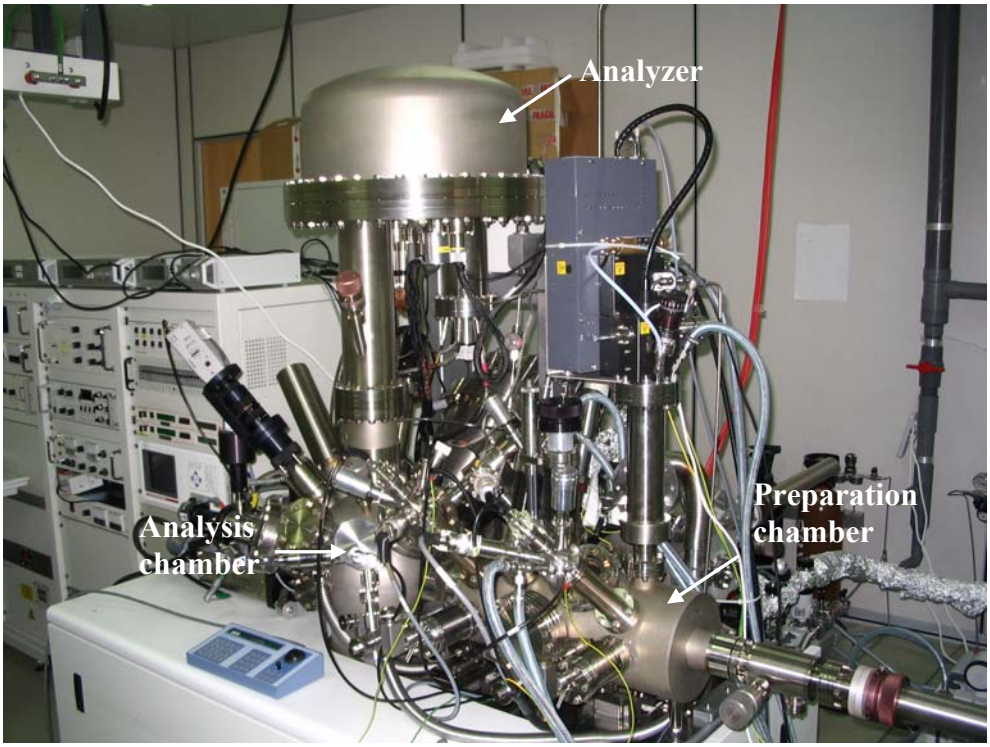

Fig. 2.2 Overview of the VG ESCALAB 220i-XL XPS system.

2.2 Transmission Electron Microscopy (TEM) Characterization

2.2.1 Principles of operations

The transmission electron microscopy uses a high energy electron beam transmitted through a very thin sample to image and analyze the microstructure of materials with atomic scale resolution.[4, 5] The electrons are focused with electromagnetic lenses and the image is observed on a fluorescent screen, or recorded on film or digital camera. The electrons are accelerated at several hundred kV, giving wavelengths much smaller than that of light: 200kV electrons have a wavelength of 0.025Å. Transmission electron microscopes are, in principle, similar to optical microscopes; both contain a series of lenses to magnify the sample. Whereas the resolution of the optical microscope is limited by the wavelength of light, that of the

electron microscope is limited by aberrations inherent in electromagnetic lenses, to about 1-2 Å.

The main strength of TEM lies in its extremely high resolution. The reason for this high resolution can be traced to the resolution equation $s = 0.61\lambda / NA$, where s is the resolution, λ is the wavelength of the high energy electron (for 200 kV electrons, λ~0.015 Å), and NA is the numerical aperture. In electron microscopy, NA is about 0.01 due to electron lens imperfections. According to the resolution equation, λ=0.015 Å gives a resolution of s=0.15 nm. The actual resolution expression is more complicated and this simple calculation should only be taken as a crude estimate.

Because even for very thin samples one is looking through many atoms, one does not usually see individual atoms. Rather the high resolution imaging mode of the microscope images the crystal lattice of a material as an interference pattern between the transmitted and diffracted beams. This allows one to observe planar and line defects, grain boundaries, interfaces, etc. with atomic scale resolution. The bright-field or dark-field imaging modes of the microscope, which operate at intermediate magnification, combined with electron diffraction, are also invaluable for giving information about the morphology, crystal phases, and defects in a material. A shortcoming of TEM is its limited depth resolution.

The TEM is also capable of forming a focused electron probe, as small as 20Å, which can be positioned on very fine features in the sample for microdiffraction information or analysis of *x*-rays for compositional information. The spatial resolution for this compositional analysis in TEM is much higher, on the order of the probe size, because the sample is so thin. Conversely the signal is much smaller and therefore less quantitative. The high brightness field-emission gun improves the sensitivity and

resolution of *x*-ray compositional analysis over that available with more traditional thermionic sources.

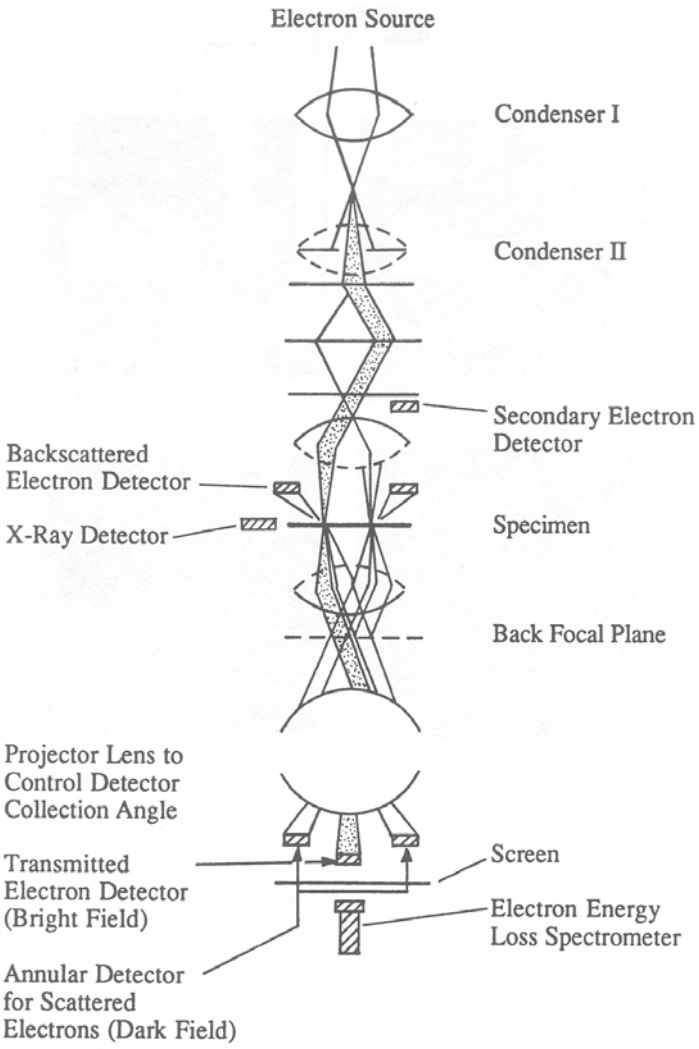

Fig. 2.3 Schematic diagram of a transmission electron microscope[6]

A schematic of transmission electron microscopy is shown in Fig. 2.3. Electrons from an electron gun are accelerated to high voltage (typically 100 to 400 kV) and focused on the sample by condenser lenses. The sample is fit into a 3mm diameter cooper grid. A TEM sample must be sufficiently thin (approximately1000Å or less in thickness) in the area of interest so that it is transparent to electrons. The transmitted and forward scattered electrons form a diffraction pattern in the back focal plane and a

magnified image in the image plane. The ability to form a diffraction pattern allows structural information to be obtained.

2.2.2 Restrictions on samples

The success of TEM is very much dependent on sample preparation. Sample preparation for TEM generally requires more time and experience than for most other characterization techniques. A TEM specimen must be approximately1000Å or less in thickness in the area of interest. The entire specimen must fit into a 3mm diameter cup and be less than about 100 microns in thickness. A thin, disc shaped sample with a hole in the middle, the edges of the hole being thin enough (<100 nm) for TEM viewing, is typical. The initial disk is usually formed by cutting and grinding from bulk or thin film/substrate material, and the final thinning done by ion milling. Other specimen preparation possibilities include direct deposition onto a TEM-thin substrate (Si_3N_4, carbon); direct dispersion of powders on such a substrate; grinding and polishing using special devices (t-tool, tripod); chemical etching and electropolishing; lithographic patterning of walls and pillars for cross-section viewing; and focused ion beam (FIB) sectioning for site specific samples.

Artifacts are common in TEM samples, due both to the thinning process and to changing the form of the original material. For example surface oxide films may be introduced during ion milling and the strain state of a thin film may change if the substrate is removed. Most artifacts can either be minimized by appropriate preparation techniques or be systematically identified and separated from real information.

In our experiments, the TEM specimens of the films were prepared by using standard preparation method (i.e., polishing, mechanical dimpling and ion-beam milling).

2.2.3 TEM instrumentation and application in this study

The transmission electron microscope facility is comprised of a Philips CM300 FEG-TEM with energy dispersive *x*-ray spectrometer EDS (as shown in Fig. 2.4), a darkroom, computer room, and specimen preparation room. The accelerating voltage is 300 kV, which has a point-to-point spatial resolution of 1.7 Å. In this study, high resolution TEM (HRTEM) is used to determine the interface structures at ZrO_2/Si and Ni/ZrO_2 interfaces on the atomic-scale. The growth rate of thin film (ZrO_2 and Ni) can also be calibrated by cross-section TEM.

Fig. 2.4 Overview of a Philips CM300 FEG-TEM system.

2.3 First-principles total energy calculation methods

2.3.1 Introduction

In principle, all knowledge about a system can be obtained from the quantum mechanical wave function. This is obtained (non-relativistically) by solving the Schrödinger equation of the complete many electron system. However in practice solving such an N-body problem proves to be impossible. This section will give a brief description of a) earlier approximations made to solve this many-body problem and a description of the important physical features omitted from these theories; b) the necessity to use density functional theory developed by Kohn and Sham based on the theory of Hohenberg and Kohn, in which the N-electron problem is expressed as N one-electron equations where each electron interacts with all other electrons via an effective exchange-correlation potential; c) the local density approximation to exchange and correlation function used to calculate these interactions; and d) the implementation of density function theory in VASP (Vienna Ab-initio Simulation Package) and CASTEP (CAmbridge Serial Total Energy Package), two state-of-the-art first-pricniples total energy caluclation programs used in this study.

2.3.2 Earlier approximations in solving Schrödinger equations

Much of condensed matter physics lies within finding the ground state of a system of N_i nuclei and N_e electrons in interaction, which is determined from the following time-independent Schrödinger equation:

$$\hat{H}(\vec{R}_1,\vec{R}_2,...;\vec{r}_1,\vec{r}_2,...)\Psi(\vec{R}_1,\vec{R}_2...;\vec{r}_1,\vec{r}_2,...) = E\ \Psi(\vec{R}_1,\vec{R}_2,...;\vec{r}_1,\vec{r}_2,...) \qquad (2.9)$$

where the wave function Ψ and the Hamiltonian $\hat{H}$ are functions of all the nucleus and electron coordinates $\vec{R}_i$ and $\vec{r}_i$, respectively. E is the eigenstate energy of the system.

Although the expression of Eq. (2.9) seems simple, the simplicity is deceptive because the sums in the Hamiltonian $\hat{H}$ range over all electrons and nuclei in a solid. Obviously, dealing with the 10^{23} particles in actual solids requires a series of approximations. A first simplification is to remove the nuclei from the quantum-mechanical problem; this is the famous Born-Oppenheimer approximation or adiabatic approximation.[7] Taking into account that the ion cores are so much more heavier than the electrons and they move much slowly, the $\hat{H}_{ion}$ term can be dissociated from other terms in the Hamiltonian and considered as a perturbation. The unperturbed Hamiltonian does not include differential operators with respect to nuclear positions. Thus the nuclear positions can be considered as classical vibrates, no more as quantum ones, leading to a separation of electronic and nuclear coordinations in the many-body wave function. Adopting the Born-Oppenheimer approximation, the Hamiltonian for the N-electron subsystem is described as:

$$\hat{H}\Psi = -\sum_i \frac{\hbar^2}{2m}\nabla_i^2\Psi + \frac{1}{2}\sum_{i\neq j}\frac{e^2}{\left|\vec{r}_i - \vec{r}_j\right|}\Psi - \sum_{i,l}\frac{Z_l e^2}{\left|\vec{r}_i - \vec{R}_l\right|}\Psi \qquad (2.10)$$

where Ψ is an antisymmetric function of N electrons in a solid. The first term is the many-body kinetic energy operator and the second describes the interactions of electrons with each other. The final term represents the interaction of the electrons with the bare nuclei at fixed positions in the solid, $\boldsymbol{R_l}$. The total energy of the system will also include the Coulomb repulsion between the ions. In general, the problem is still intractable and the numerical problem grows exponentially with the number of

electrons. Most of the computational difficulty arises from the electron-electron interaction. Because of the electron-electron interaction, the equation cannot be separated to obtain independent equations in the coordinates of the individual electrons. In the Hartree approximation, it is found that **Ψ** can be written as a product of N one-electron wavefunctions. This follows from the assumption that the electrons interact only via the Coulomb force. By replacing the Hartree wavefunction by a Slater determinant of one electron wavefunctions, the resultant ground state electron wavefunctions can be found variationally by using this trial wavefunction to obtain the Hartree-Fock equations. Then, one way to directly address the resolution of Eq. (2.10) is to replace the Coulomb interaction term by something more computationally tractable, such as an effective electron-electron potential, so that the effect of the interaction of a given electron with all others can be approximated by a potential, and the equations can be separated. This is the self-consistent-field approximation,[8] which forms the basis for almost all solid state theory.

Although Hartree-Fock approximation has the advantage to include exactly the exchange effects, the method totally neglects the electron correlation.[9, 10] At present the density functional theory (DFT) is the most successful (and also the most promising) approach to model electron-electron interaction. Its applicability ranges from atoms, molecules and solids to nuclei and quantum and classical fluids.

2.3.3 Density functional theory

Density functional theory (DFT), developed by Hohenberg and Kohn (1964)[11] and Kohn and Sham (1965)[12], is both a profound, exact theory for interacting electrons, and a practical prescription of calculation in terms of single-electron equations. DFT allows one, in principle, to solve exactly the problem of a strongly interacting electron

gas in the map of a single particle moving in an effective nonlocal potential. Since its introduction in the mid 1960s and early 1970s, DFT has been used extensively in condensed matter physics in almost all band-structure and electronic structure calculations. It has also been widely adopted in the quantum chemistry community, and has led to a computational revolution in that area.[13]

As the starting point of DFT, Hohenberg and Kohn pointed out that electron density contains in principle all the information contained in a many-electron wave function. If one knows the density of the ground state of a many-electron system, one can deduce it the external potential in which the electrons reside, up to an overall constant. The total energy including exchange and correlation of a system of electrons and nuclei, is a unique function of the electron density. This theorem allows for the systematic formation of many-body problem-interacting electrons in an external potential (being from the nuclei in a solid) — in terms of electron density as the basic variable. This statement is surprising, because the density is a real function of a single spatial variable, while the complete quantum mechanical wave function needs immense N (number of electrons) variables for its description.

Hohenberg and Kohn next observed that the variational minimum of the energy is exactly equivalent to the true ground-state energy. This theorem is a variational statement for the energy in terms of the density: the ground-state energy is a unique function of the ground-state density $n_0(\vec{r})$, which is described as:

$$E[n(\vec{r})] \equiv < \psi[n_0(\vec{r})] \left| \hat{H} \right| \psi[n_0(\vec{r})] > = < \psi[n_0(\vec{r})] \left| T + V_{ext} + V \right| \psi[n_0(\vec{r})] > \qquad (2.11)$$

where T is the kinetic energy, V_{ext} is the specific external potential of a system with ground-state density $n_0(\vec{r})$ and the ground-state energy E_0, and V is the two-body electron-electron interaction (usually the Coulomb interaction). The ground-state

energy can be found by varying the density to minimize the energy, provided we know the form of the functional $E[n(\vec{r})]$. This means, in principle, that there exists a universal functional $E[n(\vec{r})]$ that needs to be found once and for all.

While the Hohenberg-Kohn theorem rigorously established that we may use the density and the density alone, as a variable to find the ground-state energy of an *N*-electron problem, it is Kohn and Sham who then showed how it is possible, formally, to replace the many-electron problem by an exactly equivalent set of self-consistent one electron equations, thus provided practical tools for applying DFT. The Kohn-Sham total-energy functional for a set of doubly occupied electronic states ψ_i can be written as

$$E[\{\psi_i\}] = 2\sum_i \psi_i[-\frac{\hbar^2}{2m}]\nabla^2\psi_i d^3\vec{r} + \int V_{ion}(\vec{r})n(\vec{r})d^3r$$

$$+\frac{e^2}{2}\int\frac{n(\vec{r})n(\vec{r}')}{|\vec{r}-\vec{r}'|}d^3\vec{r}d^3\vec{r}' + E_{xc}[n(\vec{r})] + E_{ion}(\{\vec{R}_I\}) \qquad (2.12)$$

where V_{ion} is the static total electron-ion potential, $n(\vec{r})$ is the electron density which was obtained using a set of single-electron wave functions $\psi_l(\vec{r})$ as the main ingredients,

$$n(\vec{r}) = 2\sum_{l=1}|\psi_l(\vec{r})|^2, \qquad (2.13)$$

$E_{xc}[n(\vec{r})]$ is the exchange-correlation functional, and E_{ion} is the Coulomb energy associated with interactions among the nuclei (or ions) at positions $\{\vec{R}_I\}$. The minimum value of the Kohn-Sham energy functional is equal to the ground state energy of the system with the ions at positions $\{\vec{R}_I\}$.

Varying the energy functional with respect to the wave function, one can determine the set of wave functions ψ_i that minimize the Kohn-Sham total-energy functional.[14] These are given by the self-consistent solutions to the *Kohn-Sham equations* (1965): [12]

$$[-\frac{\hbar^2}{2m}\nabla^2 + V_{ion}(\vec{r}) + V_H(\vec{r}) + V_{xc}(\vec{r})]\psi_i(\vec{r}) = \varepsilon_i\psi_i(\vec{r}) \tag{2.14}$$

where $\psi_i(\vec{r})$ is the wave function of electronic state *i*, ε_i is the Kohn-Sham eigenvalue, and $V_H(\vec{r})$ is the Hartree-Fock potential of the electrons given by

$$V_H(\vec{r}) = \int \frac{e^2\rho(\vec{r}')}{|\vec{r} - \vec{r}'|} d^3\vec{r}' . \tag{2.15}$$

The exchange-correlation potential, $V_{xc}(\vec{r})$, is given formally by the functional derivative

$$V_{xc}(\vec{r}) = \frac{\delta E_{xc}[\rho(\vec{r})]}{\delta\rho(\vec{r})} . \tag{2.16}$$

The Kohn-Sham equations represent a mapping of the interacting many-electron system onto a system of noninteracting electrons moving in an effective potential due to all the other electrons. If the exchange-correlation energy functional was known exactly, then taking the functional derivative with respect to the density would produce an exchange-correlation potential that included the effects of exchange and correlation exactly. The Kohn-Sham equations must be solved self-consistently so that the occupied electronic states generate a charge density that produces the electronic potential that was used to construct the equations.

2.3.4 Local density approximation

The exchange-correlation energy functional $E_{xc}[n(\vec{r})]$ in Kohn-Sham equations requires some approximation for this method to be computational tractable. A simple

and surprisingly good approximation is the local density approximation (LDA), which is based on the known exchange-correlation energy of the uniform electron gas. [15] The local density approximation assumes that the charge density varies slowly on an atomic scale (i.e. each region of a molecule actually looks like a uniform electron gas). The total exchange-correlation energy can be obtained by integrating the uniform electron gas result:

$$E_{xc}[n(\vec{r})] \approx E_{xc}^{LDA} = \int n(\vec{r})\varepsilon_{xc}(\vec{r})d\vec{r} \tag{2.17}$$

where $\varepsilon_{xc}(\vec{r})$ is the exchange-correlation energy per particle in a uniform electron gas and n is the number of particles. The simplest form of the exchange-correlation potential is the form derived by Slater,[16] which uses simply $\varepsilon_{xc}(\vec{r}) = n(\vec{r})^{1/3}$. In this approximation, the correlation is not included. A much more sophisticated exchange-correlation energy for a uniform electron gas as a function of density may be derived from quantum Monte Carlo simulations [17] and used to construct exchange-correlation functionals within the framework of the LDA. [18]

The next step in improving the LDA model is to take into account the inhomogeneity of the electron gas which naturally occurs in any molecular system. This can be accomplished by a density gradient expansion, sometimes referred as the generalized-gradient approximation (GGA). The gradient corrected exchange-correlation energy is described as:

$$E_{xc}^{GGA} = \int \rho(\vec{r})\varepsilon_{xc}(\rho, \nabla\rho)d\vec{r} \tag{2.18}$$

where ε_{xc} at $\vec{r}$ depends on the density and its gradient (+ higher terms) at positions $\vec{r}$.

GGA functionals provide a better overall description of the electronic subsystem. The LDA description tends to overbind atoms, so that the bond lengths and the cell volume are usually underestimated by a few percent and while the bulk modulus is

correspondingly overestimated. GGA corrects this error and can underbind instead, leading to slightly longer bond lengths. At the moment there has been no consensus on the best GGA. For solid-state applications, the GGAs proposed by Perdew and co-workers [19, 20, 21] have been widely used and have proved to be quite successful in correcting some of the deficiencies of the LDA.

2.3.5 Implementation of DFT in VASP and CASTEP.

VASP (Vienna Ab-initio Simulation Package) [22, 23] and CASTEP (CAmbridge Serial Total Energy Package)[24] are both state-of-the-art DFT-based first-principles simulation programs. They perform *ab-initio* quantum-mechanical molecular dynamics (MD) simulations using pseudopotentials (and also the projector-augmented wave method for VASP) and a plane wave basis set. This section provides brief information specific to the implementation of DFT in the VASP and CASTEP programs, including supercell approach with periodic boundary conditions, plane wave basis set, the pseudopotential description of the electron-ion interaction, and iterative energy minimization schemes.

a. Plane wave basis set and Pseudopotential method

VASP and CASTEP are both based on a supercell method, wherein all studies must be performed on a periodic system, even when the periodicity is superficial. For example, a crystal surface must be represented by a finite-length slab with vacuum separating two surfaces. Similarly, to study molecules it is necessary to assume that they are in a box and treat them as periodic systems. There is no limitation on the shape of the supercell. The main advantage of imposing periodic boundary conditions relates to Bloch's theorem.

In Bloch's theorem, each electronic wave function can be written as a sum of plane waves,

$$\psi_i(\vec{r}) = \sum_G c_{i,\vec{k}+\vec{G}} \exp[i(\vec{k}+\vec{G})\cdot\vec{r}]. \tag{2.19}$$

In principle, this can be utilized to solve Schrödinger equation directly. Since the coefficients $c_{i,\vec{k}+\vec{G}}$ for the plane waves with small kinetic energy $(\hbar^2/2m)|\vec{k}+\vec{G}|^2$ are typically more important than those with large kinetic energy, the plane-wave basis can be truncated to the plane waves that have kinetic energies less than some particular cutoff energy. Although the truncation of the plane-wave basis set at a finite kinetic energy cutoff will lead to an error in the total energy of the system, it is possible to make this error arbitrarily small by increasing the size of the basis set by allowing a larger energy cutoff. In addition, expanding the electronic wave functions in terms of a basis set of plane waves leads the Kohn-Sham equations taking a particularly simple form. Substitution of Eq. (2.19) in to the Kohn-Sham equations, (2.14), gives

$$\sum_{\vec{G}}[\frac{\hbar^2}{2m}|\vec{k}+\vec{G}|^2\delta_{\vec{G}\vec{G}'} + V_{ion}(\vec{G}-\vec{G}') + V_H(\vec{G}-\vec{G}') + V_{xc}(\vec{G}-\vec{G}')]c_{i,\vec{k}+\vec{G}'} = \varepsilon_i c_{i,\vec{k}+\vec{G}} \tag{2.20}$$

In this form, the kinetic energy is diagonal, and the various potentials are described in terms of their Fourier transforms. Solution of Eq. (2.20) proceeds by diagonalization of the Hamiltonian matrix elements $\hat{H}_{\vec{k}+\vec{G},\vec{k}+\vec{G}'}$ given by the terms in the brackets above. The size of the matrix is determined by the choice of cutoff energy $\frac{\hbar^2}{2m}|\vec{k}+\vec{G}_c|^2$, and will be intractably large for systems that contain both valence and core electrons. This is a severe problem, but can be overcome by use of the pseudopotential approximation.

The concept of pseudopotential is a crucial one for plane-wave total energy methods since the alternative full Coulomb potential of the electron-ion interaction decays too slowly to be accurately represented by a small number of Fourier components. All-electron DFT methods treat core and valence electrons on an equal footing. Because all-electron wavefunctions of valence electrons exhibit rapid oscillations in the core region in order to satisfy the orthogonality constraint, it is impractical to represent such functions using plane waves as the size of the basis set would be prohibitive. In the pseudopotential approach ion cores are considered to be *frozen*. This means that properties of molecules or solids are calculated on the assumption that the ion cores are not involved in chemical bonding and do not change as a result of structural modifications. The pseudopotential approximation replaces core electrons and the strong Coulomb potential by a weaker pseudopotential that acts on a set of pseudo wavefunctions. This potential can be represented with only a small number of Fourier coefficients. It is now well known that the combination of the power of plane wave technology and the pseudopotential concept is extremely useful for the description of chemical bonding.[25]

The main requirement of the pseudopotential approach is that it reproduces the valence charge density associated with chemical bonds. For pseudo and all-electron wavefunctions to be identical beyond the core radius, it is necessary for the integrals of squared amplitudes of the two functions be the same. This is equivalent to requiring norm-conservation from pseudo wavefunctions (thus we call such pseudo wavefunctions norm-conserving pseudopotentials.), i.e. that each of them should carry exactly one electron. But early development of accurate norm-conserving pseudopotentials quickly showed that the potentials for transition metals and for first

row elements (O, C, N, *etc*.) turn out to be extremely hard, which require a large plane wave sets.[26, 27] Since there are inherent limits on optimizing the convergence of norm-conserving pseudopotentials , a completely different approach has been suggested by Vanderbilt,[28] named ultrasoft potentials (USPP). The rationale behind USP is that, in most cases, a high cutoff energy is only required for the plane-wave basis set when there are tightly bound orbitals that have a substantial fraction of their weight inside the core region of the atom. In these situations, the only way to reduce the basis set is to violate the norm-conservation condition by removing the charge associated with these orbitals from the core region. The pseudo wavefunctions are thus allowed to be as soft as possible within the core, yielding a dramatic reduction in the cutoff energy.

The pseudopotentials supplied with VASP and CASTEP are among the best pseudopotentials presently available. CASTEP implemented both LDA and GGA generated USPP for most elements in the periodic table; in addition, part of elements were supplied with norm-conserving pseudopotentials, which is expected to be more accurate than USPP in optical properties calculations after the geometry optimization accomplished with USPP. VASP is also supplied with a set of standard USPP, generated both from LDA and GGA (PW91 and PBE). VASP also provides projector-augmented-wave (PAW)[29, 30] potentials for all elements in the periodic table. Generally, the PAW potentials are more accurate than the USPP, especially for magnetic materials, alkali and alkali earth elements, 3d elements (left of periodic table), and lanthanides and actinides. Since the core radii of the PAW potentials are smaller, the required energy cutoffs and basis sets are also somewhat larger. If such a high precision is not required, the USPP can be used.

b. Iterative energy minimization schemes

Until the early 1980s, first principles electronic calculations were based on techniques which required the computationally expensive direct matrix diagonalisation methods. The first step to improve the computational algorithm was attributed to Car and Parrinello. [31] They formulated a new more efficient method which can be expressed in the language of molecular dynamics. The essential step was to treat the expansion coefficients of the wavefunction as dynamical variables. The ideas in their "molecular dynamics methods" are central to the efficiency of modern first principles total energy calculations. After the original work of Car and Parrinello, there have been several methods suggested to find the ground state. Arguments about which is better are still going on, but the truth is that either can possess the advantage depending on the system under study and the kind of calculation.

VASP and CASTEP offer a choice of methods for electronic relaxation. The default method in CASTEP is based on the density mixing.[32] In this scheme the sum of electronic eigenvalues is minimized in the fixed potential instead of the self-consistent minimization of the total energy. The new charge density at the end of the minimization is mixed with the initial density and the process is repeated until convergence is reached. A number of options are supported for this scheme: linear mixing, Kerker mixing, Broyden mixing and Pulay mixing, in order of increasing robustness. The conjugate-gradient based approach is used to minimize the sum of eigenvalues. A slightly more elaborate scheme that involves separate mixing of spin density has been developed for spin-polarized calculations. Most of the algorithms implemented in VASP use an iterative matrix-diagonalisation scheme: the used algorithms are based on the conjugate gradient scheme, block Davidson scheme, or a

residual minimization scheme - direct inversion in the iterative subspace (RMM-DIIS). All implemented algorithms will result in the same answer, i.e. they will correctly calculate the Kohn-Sham ground states, if they converge.

References

[1] H. Hertz, Ann. Physik **31**, 983 (1887).

[2] A. Einstein, Ann. Physik **17**, 132 (1905).

[3] Stefan Hüfner, *Photoelectron Spectroscopy* (Springer, Berlin, 1996)

[4] M. von Heimendahl, *Electron Microscopy of Materials* (Academic Press, New York, 1980)

[5] D. B. Williams and C. B. Carter, *Transmission Electron Microscopy* (Plenum, New York, 1996).

[6] D. K. Schroder, *Semiconductor material and device characterization* (Wiley-Interscience, 1998

[7] M. Born and R. Oppenheimer, Ann. Physik **87**, 457 (1927).

[8] W. A. Harrison, *Solid State Theory* (McGraw-Hill, New York, 1970), p.72.

[9] S. Fahy, X. W. Wang, and S. G. Louie, Phys. Rev. Lett. **61**, 1631 (1988).

[10] X. P. Li, D. M. Ceperley, and R. M. Martin, Phys. Rev. B **44**, 10929 (1991).

[11] P. Hohenberg and W. Kohn, Phys. Rev. **136**, B864 (1964).

[12] W. Kohn and L. J. Sham, Phys. Rev. **140**, A1133 (1965).

[13] P. L. Taylaor and O. Heinonen, *A Quantum Approach to Condensed Matter Physics* (Cambridge University Press, Cambridage, 2002), p.183.

[14] M. C. Payne, M. P. Teter, D. C. Allan, T. A. Arias, and J. D. Joannopoulos, Rev. Mod. Phys. **64**, 1045 (1992).

[15] J. P. Perdew and A. Zunger, Phys. rev. B **23**, 5048 (1981).

[16] J. C. Slater, Phys. Rev. **81**, 385 (1951).

[17] D. M. Ceperley and B. J. Alder, Phys. rev. Lett. **45**, 566 (1980).

[18] M. J. Gillan, in *Computer Simulation in Materials Science*, edited by M. Meyer and V. Pontikis (Dordrecht, Kluwer, 1991), p.257.

[19] J. P. Perdew, A. Chevary, S. H. Vosko, K. A. Jackson, M. R. Pedersen, M. R. Singh, and C. Fiolhais, Phys. Rev. B **46**, 6671 (1992).

[20] J. P. Perdew and Y. Wang, Phys. Rev. B **45**, 13244 (1992).

[21] J. P. Perdew, K. Burke, and M. Ernzerhof, Phys. Rev. Lett. **77**, 3865 (1996).

[22] G. Kresse and J. Hafner, Phys. Rev. B **47**, 558 (1993); G. Kresse and J. Hafner, Phys. Rev. B **48**, 13115 (1993).

[23] G. Kresse and J. Furthmuller, Comput. Mater. Sci. **6**, 15 (1996).

[24] M. D. Segall, P.L. D. Lindan, M. J. Probert, C. J. Pickard, P. J. Hasnip, S. J. Clark, and M. C. Payne, J. Phys.: Condens. Matter **14**, 2717 (2002).

[25] G. P. Srivastava and D. Weaire, Advances in Physics. **26**, 463 (1987).

[26] G. B. Bachelet, D. R. Hamann, and M. Schluter, Phys. Rev. B **26**, 4199 (1982).

[27] G. Kerker, J. Phys. C **13**, L189 (1980).

[28] D. Vanderbilt, Phys. Rev. B **41**, 7892 (1990).

[29] G. Kresse and J. Joubert, Phys. Rev. B **59**, 1758 (1999).

[30] P. E. Blochl, Phys. Rev. B **50**, 17953 (1994).

[31] R. Car and M. Parrinello, Phys. Rev. Lett. **55**, 2471 (1985).

[32] G. Kresse and J. Furthmuller, Phys. Rev. B **54**, 11169 (1996).

Chapter 3

High-*k* gate dielectric/Si interfaces: epitaxial ZrO_2 on Si(001)

3.1 Introduction

Zirconia (ZrO_2) satisfies almost all the requirements for dielectric material and is considered along with another group IVB metal oxide, HfO_2, as the most promising high-*k* dielectric to replace conventional SiO_2 as the gate dielectric. ZrO_2 has a moderate high *k* value (25) and a relative large band gap (~5.8 eV). The conduction band offset, the electron barrier height from Si channel to gate dielectric oxide, was estimated to be around 1.5 eV from charge neutrality level (CNL) model, [1] which is far above the minimum band offset requirement (>1.0 eV). Furthermore, ZrO_2 has a higher heat of formation than that of SiO_2, which indicates ZrO_2 should be stable above Si channel, not reacting with Si to form SiO_2 or a silicide from a thermodynamic point of view.[2, 3]

A substantial amount of investigation has gone to ZrO_2 as it has shown its attractive properties as candidate to replace SiO_2. Copel *et al.* [4] found that ZrO_2 films grown by atomic layer chemical vapor deposition (ALCVD) was stable with respect to both silicidation and silicate formation up to the temperature as high as 900^{o}C. However, a disadvantage of this industry-preferred ALD method is that it is usually carried out on a "chemical oxide" (SiO_2) surface as nucleation occur much more readily on a slightly-oxidized Si surface than on H-terminated surface. Lin *et al.* [5] observed that Zr silicate was formed at the ZrO_2/Si interface after ZrO_2 was deposited

by ALD at 360°C. Zr-silicate has a relatively higher dielectric constant than SiO_2, although still smaller than that of ZrO_2. However, Wilk and Muller[6] reported recently that no Hf-silicate intermixing is detected at the ALD-deposited HfO_2/Si interface after 600°C annealing in oxygen ambient. Copel *et al.*[7] also demonstrated the extremely low levels of Hf incorporation at HfO_2/Si interfaces. In addition, initial studies of ZrO_2/Si interfaces reported an interlayer of SiO_2 rather than Zr-silicate.[8] From the above numerous investigations that have addressed the interfacial composition of ZrO_2 or HfO_2/Si interfaces, we can conclude that the chemical composition of the interfacial layer at ZrO_2 (or HfO_2)/Si interfaces obtained by ALD or CVD is prevailed by SiO_2. The metal (Zr or Hf) incorporation is at a low level if it exists there. The existence of such an interfacial layer of SiO_2 limits the ultimate equivalent oxide thickness (EOT) that can be achieved, as the overall EOT is given by the series capacitances of SiO_2 and high-*k* material. The *k* value of SiO_2 is so small (3.9) that a SiO_2 interfacial layer can rapidly use up the EOT allocation and this serves as a severe impediment for the continued scaling of EOT to sub-1 nm thickness for the coming sub-45 nm node MOSFET devices.

As the oxides of Zr or Hf with an amorphous interface layer (SiO_2 or metal silicate) will no longer be tolerable after one or two generations, epitaxial crystalline metal oxide with atomically well-defined interface with Si will be required ultimately. However, the issue concerning the film growth process and interface structure of oxide on semiconductors is a very crucial step for the implementation of this new structure and has not been well understood yet.

In this chapter, we will study the epitaxial ZrO_2 on silicon as alternative gate dielectric, including film growth, interface characterization and electronic structure calculations.[9] The atomic and electronic structures at the ZrO_2/Si interfaces will be

determined using a combination of characterization tools, including high-resolution transmission electron microscopy (HRTEM) and X-ray photoelectron spectroscopy (XPS), in conjunction with first-principles calculation based on density functional theory (DFT).

3.2 Experimental characterizations of epitaxial ZrO_2 on Si

Crystalline zirconia has three polymorphs which are, in sequence of stability from low to high temperature, monoclinic phase (*m*-ZrO2), tetragonal phase (*t*-ZrO2) and cubic phase (*c*-ZrO2).[10] The latter two phases are metastable under ordinary temperatures and pressures. For temperatures higher than 2643 K zirconia adopts a cubic fluorite structure. Yttrium doping can be employed to completely stabilize the cubic modification at room temperature.[11] Cubic yttrium-stabilized ZrO_2 (YSZ) has a lattice constant of 5.15 Å, which is ~5% smaller than that of Si (5.43 Å). In our experiments, yttrium-stabilized ZrO_2 (YSZ) single crystal target was used to deposit films by pulsed laser deposition (PLD) technique.[12] Yttrium is about 7% in the target to stabilize the film as cubic structure. The Si substrates are ultrasonically cleaned in dilute nitric acid and then thoroughly rinsed. In this treatment the native amorphous SiO_2 layer remains on the substrates. The deposition is operated at a substrate temperature of 700~730^{o}C in an ambient oxygen deficient pressure of $2.0\sim6.0\times10^{-4}$ Pa. A KrF excimer laser (pulse duration 30 ns, wavelength 248 nm) was operated with a fluence of 1.5 J/cm^2 and laser frequency of 3 Hz on target surface.

To reveal the interface structure between YSZ layer and Si substrate as well as structural defects in YSZ thin films at atomic level, cross-sectional transmission electron microscopy samples were prepared following standard procedures including

cutting, gluing and ion milling. The microstructure of the films was investigated using HRTEM (Philips CM 300, with point resolution 1.7 Å). Photoelectron spectroscopy studies were performed in a VG ESCALAB 220i-XL system. All spectra were obtained in the constant pass energy mode with pass energy of 10 eV using monochromatic Al $K\alpha_1$ source (1486.6 eV). The binding energy scale was calibrated with pure gold, silver and copper by setting the Au $4f_{7/2}$, Ag $3d_{5/2}$ and Cu $2p_{3/2}$ at binding energy of 83.93, 368.26 and 932.67 eV, respectively.

3.2.1 Epitaxial ZrO_2/Si interface structure on atomic scale

Cross-sectional TEM has been performed to characterize the YSZ-Si heterostructures. Fig. 3.1a is a typical cross-sectional HRTEM image of epitaxial YSZ thin film on Si(100) substrate taken with the incident electron beam parallel to Si[110]. It is very clear that the epitaxial relationship between YSZ and Si is a high-symmetry cube-on-cube structure. The electron diffraction pattern of YSZ/Si interface (Fig. 3.1d) shows that the orientation relationship between YSZ and Si is YSZ(001)//Si(001) and YSZ[011]//Si[011]. The most obvious point in Fig. 3.1a is that the YSZ thin film grows epitaxially on Si(100) substrate, without the formation of interfacial amorphous oxide layer at the interface in this case.

We proposed a possible interface structure formed by c-ZrO2 and Si with a –Si-Si-O-Zr-O- interfacial atomic structure, as shown in Fig. 3.1c. Based on the interface structure model shown in Fig. 3.1c, the simulated HRTEM image of crystalline YSZ on silicon (in Fig. 3.1b) is in good agreement with experimental HRTEM image (Fig. 3.1a), indicating that the film on silicon is single crystal cubic YSZ film.

The lattice mismatch between YSZ[011] and Si[011] is as high as 5%, which would induce many interface dislocations to relax the lattice mismatch induced strain.

The average distance between two adjacent interface dislocations can be expected to be

$$d = d_{YSZ\{110\}} d_{Si\{110\}} / (d_{YSZ\{110\}} - d_{Si\{110\}}) \quad (3.1)$$

where $d_{YSZ\{110\}}$ and $d_{Si\{110\}}$ are the inter-planar distances for YSZ and Si respectively. The calculation of the Eq.(3.1) gives $d = 7.62$ nm, which equals 19 $d_{YSZ\{110\}}$ or 18 $d_{Si\{110\}}$.

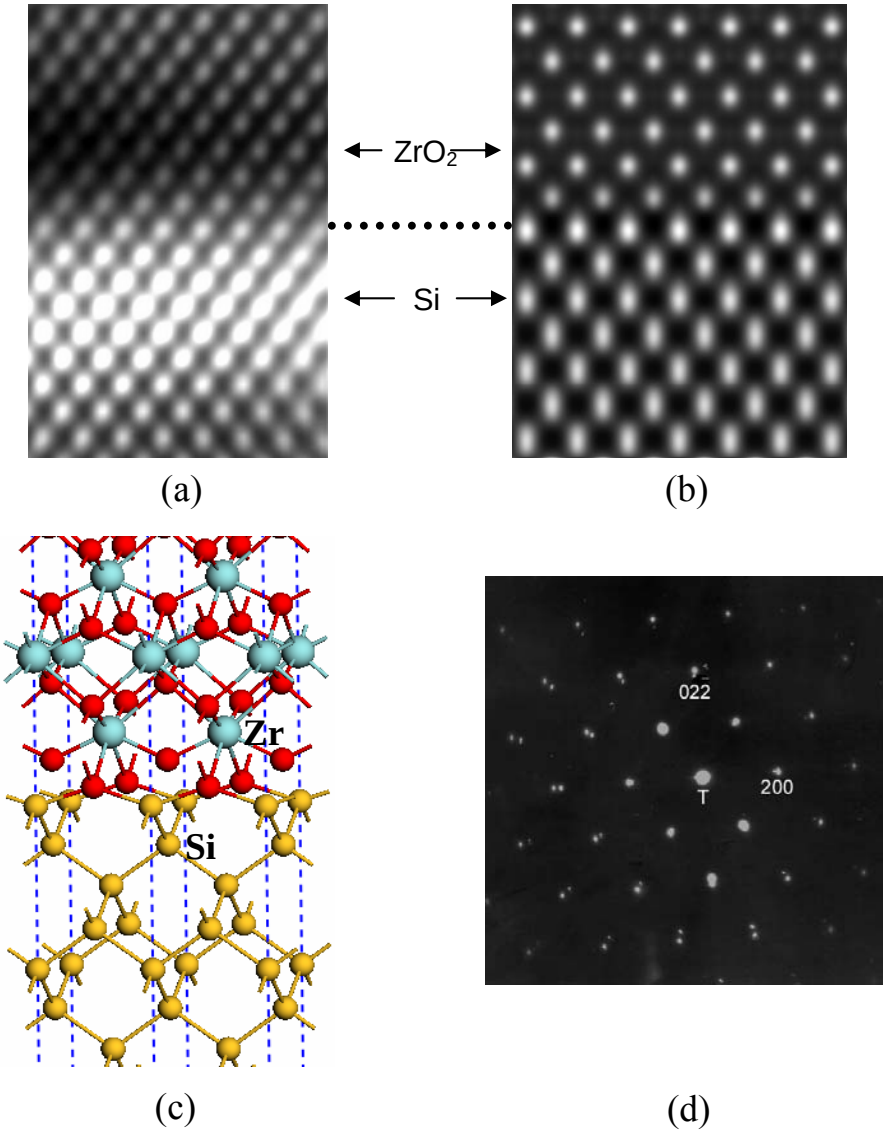

Fig. 3.1 (a) HRTEM image of the interface between YSZ and Si(001) substrate, showing the high symmetry cub-on-cube epitaxial relationship with YSZ(001)//Si(001) and YSZ[011]//Si[011]; (b) Simulated HRTEM image by JEMS program; (c) proposed ZrO_2/Si interface structure; and (d) the electron diffraction pattern for YSZ on Si(001).

Thus the interface dislocations are expected on the oxide side, which is in agreement with the experiment result, as shown in Fig. 3.2. The interface dislocations are revealed by numbering the atomic columns on both YSZ and Si sides. In the interface region (~38.5 nm in width) shown in Fig. 3.2, five dislocations were identified. A burgers circuit around the dislocation indicates that the Burgers vector is **a/2** [$\bar{1}$10], with **a** the lattice constant of the YSZ layer. The lattice misfit between the Si substrate and YSZ thin film is relaxed into local regions of coherent fit separated by the disturbed atomic sequence.

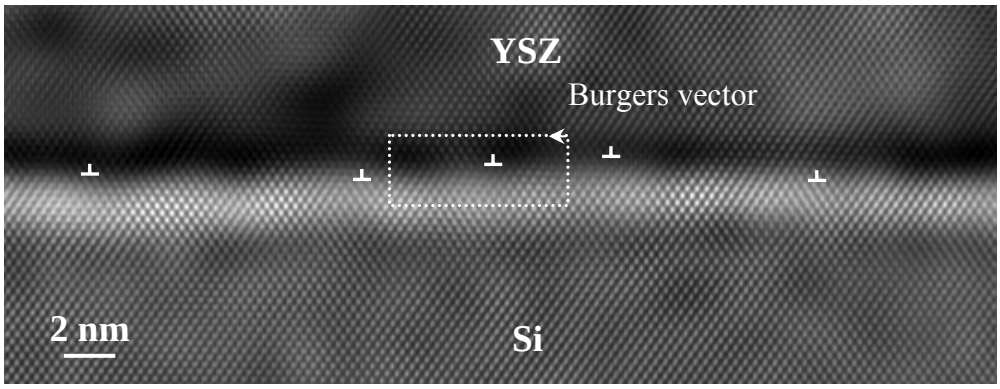

Fig. 3.2 Interface dislocation with the Burgers vector **a/2** [$\bar{1}$10] on the Si side to accommodate the misfit of lattice constants between the YSZ thin film and the Si substrate. Statistically insignificant frequency components were removed by Fourier filtering with a large circular aperture.

In general, the thickness of native amorphous SiO_2 on the surface of Si wafer is about 1.0 nm. Although we did not conduct any acid-etching process on the natively oxidized Si substrate, no amorphous SiO_2 or Zr-silicate layer was observed at the YSZ/Si interface in the cross-sectional TEM image. This phenomenon is considered as the result of the two possible reaction pathways. One is related to the reaction of metallic Zr ions with SiO_2 on the surface of Si wafer under low oxygen pressure and high temperature conditions, where metallic Zr ions absorb the oxygen atoms in the

SiO_2 layer and volatile SiO byproduct is formed:

$$2SiO_2 + Zr \rightarrow ZrO_2 + 2SiO\uparrow \quad (3.2)$$

Thus the atoms in the native amorphous SiO_2 layer on the surface of Si wafer will be rearranged. Rubloff *et al.*[13] found that the critical oxygen partial pressure above which the silicon oxide layer remains stable at 730°C is about 7×10^{-3} Pa. Thus the desorption of SiO_2 overlayer is expected for lower growth partial pressure 5×10^{-4} Pa during the initial deposition process.

The other possible reaction involves oxygen vacancies (V_O). From thermodynamic point of view, it is energetically more favorable to form Vo in SiO_2 than in ZrO_2, which indicates that oxygen-deficient ZrO_2 grown on top of SiO_2 will consume oxygen from SiO_2 and reduce SiO_2 to Si.[14] This reaction has been demonstrated by Copel and Reuter[15] on the growth of HfO_2 by Hf deposition in an oxidizing atmosphere at temperatures as low as 500°C, which is far below the regime associated with SiO volatility.

The former reaction is the dominant one at high temperatures where SiO is very volatile, while the latter is the main reaction at relatively low temperatures. Both of these reactions consume oxygen in SiO_2 interfacial layer and as a result, the native amorphous SiO_2 layer will be reduced or even eliminated in lower partial pressure deposition process. At the same time, the atoms on the surface of Si will be rearranged and a crystalline YSZ film forms with epitaxial structure relative to Si substrate. Here we note that an appropriate low oxygen partial pressure is essential for the two reactions. With higher oxygen partial pressure, SiO_2 interfacial layer cannot be consumed thoroughly; but oxygen partial pressure also needs to be high enough to avoid the formation of silicide layer at the interface, which is detrimental for devices.

3.2.2 Band offsets at epitaxial ZrO_2/Si(001) interfaces

In order to measure the band alignment at the epitaxial ZrO_2/Si interface, an yttrium-stabilized ZrO_2 (YSZ) film with the thickness of 3.0 nm was grown on silicon (001). As the sampling depth of *x*-ray photoelectron with energy of 1486.6 eV can be up to ~10 nm, the information from both the film and substrate can be seen from photoemission spectra simultaneously.

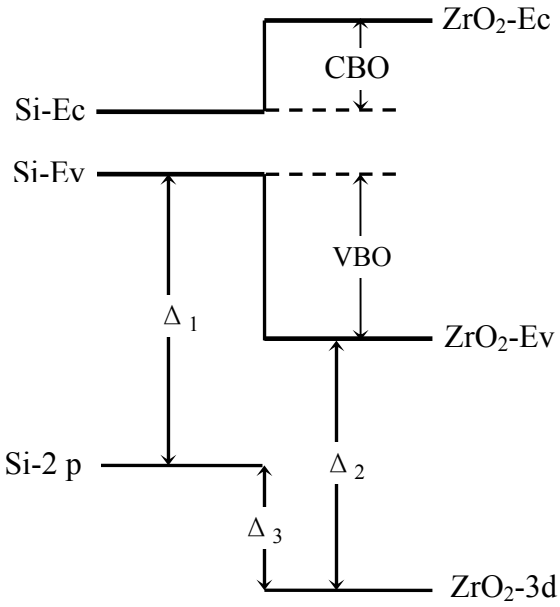

Fig. 3.3 Schematic representation of a band alignment problem at heterojunctions.

We applied the photoemission-based method of Kraut *et al.* [16, 17] to determine the valence and conduction band discontinuities. The procedure to measure the band offsets is shown in Fig. 3.3. Firstly, the energy differences between the valence band maximum (Ev) and the core level centroids were measured in respective bulk materials (Δ_1 for bulk-Si and Δ_2 for bulk-ZrO_2). Then the core levels (Si $2p_{3/2}$ and Zr $3d_{5/2}$ for Si substrate and YSZ thin film respectively) for the thin film and substrate were

simultaneously measured from the ZrO_2/Si contact. These core levels from the interface were used to align the energy bands in the two sides. In this procedure, there is an important assumption, that is, the energy differences (Δ_1 for bulk-Si and Δ_2 for bulk-ZrO_2) are kept constant for a given material. This assumption is essentially right, which has been checked carefully for various materials [16] and serves as the basis for this band alignment method for heterostructures.

In using the above procedure to measure valence band offset, it is essential to accurately determine the valence band maximum for semiconductor or oxide from XPS valence band spectra. One simple and accurate method is the linear method,[18] by finding the intersection of two straight line segments, of which one fits to the linear portion of the valence band leading edge and one fits to the background channels between the VBM and the Fermi level. In Fig. 3.4 we show how the VBMs for Si(001) and YSZ(001) surfaces can be determined accurately by this linear method from XPS valence band spectra.

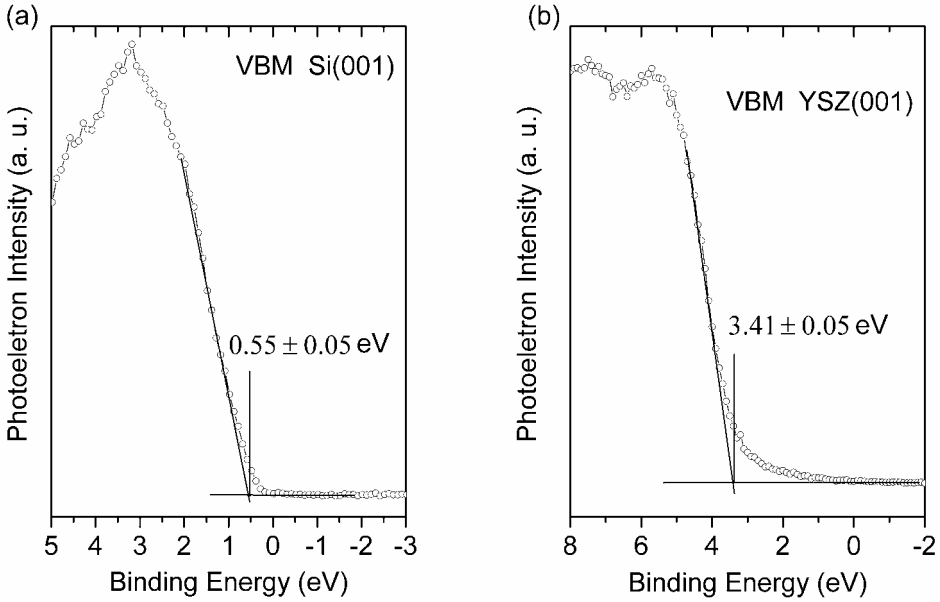

Fig. 3.4 Valence band spectra for (a) Si(001), and (b) YSZ(001).

In Fig. 3.5 we show the core-level and valence band spectra for bulk Si(001), bulk YSZ(001), and YSZ/Si(001) heterojunctions used to determine the band offsets. The energy bands in Fig. 3.5 have been aligned using Zr $3d_{5/2}$ and Si $2p_{3/2}$ core levels as the reference levels. In addition, an important feature of Si 2p spectra is the absence of the bonding peak corresponding to Si in SiO_2 or silicate, which is normally in a higher energy position (100~104 eV) than that for element Si (~99.5 eV). There is only one Si 2p spin-orbital doublets, which originates from pure Si substrate. This finding confirms the result obtained from the HRTEM images shown in Fig. 3.1a, that is, there is no interfacial SiO_x or silicate layer between the 3.0 nm thick YSZ ultra-thin film and Si substrate.

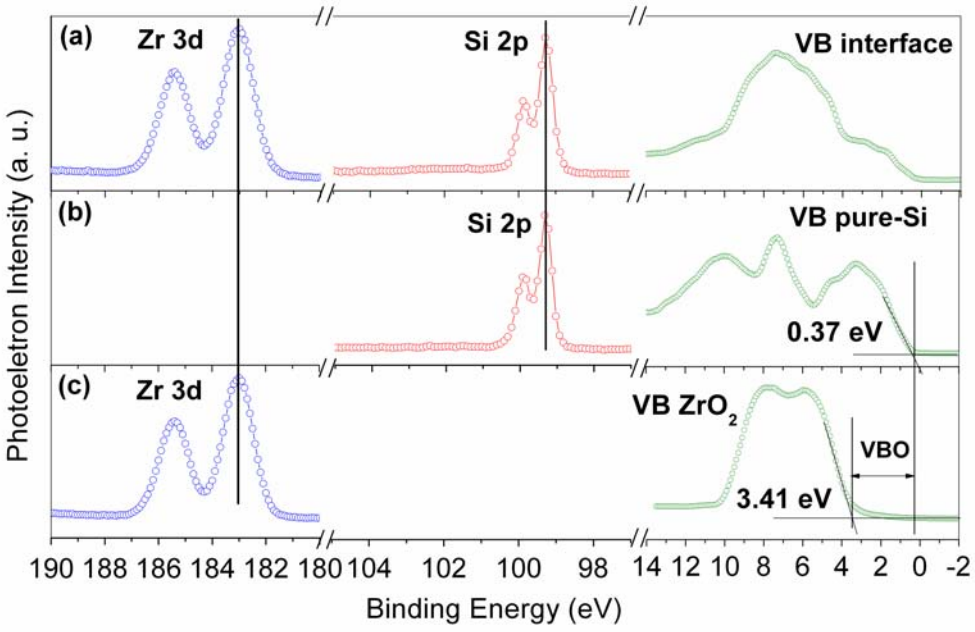

Fig. 3.5 Core-level and valence band photoelectron spectra for (a) 30 Å epitaxial YSZ on Si (001), (b) H-terminated Si (001) surface, and (c) YSZ (001) surface. The energy bands have been aligned using Zr 3d and Si 2p core levels as the reference levels.

In Fig. 3.5, the energy difference between the valence band edges and the energy position of Si $2p_{3/2}$ peak was measured to be 98.70 ± 0.05 eV for Si(001) substrate, which is in good agreement with the value we obtained previously.[19] It is worth noticing that this value is slightly lower than that measured by Yu *et al.* [20] (98.95 eV for n-Si) and that obtained by Chambers *et al.* [21] (98.90 eV, for n-Si; and 98.98 eV, for p-Si). They measured the energy difference between the valence band edges and the centroids of Si 2p, instead of Si $2p_{3/2}$. The resolution of XPS in our experiment is high (up to 0.45 eV) enough to distinguish the spin-orbital doublets of Si 2p even for the buried Si substrate (the energy separation between Si $2p_{1/2}$ and Si $2p_{3/2}$ is only 0.6 eV). Thus we used the energy position of Si $2p_{3/2}$ peak instead of the centroids of the whole Si 2p as the reference level. The energy difference between Zr $3d_{5/2}$ and the VBM of ZrO_2 was measured to be 179.53 ± 0.05 eV for YSZ(001) surface and the energy difference between Zr-$3d_{5/2}$ and Si $2p_{3/2}$ was determined to be 83.67 ± 0.05 eV for 30 Å epitaxial YSZ on Si (001). Then, the valence band offset was determined to be 3.04 ± 0.05 eV by using the equation

$$VBO = (E_{Zr-3d_{5/2}} - E_{Si-2p_{3/2}})_{ZrO_2/Si(001)} - (E_{Zr-3d_{5/2}} - E_v)_{ZrO_2(001)} + (E_{Si-2p_{3/2}} - E_v)_{Si(001)} \quad (3.3)$$

with $E_{Zr-3d_{5/2}}$ the energy position of Zr $3d_{5/2}$, $E_{Si-2p_{3/2}}$ the energy position of Si $2p_{3/2}$, and E_V the valence band edge.

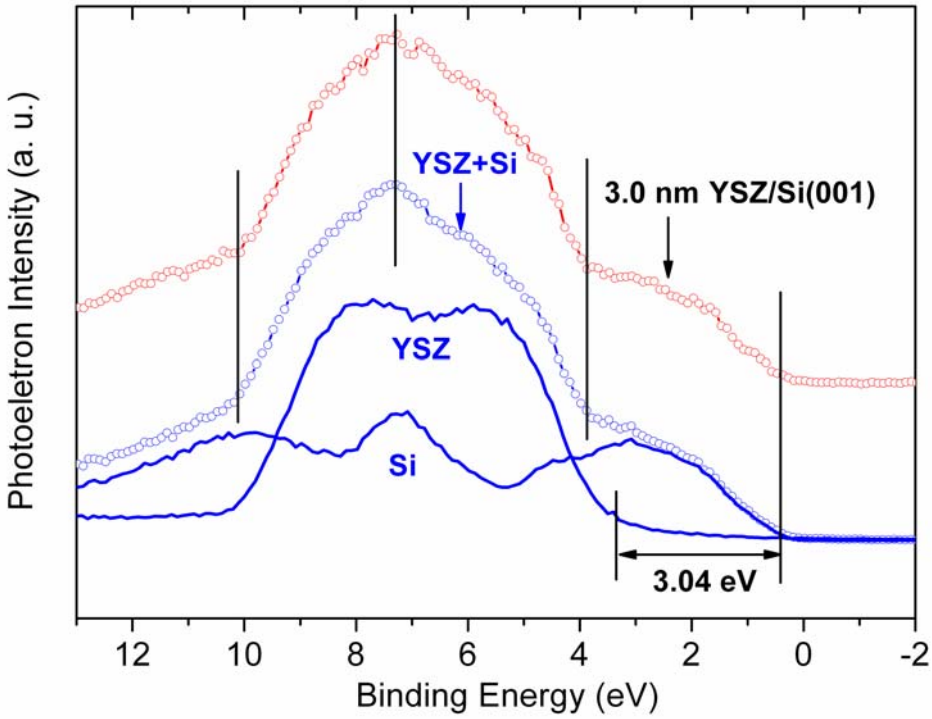

Fig. 3.6 Comparison between the valence band for the actual 3.0 nm YSZ/Si interface and the simulated valence spectra (YSZ+Si). The latter was obtained by summing the valence band for Si (001) and YSZ (001) surface in their respective energy positions aligned by the core-level-based method.

To check the above core-level-based method, we simulated the valence band spectra of the 3.0 nm YSZ/Si interface by summing the appropriately weighted spectra for clean Si (001) and YSZ (001) surface in their respective energy positions shown in Fig. 3.5. The result of this check is shown in Fig. 3.6. The simulated valence spectra (YSZ+Si) is in good agreement with that for the actual 3.0 nm YSZ/Si interface, which demonstrates that the above core-level-based method can accurately determine the valence band offset for heterostructures.

With the measured valence band offset, the conduction band offset (CBO) can be obtained by the simple equation

$$CBO = (E_{g-ZrO2} - E_{g-Si}) - VBO \tag{3.4}$$

where E_{g-ZrO2} and E_{g-Si} are band gaps for ZrO_2 and Si respectively. The band gap of ZrO_2 was determined to be ~5.82 eV using the ultra-violet adsorption as shown in Fig. 3.7, while that for Si is 1.12 eV. Therefore, the CBO for ZrO_2/Si interface is 1.66 eV.

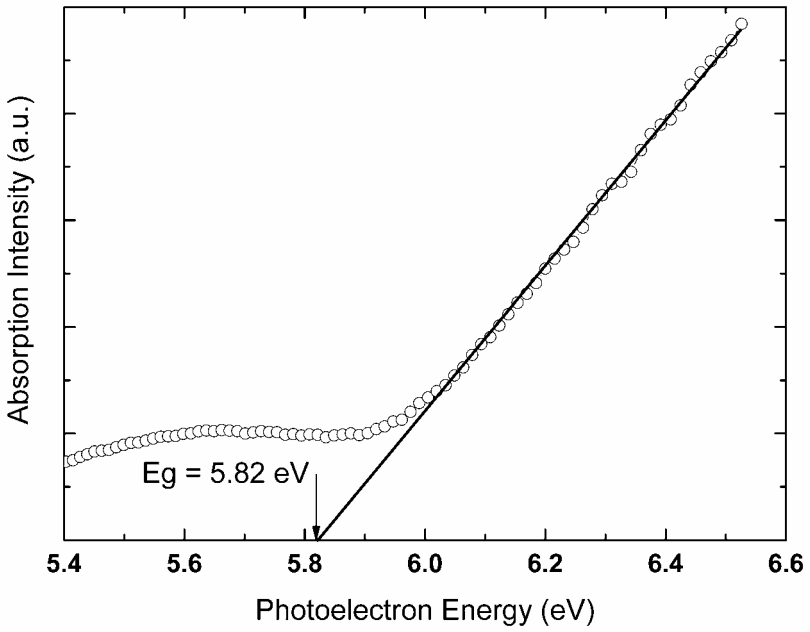

Fig. 3.7 UV absorption spectrum for 500 nm YSZ thin film on Al_2O_3 substrate.

The valence band offset (3.04 ± 0.05 eV) we obtained here for epitaxial ZrO_2/Si interface is in good agreement with the value (3.15 eV) measured by Miyazaki *et al.* [22] for thermal evaporation deposited ultra thin amorphous ZrO_2 on Si(001) interface. For ZrO_2/SiO_x (~0.5 nm)/Si stacks with an ultrathin SiO_2 buffer layer between ZrO_2 and Si, Miyazaki *et al.* [22] obtained a relatively larger value of 3.35 eV. Fulton *et al.* [23] argued that the charge layer in the SiO_x buffer layer would give rise to large changes in the band alignment. They found an astonishing valence band maximum shift for ZrO_2 on Si with SiO_2 buffer layer between them, as large as 2.0 eV. The VBO was shift from

0.95 eV for the as-grown ZrO_2 on Si to 3.0 eV for the post-annealing sample. The band alignment is so dependant on the interface structures for the amorphous ZrO_2 on Si stacks that it inspires us to consider what are the situations for epitaxial ZrO_2/Si interfaces, where there is no silicon oxide or silicate buffer layer between them.

3.3 Atomistic modeling for ZrO_2/Si interfaces

Recently, theoretical approach based on the first-principles density functional theory has been used to study interfacial properties of metal oxide dielectric/Si interface on atomic level[24−28]. The general bonding rules proposed by Robertson and Peacock[29] are very instructive in understanding the atomic structure of oxide/Si interfaces, and such rules have been tested for several model interfaces of ZrO_2/Si in free-standing mode, in which both the oxide and Si were relaxed simultaneously in DFT calculations. Puthenkovilakam *et al.* [30] studied the detailed atomic and electronic structures of ZrO_2/Si interfaces using first-principles calculations. The valence band offset evaluated from their interface model agrees with their XPS experimental results (3.65 eV)[31], which indicated that the conduction band offset is smaller than the critical value for high-*k* dielectric applications. However, there have been other reported experimental values for the valence band offsets, e.g., 3.0 eV in Ref. 16 and 3.15 eV in Ref. [32]. Such variations indicate that band offsets are deposition-process-dependent. Thus, further study is required in order to clarify the dependence of band offset on interface structure.

In this section, atomic structure and electronic properties of various ZrO_2/Si interface models are studied.[33] The stabilities of these interfaces are compared to explore the possibility of atomic control of interface structure by altering the chemical environment (oxygen chemical potential). The valence band offsets for the various

interface structures are calculated to determine the dependence of band offset on interface structures, thus to provide information for band offset engineering with these materials.

3.3.1 ZrO_2/Si interface structures

DFT calculations were performed by using the VASP[34,35] code and partially checked by CASTEP[36], with Vanderbilt ultrasoft pseudopotentials[37] and the generalized gradient approximation (GGA)[38] for the exchange-correlation potential. Previous *ab initio* studies of bulk zirconia[39] and surface[40] have shown that it is necessary to include generalized gradient corrections in order to accurately describe the bulk energy differences between the various polytypes of ZrO_2 and the surface energy of ZrO_2. In addition, GGA is more suitable to studies of interfaces which represent a more inhomogeneous chemical environment. A cutoff energy of 350 eV was used in the plane wave expansion of electron wavefunction. For the primitive cell of bulk tetragonal ZrO_2 (*t*-ZrO2), we used an 8×8×6 Monkhorst-Pack k-mesh, and for the (1×2) interface supercells (3.858Å×7.716Å×35.000Å), an 8×4×1 k-mesh. Electronic optimization was performed using a fairly robust mixture of the blocked Davidson and RMM-DIIS algorithm as implemented in VASP. Ionic relaxation was performed using the conjugate gradient (CG) algorithm. Density of states (DOS) were calculated with finer k-meshes using the tetrahedron method with Blöchl corrections as implemented in VASP.

Zirconia has three polymorphs which are, in sequence of stability from low to high temperature, monoclinic phase (*m*-ZrO_2), tetragonal phase (*t*-ZrO_2) and cubic phase (*c*-ZrO_2). Our calculation correctly reproduced the energetic hierarchy among the three phases. The *m*-ZrO_2 is favored over *t*-ZrO_2 by 77 meV/formula unit and over *c*-ZrO_2

by 156 meV/formular unit, which are in excellent agreement with other DFT calculations and the experimental results[22]. Both *c*-ZrO_2 and *t*-ZrO_2 are suitable for epitaxial growth on Si. In this study, *t*-ZrO_2 is used as the building-block. The simple reason is that the phase transition from *c*-ZrO_2 to *t*-ZrO_2 is barrierless when both are imposed by the tetragonal symmetry. The un-strained crystalline structures are well reproduced with *a*=5.456 Å for Si and *a*=3.650 Å, *c/a*=1.449, dz=0.0512 for *t*-ZrO_2, compared to the experimental values of *a*=5.45 Å for Si and *a*=3.64 Å, *c/a*=1.448, dz=0.065 for *t*-ZrO_2[41]. These theoretical lattice constants agree well with those of other DFT calculations.[20, 42] For the epitaxial growth of *t*-ZrO_2 on Si (001) substrate, the *t*-ZrO_2 is in-plane strained with $a_{//} = a_{Si}/\sqrt{2}$ =3.858 Å and the lattice parameter *c* in the interface normal contracted to 5.200 Å accordingly. A uniaxial strain along [001] will not change the symmetry of *t*-ZrO_2 ($P4_2/nmc$), but it leads to two dramatic changes in the band structure of *t*-ZrO_2, as shown in Fig. 3. 8. One is the substantial reduction of the indirect band gap, from 4.0 eV to 2.9 eV. The other is the disappearance of the CB gap between Zr 4d (x^2-y^2, z^2) and Zr 4d (xy, yz. xz) states.

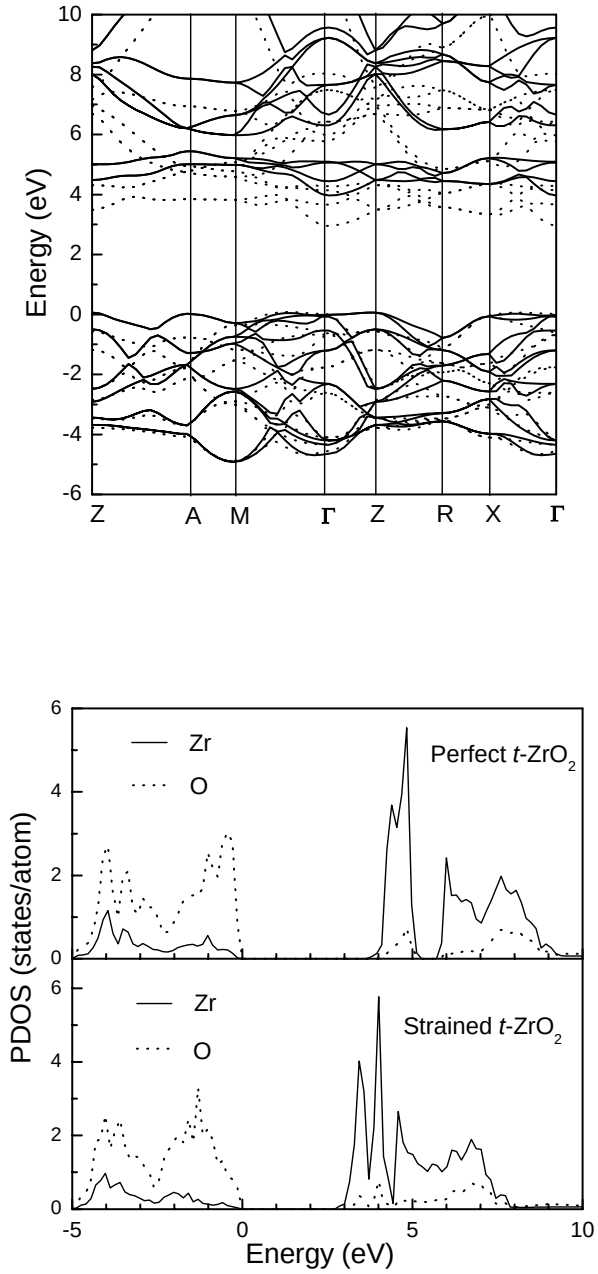

Fig. 3.8 Band structures (top) and PDOS (down) for perfect *t*-ZrO_2 and in-plane strained *t*-ZrO_2. Solid lines: perfect *t*-ZrO_2; dotted lines: in-plane strained *t*-ZrO_2.

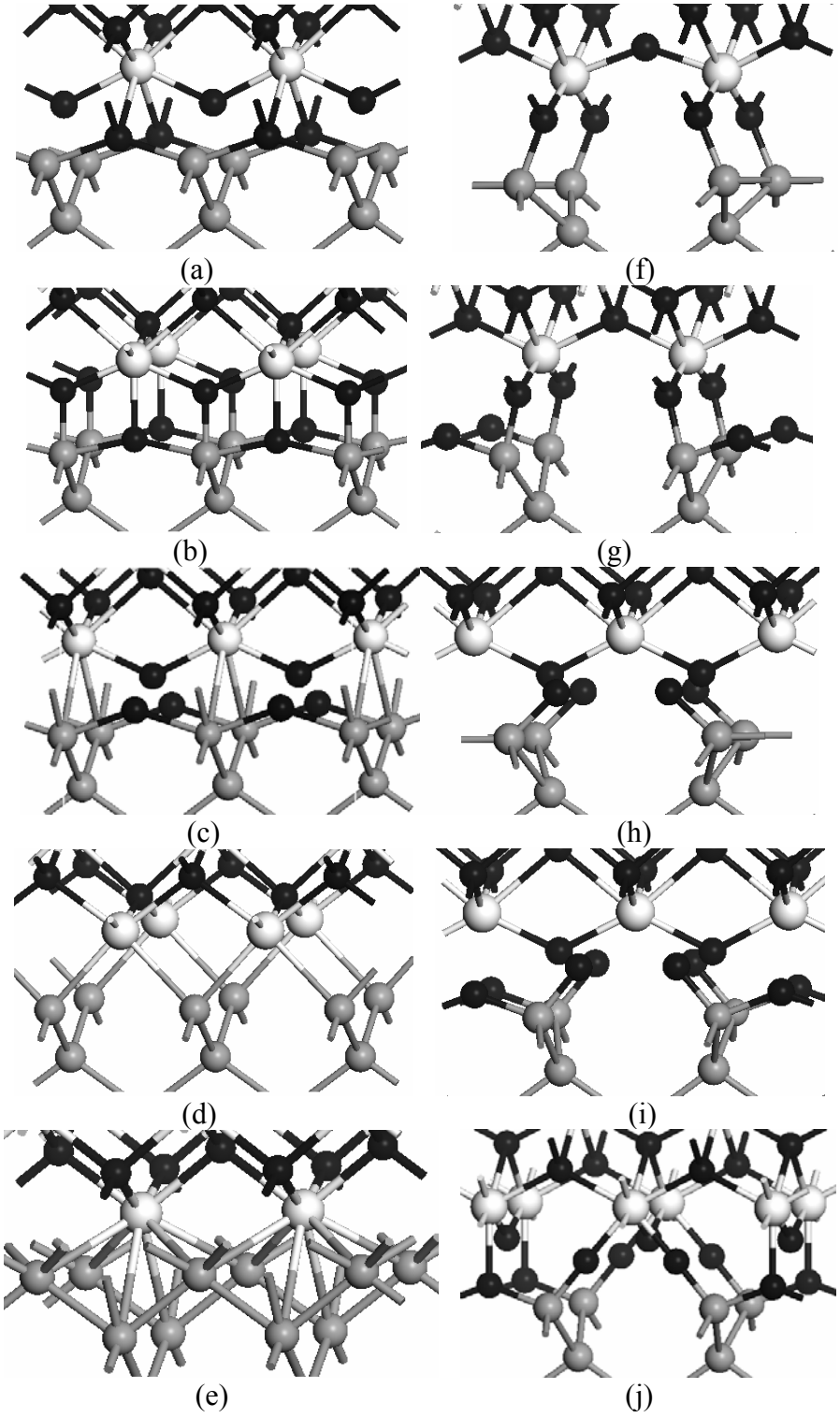

Fig. 3.9 Model interfaces for *t*-ZrO2/Si, viewed in the (110) plane (Grey: Si; Black: O; Light: Zr).

For the interface structure of epitaxial *t*-ZrO_2 (001) on Si (001), there are many possibilities even for abrupt interfaces. We chose the interface structures based on the general bonding rules for Si and ionic oxides interfaces, recently proposed by Robertson and Peacock[10]. The general bonding rules state that: (1) terminate with enough excess oxygen so that the interfacial Si DBs are formally Si^+ and empty, or (2) terminate with excess metal so that the Si DBs are formally Si^- and filled. The rules set valence requirements for Si and ionic interfaces. Such simple electron-counting arguments aim to give insulating interfaces because a perfect interface with no electronic defects and no midgap interface states is a key criterion for high-k applications. Our detailed studies on various ZrO_2/Si model interfaces offer a test for such rules. Both the unreconstructed Si surface and the 2×1 reconstructed Si surface are considered as the growth templates.

The various interface structures are shown in Fig. 3.9. While many other interface structures, such as that with a mixed Si-Zr layer in Ref. 24, are possible, we consider only the abrupt interfaces in this study. Some of the ZrO_2 on unreconstructed Si surface structures (**a**, **b**, **d** and **e**) are proposed by Robertson and Peacock [10] and structure **f** was proposed by Puthenkovilakam *et al.* [12] Structure **a** is an ideal Si:OOZrO interface. Two adjacent Si dangling bonds are firstly saturated by a bridge O. Then the closed OZrO shell is stacked above it with the interface Zr standing on the shoulder of the two bridging Os. To get structure **b** and **c**, we simply translate the OZrO stacks in the interface plane. For **b**, interface Zr stands on the head of the bridge O and for **c**, on the shoulder of two interface Si atoms. The surface Si dangling bonds can also be saturated by metal atoms, such as structure **d** and **e**. Such silicide interfaces are expected to be metallic. We also consider models formed by the *t*-ZrO_2 and the 2×1 reconstructed silicon surface structures. Structure **f** and **h** are such structures with the

dangling bond on each Si surface atom first saturated by an O atom. Structure **g**, **i** and **j** are three interface structures with oxidized Si-dimmer. All the five structures (**f**, **g**, **h**, **i**, **j**) are O-terminated (the surface Si are saturated by O). The Zr-terminated structures on the 2×1 reconstructed silicon surface are not considered because earlier DFT calculations[43] showed that the adsorbed Zr is thermodynamically unstable against the formation of bulk silicide $ZrSi_2$, which are technologically unfavorable.

The ZrO_2-Si interfaces are modeled following a supercell approach with repeated slab geometry. The slab includes 8 layers of Si, 5 layers of *t*-ZrO_2 and at least 10Å vacuum. The bottom Si layer is saturated with two hydrogen atoms per Si. The positions of the hydrogen atoms and the last Si layer are fixed during relaxation. All the other atoms are allowed to move to minimize the total energy without any symmetry restriction. The pre-strained *t*-Zr_{O2} ($\sqrt{2}$ a=5.456Å, c=5.200Å) and unstrained Si were used as the building blocks. In this case, the relaxations occur only in the first two interface-neighboring (for *t*-ZrO_2 also the surface) layers.

3.3.2 Interface energetics

The relative stability of an interface is given by its formation energy. The smaller the interface formation energy, the more stable the interface structure. For the repeated slab structure, the interface formation energy can be expressed as

$$E_{form} = \frac{E_{total} - [nE_{ZrO_2} + mE_{Si} + E_{other} \pm l\mu_O]}{A} \tag{3.5}$$

where E_{total} is the DFT total energy of the interface supercell, *n* and *m* are the numbers of Si and ZrO_2 bulk units, respectively, E_{Si} and E_{ZrO_2} the total energy per Si and ZrO_2 bulk unit respectively, E_{other} includes the upper surface energy of ZrO_2 and the energy related to the H atoms, *l* the number of oxygen atoms added (+, for O-rich situation)

or removed (-, for Zr-rich) to create the interface, μ_O the chemical potential of oxygen in the interface supercell, and A the basal area of the interface supercell. E_{ZrO_2} corresponds to the in-plane strained *t*-ZrO_2 bulk (in the same strain state as in the slab), so the calculated interface formation energy is volume-independent.[44] We used the DFT total energies instead of the Gibbs free energies, since the vibrational entropy contributions and enthalpy changes due to finite temperature are almost the same for different structures and will not change the relative stability of different structures significantly. For the various repeat slab interface supercell structures being considered, [$nE_{ZrO_2} + mE_{Si} + E_{other}$] is the same and can also be counteracted when the relative interface energies are compared. The key problem is to evaluate the chemical potential of the added or subtracted O atoms. Here we utilized the method which has been widely used to calculate the surface energy of metal oxide[45, 46, 47]. We assumed that Zr bulk and O_2 gas reservoirs are in thermal equilibrium with the ZrO_2 thin film (if this is not the case, the ZrO_2 thin film would either grow or decompose). This requires

$$2\mu_O + \mu_{Zr} = E_{ZrO_2} \tag{3.6}$$

where E_x and μ_x are the DFT total energies and chemical potentials of particle *x*, respectively. By defining the formation enthalpy (by convention is negative) as

$$H_f = E_{ZrO_2} - (E_{O_2} + E_{Zr}) \tag{3.7}$$

where E_{O_2} and E_{Zr} are the DFT total energies per oxygen molecule and Zr atom in *hcp*-Zr bulk, respectively.

we get

$$(2\mu_O - E_{O_2}) + (\mu_{Zr} - E_{Zr}) = H_f \tag{3.8}$$

Because of the simple fact that the chemical potential for each element cannot be above that of the bulk (or gas) element phase[48], μ_O is allowed to vary over the range

$$\frac{1}{2}(E_{O_2} + H_f) \le \mu_O \le \frac{1}{2}E_{O_2} \tag{3.9}$$

Once the bound for the chemical potential of oxygen has been found, the interface formation energy can be expressed as a function of μ_O, as in Eq. (3.5). In the following calculation, all energies and chemical potentials are referenced to $\frac{1}{2}E_{O_2}$.

Following the approach outlined above, we firstly calculated the relative interface formation energies for the ten interface structures as a function of oxygen chemical potential, with respect to the stoichiometric structure **f**. Then the absolute formation energy of structure **f** was determined to be 0.079 eV/ Å ^{2}, using the supercell structure without vacuum. Finally, the absolute formation energies of the various structures as a function of μ_O are shown in Fig. 3.10. The dashed lines are for unreconstructed Si surface template, while the solid lines for the 2×1 reconstructed Si surface template. The left and right boundaries of Fig. 3.10 correspond to the limiting cases of metallic zirconium and molecular oxygen respectively. The most important features of Fig. 3.10 are: (i) Among all the interface structures, structure **b** seems to be the most stable one except in the very low O chemical potential region. So this structure is most possible for our HRTEM image[4]; (ii) the Zr-terminated interface structures only exist in very low oxygen partial pressure; (iii) for the reconstructed template, the most stable structure is O chemical potential dependent, with the increase of μ_O, the most stable structure is structure **f**, **g** and **j** by sequence; and (iv) the Si-dimer position are easier to be attacked by O for structure **f** compared to **h**. Structure **g**, the Si-dimer-oxidized variant of structure **f**, is more stable than **f** in most region of μ_O; while structure **h** and

its Si-dimer-oxidized variant **i** has almost the same average formation energy in the allowed O chemical potential region. The formation energies of the various interfaces at their respective most favored growth conditions (the limiting cases of metallic zirconium for metal-rich interfaces and molecular oxygen for oxygen-rich interfaces) are also shown in Table.3.3 (on page 86), which are comparable to the results obtained by Fiorentini and Gulleri[22] using the Si-epi structure ZrO_2 bulk to build the interfaces.

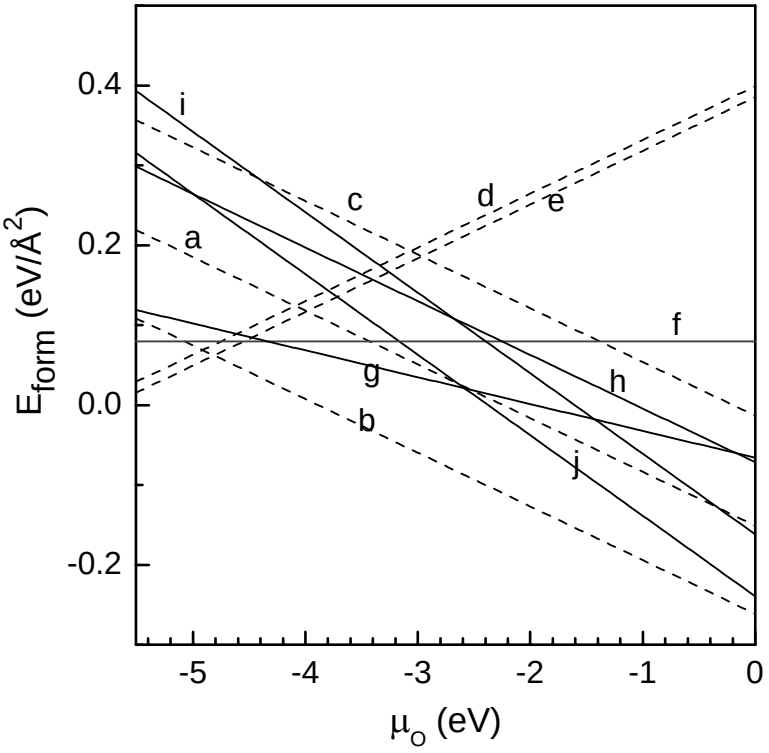

Fig. 3.10 Interface formation energies (E_{form}) of the various structures as a function of oxygen chemical potential (μ_O).

From the above analysis, we can determine the equilibrium composition and geometry of an interface structure in contact with a given chemical environment (O chemical potential) from the thermodynamics point of view, which provides the possibility of the atomic-scale control of the interface structure by altering the

chemical environment. However, we should caution that the above discussion is based only on thermodynamic arguments. The real situation in epitaxial thin film growth is more complicated where kinetic effects also play an important role. Nevertheless our calculated interface formation energy dependence on O chemical potential does offer the possibility of the atomic-scale control of the interface structure.

3.3.3 Band offsets for epitaxial ZrO_2/Si interfaces

The relaxed interface supercells were used to calculate the total density of states (DOS) and the projected density of states (PDOS) on different atoms. Due to the large size of our supercells, a non-selfconsistent calculation of DOS with much denser k-meshes follows a self-consistent total energy calculation with fewer k-points. Fig. 3.11 shows the total DOS and PDOS on different atoms residing in different layers for structure **a**. It is clear that the PDOS for atoms residing in the middle layers converge to their respective bulk characters. From the site-projected DOS for the interface Si and Zr atoms for structure **a** shown in Fig. 3.11, the absence of the interface induced mid-gap state demonstrates semiconductor character of the interface structure. Similar total DOS and PDOS have also been obtained for structures **b**, **g**, **h**, **i** and **j**, which all show semiconductor character. For structure **c**, because of the adjacent Zr and Si atoms, there are interface states in the middle of Si band gap (not shown here). Subsequent energetic calculations show that this structure is unstable, and we will not discuss it in detail.

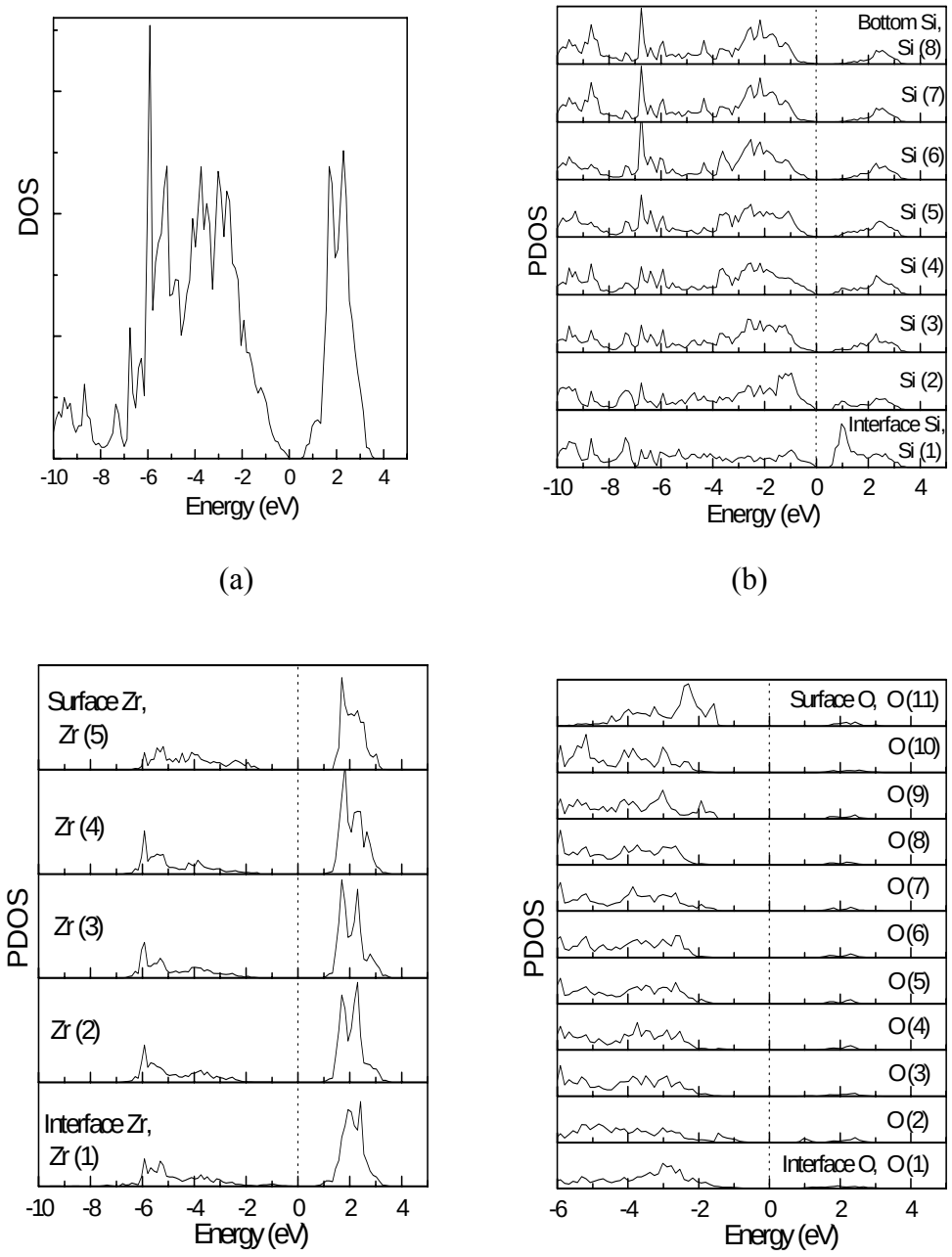

Fig. 3.11 Total DOS (a) and PDOS of Si (b), Zr (c) and O(d) for structure **a**. The energy of the valance band maximum is set to zero.

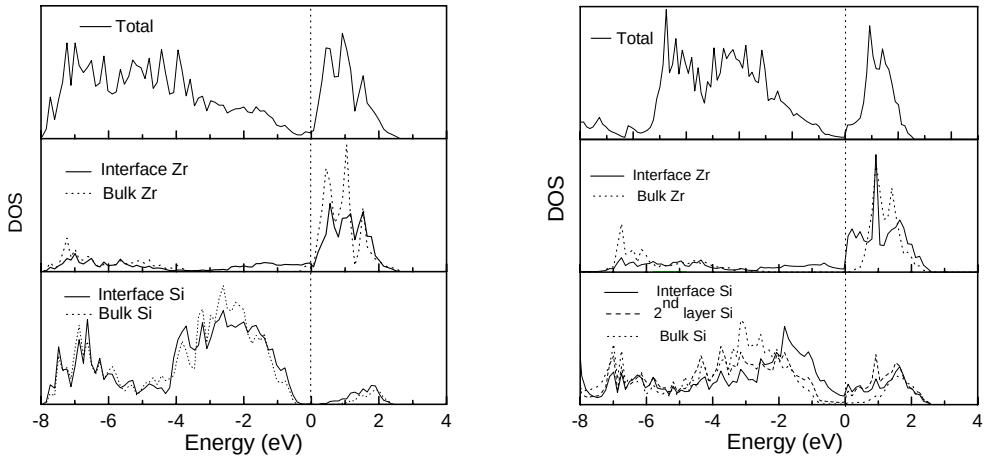

Fig. 3.12 Total DOS and PDOS for structure **d** (a) and **e** (b). The zero energy is at the Fermi level.

Structures **d** and **e** have silicide-like bonds, and should be metallic although they satisfy the general bonding rules. This was confirmed by the calculated DOS and PDOS shown in Fig. 3.12. There is no band gap for these two structures. For both structures, the PDOS for the interface Zr atoms are metal-like. For **d**, the tetrahedral bonds are satisfied for interface Si atoms, so the interfacial Si DBs are nearly occupied, while for **e**, the interfacial Si DBs are partially occupied. Our result for structure **d** is different from that of Robertson and Peacock[10], where an insulating interface with states in the middle gap has been found for structure **d**. Such a difference may come from the different Zr-Si bond length and angles in the interface when the interface supercell relaxed using different strain modes. Our results indicate that the general bonding rules are not applicable for silicide-like Zr-Si interface bonds. That means termination of Si DBs with excess Zr cannot give an insulating interface. The entire family of O-terminated interface structures, both on unreconstructed Si and 2×1 reconstructed Si templates, satisfy the bonding rules, and yield insulating interfaces.

This is not surprising since the general bonding rules, or electron counting arguments, are based on valence requirements, and the metal bonds in the interface do not obey such rules.

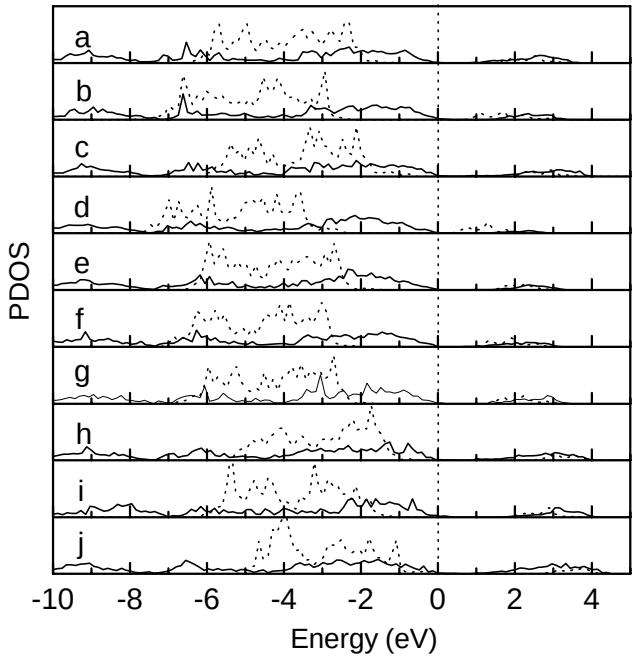

Fig. 3.13 PDOS of bulk-Si and bulk-O atoms for the various structures (Solid lines: Si; Dotted lines: O). The zero energies are aligned at the Si VBMs.

The PDOS of the O and Si atoms residing in the middle layer of the respective material (referred to as bulk-O and bulk-Si respectively) in various structures are shown in Fig. 3.13. The valence band maxima (VBM) of Si PDOS have been aligned at energy zero. We can see a rigid shift of the relative energy position of O and Si, as shown in Fig. 3.13. This shift is due to the change of the net interface dipole. In fact, such PDOS has been used to calculate the valence band offsets directly, a direct density of states analysis technique[9]. Because of the semi-quantitative character of PDOS (nonperfect determination of the VBM from PDOS), we prefer the standard

"bulk-plus-lineup"[49, 50] procedures to calculate VBO. Nevertheless, such a rigid shift in PDOS indicates variation of valence band offsets between different interface structures.

For high-*k* applications, the conduction band offset between the high-k dielectric material and Si should be large enough (>1.0 eV) to give an accessible low leakage current. Given the experimental band gap difference ΔE_g for dielectric material and Si, the relation between conduction band offset (CBO) and valence band offset (VBO) can be expressed by

$$CBO + VBO = \Delta E_g \tag{3.10}$$

Because of the band gap error in GGA, we will focus on the DFT calculation of VBO and the CBO then can be found using formula (3.10) with ΔE_g of 4.7 eV (1.1 eV for Si and 5.8 eV for ZrO_2). Based on our calculation, in-plane tensile strain has the tendency to decrease the band gap value of *t*-ZrO_2. However, there are no experimental results for the band gap of strained *t*-ZrO_2.

The interface valence band offsets are evaluated by using the standard "bulk-plus-lineup"[49, 50] procedure, where the valence band offset (VBO) is usually split into two terms:

$$VBO = \Delta E_V + \Delta V \tag{3.11}$$

The first term is referred as the band-structure term. It is defined as the energy difference of the valence band edges as obtained from two independent bulk calculations. The quasiparticle corrections to the bulk valence-band edges at the GW level are essential because the corrections are substantial for oxides and cannot counteract between Si and oxides.[51, 52, 53] Same as in Ref. 24, we apply an overall correction of 1.08 eV to all the Si-ZrO_2 interface structures, with -0.15 eV for Si[33] and 1.23 eV for ZrO_2[35]. This correction to the DFT-GGA band offset is necessary in order

to compare the calculated values with experimental results. The second term in Eq. (3.11) is the lineup of the average of the electrostatic potential through the interface, which can be obtained using the double-macroscopic average technique.[54] As such macroscopic quantity summarizes all the intrinsic interface effects,[55] the change of the chemical composition in the interface (interface structures) can modify this term; we will discuss this in detail in section VII B. The only assumption used in this "bulk-plus-lineup" procedure is that for one specified constituent such as Si or ZrO_2, the energy difference between the VBM and macroscopic electrostatic potential is kept constant in bulk and interface. This assumption has been validated by XPS measurement for $SrTiO_3$ on Si heterostructure[56], where the core levels (which are very like electrostatic potential here in spirit.) are used to lineup the band structures. The band bending at the interface is negligible, because its length scale, in the order of Debye length, can be as long as several thousands angstroms in low doped semiconductor.

In band-offset engineering (modifying the band discontinuity at semiconductor heterojunctions), the structural (i.e., of uniaxial deformation and/or lattice distortions.) and chemical effects (i.e., of different interface chemical compositions) have been studied for isovalent and heterovalent lattice-mismatched interfaces[26, 35]. As for the structural effects, few works have been done for the crystalline metal oxide on Si structures, while lattice mismatch is the case for most crystalline metal oxide on Si structures. The lattice mismatch between *t*-ZrO_2 and Si is as high as 5%. As for the chemical effects, the band offsets can be engineered by controlling the interface chemical structures, as proved recently in epitaxial-$SrTiO_3$/Si interfaces[11]. But for the epitaxial-ZrO_2/Si interfaces, detailed study is needed.

a). Strain mode effects on band offsets

To study the structural effects on band offsets, we used two modes, free-standing mode and Si-substrate mode, to relax the interface supercell structures. Here we used 1×1 supercell geometry, with 9 layers of Si, 5 layers of *t*-ZrO_2 and no vacuum. In the free-standing mode calculation, all the three lattice parameters and atom positions are allowed to relax to minimize the DFT total energy. In this way, both ZrO_2 and Si are strained with ZrO_2 being compressed and Si elongated in the direction perpendicular to the interface. This is similar to the structure of a superlattice consisting of alternating thin Si and ZrO_2 layers. For the Si-substrate mode, the lateral lattice parameter is set to the theoretical value of bulk Si ($a_{Si}/\sqrt{2} = 3.858\,\text{Å}$). The pre-strained *t*-$ZrO_2$ was used as the building block. Internal coordinations and vertical cell size are optimized to get the ground state. This mimics the situation of epitaxial growth of ZrO_2 thin film on thick Si substrate, where the strain only resides in ZrO_2 thin film. To demonstrate the strain mode effects on band offsets, structure **a** and **e** are relaxed in two modes separately.

Table 3.1 Values of parallel, perpendicular lattice parameters and Ev for Si and *t*-ZrO_2 under different strain conditions. (For an easier comparison, Si lattice parameters are given in the notation of *t*-ZrO_2 structure.)

System	$a_{//}$ (Å)	$a_{\perp}$ (Å)	E_V (eV)
Si	3.858	5.456	4.83
	3.659	5.656	5.75
	3.674	5.640	5.67
t-ZrO_2	3.650	5.289	1.70
	3.858	5.200	1.58
	3.659	5.284	1.69
	3.674	5.276	1.66

Table 3.1 shows the values of E_V, the energies for the highest occupied VBM states measured relative to the respective average of electrostatic potential, for ZrO_2 and Si bulk under different strain conditions. We note that the uniaxial strain along [001] raises the value of Ev of Si dramatically (~0.9 eV) but the in-plane tensile strain only changes the value of Ev of *t*-ZrO_2 slightly (~0.1 eV), which reflects the insensitivity of the HOMO nonbonded oxygen *p* states. Since the VBO components from the ZrO_2 bulk change little with the strain states of ZrO_2, it is likely that a loss of pseudomorphicity of the oxide film does not change too much the VBO, whereas the stain state in the Si side contributes to most of the changes in VBO.

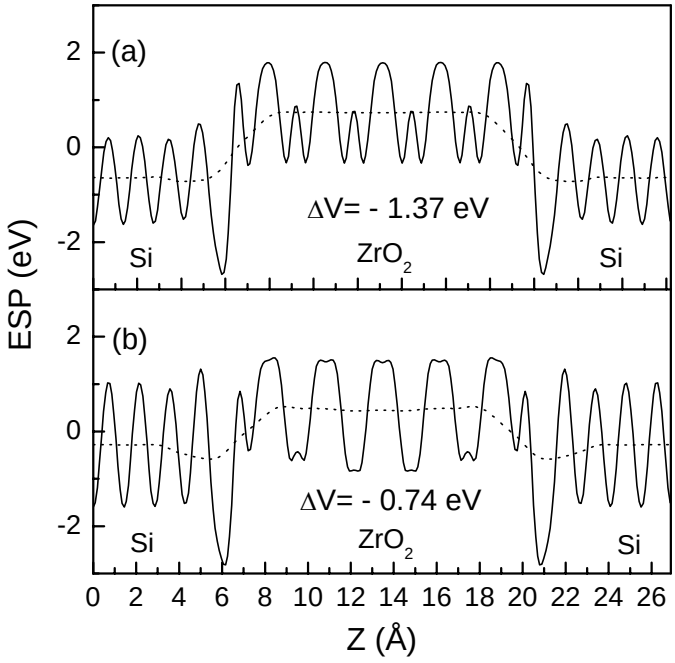

Fig. 3.14 Planar (solid line) and macroscopic average (dotted line) of electrostatic potentials (ESP) for structure **a** in Si-substrate mode (a) and free-standing mode (b), respectively. ΔV is the lineup.

Figure 3.14 shows the planar and double macroscopic average of the electrostatic potential (ESP) for structure **a** in free-standing mode and Si-substrate mode

respectively. The lineup ΔV is the difference between the double macroscopic averaged potentials residing in Si and ZrO_2 bulk-like-regions respectively. The values of ΔE_V, ΔV and VBO (with and without GW correction) are summarized in Tabel 3. 2. for structures **a** and **e** under the two strain modes.

Table 3.2 Valence band offsets (VBO) for structure **a** and **e** in two strain modes: Si-substrate (SS) and Free-standing (FS) modes.

Structure	**a**-SS	**e**-SS	**a**-FS	**e**-FS
$a_{//}$ (Å)	3.858	3.858	3.659	3.674
ΔE_V (eV)	3.25	3.25	4.06	4.01
ΔV (eV)	-1.37	-0.93	-0.74	-0.92
VBO (eV)	1.88	2.32	3.32	3.05
+GW (eV)	2.96	3.40	4.40	4.13

The main conclusions that can be drawn from Table 3.2 are: (i) the band structure term ΔE_V has a noticeable variation under different strain modes, which is mainly due to the dramatic raise of Ev of strained-Si; (ii) the strain mode effect on potential lineup is interface-structure dependent which is supposed to be related to the change of net dipole at the interface; (iii) for a given interface structure, the variation of the VBO with the strain modes are substantial; and (iv) with GW corrections, the VBOs from Si-substrate mode is closer to the experimental value (3.0~3.6eV), which is reasonable because Si-substrate mode is the situation for experimental thin film growth [7, 15, 16]. By comparison, our VBOs without GW corrections for the free-standing mode are slightly higher than but close to the values reported by Robertson and Peacock[10], who used a direct PDOS analysis technique. From the above analysis, we can see that it is not appropriate to compare the band offsets obtained from the free standing mode with the experiment results as the X-ray photoelectron measurements for valence band offsets were made on high-k dielectric thin films grown on unstrained Si substrate. In section

b), band offsets for various interface structures in Si-substrate mode were calculated and compared to the experimental values.

b). Interface structure effects on band offsets

As mentioned earlier, the interface structure or interface chemical composition can modify the lineup of VBO, which has been demonstrated in many semiconductor heterostructures [28]. To obtain the potential lineup for the different interface morphologies described in section II, we performed calculations using the repeated slab supercell. All supercell structures are relaxed in Si-substrate mode mentioned above. The planar average and double macroscopic average of the electrostatic potential (ESP) for structure **a** with repeated slab supercell is as shown in Fig. 3.15.

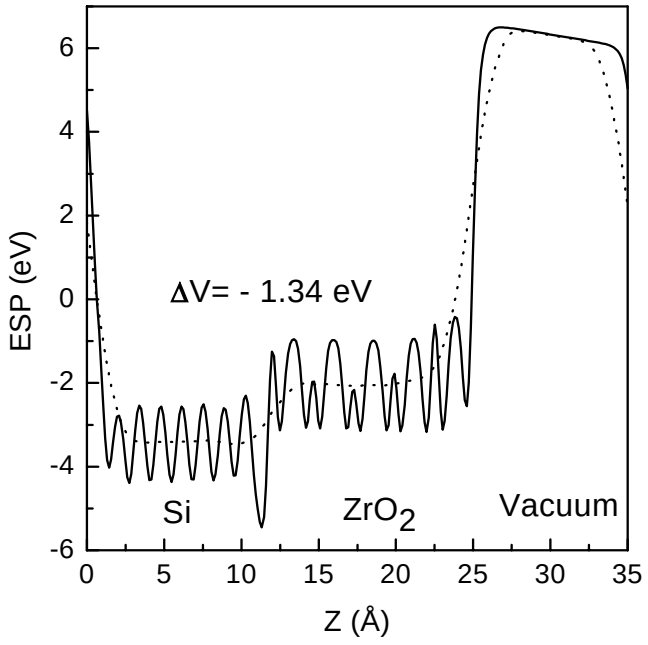

Fig. 3.15 Planar (solid line) and macroscopic average (dotted line) of electrostatic potentials (ESP) for structure **a** in repeated slab supercell. ΔV stands for the lineup.

The calculated values of ΔV are summarized in Table 3.3 for all the ten interface structures. From the virtual gap state (VGS) model (in this model, the VBO is interface structure independent.), Robertson[57] obtained the VBO for ZrO_2/Si heterostructures of 3.1 eV. Such VGS value plus the contribution from the interface net dipole gives the VBO in real situation. Our calculated VBOs is higher (lower) than such VGS value (3.1eV) as the positive (negative) interface dipole effects have been included automatically in the "bulk-plus-lineup" procedure. Puthenkovilakam *et al.* [30] obtained the VBO of 3.89 eV for structure **f**, in reasonable agreement with our result of 3.74 eV.

Table 3.3 Interface formation energies (E_{form}) and valence band offsets (VBO) for the various structures. E_{form} are for the structures at their respective most favored growth conditions (the limiting cases of metallic zirconium for metal-rich interfaces and molecular oxygen for oxygen-rich interfaces). The relative stable structures are highlighted with bold characters. All GW corrections are included for the VBO.

Structure	ΔEv (eV)	ΔV (eV)	VBO (eV)	E_{form} (eV/Å^2)
a	3.25	-1.34	**2.99**	**-0.15**
b	3.25	-0.29	**4.04**	**-0.26**
c	3.25	-1.79	2.54	-0.01
d	3.25	-0.31	4.02	0.03
e	3.25	-1.01	3.32	0.02
f	3.25	-0.59	3.74	0.08
g	3.25	-0.92	**3.41**	**-0.06**
h	3.25	-2.48	**1.85**	**-0.07**
i	3.25	-1.80	**2.53**	**-0.16**
j	3.25	-2.80	**1.53**	**-0.24**

It is clear from Table 3.3 that the valence band offset is strongly dependent on the interface structure or the interface chemical composition strongly modifies the line up term of VBO, as the case in CaF_2/Si heterostructures[58].The variation of the band offset between different structures is supposedly due to the change of interface net dipole. As shown in Fig. 5, the change of the interface dipole forces a rigid shift of the energy

position of the materials on both sides of the interface. In Table 3.3, the relative stable structures have been highlighted with bold characters. Even for these structures, the difference is as large as 2.5 eV. Such large variations with interface structures bring some technological difficulties, that is, the chemical environment should be well controlled to achieve reproducible band offset. Such a conclusion drawn from the model interfaces relaxed in the Si-substrate mode is different from that in the free-standing mode, where a relatively constant band offset has been found for O-terminated models[10]. As we have shown, such differences can be due to two effects: the structural (uniaxial deformation) and chemical (interface chemical composition) effects. The former affects both the bulk and lineup terms of band offsets, while the latter only affects the lineup term. Our results can offer some explanation for the different experimental results which vary from 3.0 eV to 3.6 eV. This difference may be due to different interface structures. However, it is difficult to make quantitative comparison directly because the samples used in the experiments are inhomogeneous and far from perfect epitaxial crystal ZrO_2 on Si structure.

2.4 Chapter Summary

In this chapter, epitaxial ZrO_2 on silicon structures have been studied as alternative gate dielectric, including film growth, interface characterization, and electronic structure calculations. Using a combinational characterization tools, including high-resolution transmission electron microscopy (HRTEM), and X-ray photoelectron spectroscopy (XPS), in conjunction with first-principles calculations based on the density functional theory (DFT), the interfacial atomic structure and band discontinuity at the ZrO_2/Si interfaces were studied. The epitaxial ZrO_2 thin films grown by pulsed laser depositions have high-quality microstructures. The HRTEM images show that the

crystalline interface has a high symmetry cube-on-cube epitaxial structure without interfacial amorphous silica or silicate layers between the metal oxide and Si substrate. Such structure could fundamentally change the scaling laws for the silicon-based transistor technology by virtue of its higher dielectric constant. The valence band offset for the epitaxial ZrO_2/Si interface was determined to be 3.04 eV by XPS. The conduction band offset is 1.67 eV, which satisfies the requirement for high-*k* applications.

Various interface structures based on the HRTEM images have been proposed. The relative stability of the various structures was compared in terms of interface formation energy, which was expressed as a function of oxygen chemical potential and calculated from the DFT total energy. The results show that Zr-terminated interfaces only exist in metal-rich atmosphere. The electronic structures of the various interfaces were also discussed to verify the general bonding rules for constructing insulating interfaces without gap states, which is a key criterion for high-*k* applications. The calculated band offsets were compared with the experimental values. The strain modes (free-standing and Si-substrate mode) effects and interface structure effects on band offsets were discussed. The band offsets are found strongly dependent on the strain modes and interface structures. The results show that in epitaxial growth of ZrO_2 on Si for gate dielectric applications, the chemical environment should be carefully controlled to get desired and reproducible band offsets.

References

[1] J. Robertson, J. Vac. Sci. Technol. B **18**, 1785 (2000).

[2] H. J. Hubbard and D. G. Schlom, J. Mater. Res. **11**, 2757 (1996).

[3] Susanne Stemmer, J. Vac. Sci. Technol. B **22(2)**, 791 (2004).

[4] M. Copel, M. Gribelyuk, and E. Gusev, Appl. Phys. Lett. **76**, 436 (2000).

[5] Y. S- Lin, R. Puthenkovilakam, J. P. Chang, C. Bouldin, I. Levin, N. V. Nguyen, J. Ehrstein, Y. Sun, P. Pianetta, T. Conard, and W. Vandervorst, J. Appl. Phys. **93**, 5945 (2003).

[6] G. D. Wilk and D. A. Muller, Appl. Phys. Lett. **83**, 3984 (2003).

[7] M. Copel, M. C. Reuter, and P. Jamison, Appl. Phys. Lett. **85**, 458 (2004).

[8] J. P. Maria, D. Wicaksana, A. Kingon, B. Busch, H. Schulte, E. Garfunkel, and T. Gustafsson, J. Appl. Phys. **90**, 3476 (2001).

[9] S. J. Wang, Y. F. Dong, A. C. H. Huan, Y.P. Feng, and C. K. Ong., Mater. Sci. Eng. **118**, 122 (2005).

[10] G. Jomard, T. Petit, A. Pasturel, L. Magaud, G. Kresse, and J. Hafner, Phys. Rev. B **59**, 4044 (1999).

[11] A. Eichler, Phys. Rev. B **64**, 174103 (2001).

[12] S. J. Wang, C. K. Ong, and S. Y. Xu, et al., Appl. Phys. Lett. **78**, 1064 (2001).

[13] G. W. Rubloff, K. Hofmann, M. Lier, and D. R. Young, Phys. Rev. Lett. **58**, 2379 (1987).

[14] W. L Scopel, Antonio J. R. da Silva, W Orellana, and A. Fazzioa, Appl. Phys. Lett. **84**, 1429 (2004).

[15] M. Copel and M. C. Reuter, Appl. Phys. Lett. **83**, 3398 (2003).

[16] E. A. Kraut, R. W. Grant, J. R. Waldrop, and S. P. Kowalczyk, Phys. Rev. Lett. **44**, 1620 (1980).

[17] E. A. Kraut, R. W. Grant, J. R. Waldrop, and S. P. Kowalczyk, Phys. Rev. B **28**, 1965 (1983).

[18] S. A. Chambers, Y. Liang, Z. Yu, R. Droopad, and J. Ramdani, J. Vac. Sci. Technol. A **19**, 934 (2001).

[19] Q. Li, S. J. Wang, K. B Li, A. C. H. Huan, J. W. Chai, J. S. Pan, and C. K. Ong, Appl. Phys. Lett. **85**, 6155 (2004).

[20] E. T. Yu, E. T. Croke, T. C. McGill, and R. H. Miles, Appl. Phys. Lett. **56**, 569 (1990).

[21] S. A. Chambers, Y. Liang, Z. Yu, R. Droopad, J. Ramdani, and K. Eisenbeiser, Appl. Phys. Lett. **77**, 1662 (2000).

[22] S. Miyazaki, J. Vac. Sci. Technol. B **19**, 2212 (2001).

[23] C. C. Fulton, G. Lucovsky, and R. J. Nemanich, Appl. Phys. Lett. **84**, 580 (2004).

[24] V. Fiorentini and G. Gulleri, Phys. Rev. Lett. **89**, 266101 (2002).

[25] X. Zhang, A. A. Demkov, Hao Li, X. Hu, and Yi Wei, Phys. Rev. B **68**, 125323 (2003).

[26] P. W. Peacock and J. Robertson, Phys. Rev. Lett. **92**, 057601 (2004).

[27] C. J. Forst, C. R. Ashman, K. Schwarz, and P. E. Blochl, Nature (London) **427**, 53 (2004).

[28] A. Fissel, J. Dabrowski, and H. J. Osten, J. Appl. Phys. **91**, 8986 (2002).

[29] P. W. Peacock and J. Robertson, Appl. Phys. Lett. **83**, 5497 (2003).

[30] R. Puthenkovilakam, E. A. Carter, and J. P. Chang, Phys. Rev. B **69**, 155329 (2004).

[31] R. Puthenkovilakam and J. P. Chang, Appl. Phys. Lett. **84**, 1353 (2004).

[32] S. Miyazaki, J. Vac. Sci. Technol. B **19**, 2212 (2001).

[33] Y. F. Dong, Y. P. Feng, S. J. Wang, and A. C. H. Huan, Phys. Rev. B **72**, 045327 (2005).

[34] G. Kresse and J. Hafner, Phys. Rev. B **47**, 558 (1993); G. Kresse and J. Hafner, Phys. Rev. B **48**, 13115 (1993).

[35] G. Kresse and J. Furthmuller, Comput. Mater. Sci. **6**, 15 (1996); G. Kresse and J. Furthmuller, Phys. Rev. B **54**, 11169 (1996).

[36] M. D. Segall, P.L. D. Lindan, M. J. Probert, C. J. Pickard, P. J. Hasnip, S. J. Clark, and M. C. Payne, J. Phys.: Condens. Matter **14**, 2717 (2002).

[37] D. Vanderbilt, Phys. Rev. B **41**, 7892 (1990).

[38] J. P. Perdew, J. A. Chevary, S. H. Vosko, K. A. Jackson, M. R. Pederson, D. J. Singh, and C. Fiolhais, Phys. Rev. B **46**, 6671 (1992).

[39] G. Jomard, T. Petit, A. Pasturel, L. Magaud, G. Kresse, and J. Hafner, Phys. Rev. B **59**, 4044 (1999).

[40] A. Christensen and E. A. Carter, Phys. Rev. B **58**, 8050 (1998); A. Christensen and E. A. Carter, Phys. Rev. B **62**, 16968 (2000).

[41] C. J. Howard, R. J. Hill, and B. E. Reichert, Acta Crystallogr., Sect. B: Struct. Sci. **44**, 116 (1988).

[42] A. Eichler, Phys. Rev. B **68**, 205408 (2003).

[43] C. J. Forst, P. E. Blochl, and K. Schwarz, Comput. Mater. Sci. **27**, 70 (2003).

[44] F. Bernadini and V. Fiorentini, Phys. Rev. B **57**, R9427 (1998).

[45] J. Padilla and D. Vanderbilt, Surf. Sci. **418**, 64 (1998).

[46] K. Reuter and M. Scheffler, Phys. Rev. B **65**, 035406 (2002).

[47] A. Eichler and G. Kresse, Phys. Rev. B **69**, 045402 (2004).

[48] G. X. Qian, R. M. Martin, and D. J. Chadi, Phys. Rev. B **38**, 7649 (1988).

[49] C. G. Van de Walle and R. M. Martin, Phys. Rev. B **34**, 5621 (1986).

[50] A. Baldereschi, S. Baroni, and R. Resta, Phys. Rev. Lett. **61**, 734 (1988); M. Peressi, N. Binggeli, and A. Baldereschi, J. Phys. D **31**, 1273 (1998).

[51] X. Zhu and S. G. Louie, Phys. Rev. B **43**, 14142 (1991).

[52] B. Kralik, E. K. Chang, and S. G. Louie, Phys. Rev. B **57**, 7027 (1998).

[53] J. Junquera, M. Zimmer, P. Ordejon, and P. Ghosez, Phys. Rev. B **67**, 155327 (2003).

[54] L. Colombo, R. Resta, and S. Baroni, Phys. Rev. B **44**, 5572 (1991).

[55] A. Franciosi and C. van de Walle, Surf. Sci. Rep. **25**, 1 (1996).

[56] S. Chambers, Y. Liang, Z. Yu, R. Droopad, J. Ramdani, and K. Eisenbeiser, Appl. Phys. Lett. **77**, 1662 (2000).

[57] J. Robertson, J. Vac. Sci. Technol. B **18**, 1785 (2000).

[58] S. Satpathy and R. M. Martin, Phys. Rev. B **39**, 8494 (1989).

Chapter 4

Metal gate/high-*k* dielectric interfaces: epitaxial Ni/ZrO_2(001) interfaces

4.1 Introduction

With the alternative high-*k* gate dielectrics being expected to replace current SiO_2 gate oxide for the continued scaling of metal-oxide-semiconductor field-effect transistors (MOSFET), there is an immense interest in replacing conventional poly-Si gate with metal gates[1, 2, 3] because of the serious problems related to poly-Si gate depletion and high gate resistance. In order to achieve low and symmetrical threshold voltages, the optimal work functions for metal gate material should be such that its Fermi level (FL) coincides with the conduction (or valence) band edge of silicon for *n*-MOSFET (or *p*-MOSFET) devices[4]. However, the possible atomic bonds of metal-metal or metal-oxygen at metal gate/oxide gate dielectric interface are quite different from conventional silicon-oxygen bond at poly-Si-SiO_2 interface. How these bonds affect the band alignment at the metal/high-*k* oxide interface is an important issue for the implementation of this gate stack. In addition, the oxygen vacancy forming during film growth or annealing is the main defect at the metal/high-*k* oxide interface. Schaeffer *et al.*[5] found that oxygen or forming gas anneal changed the effective work function of Pt-HfO_2-Si stacks. The presence of interfacial oxygen vacancies or Pt-Hf bonds was assumed to be responsible for the variation of effective work function. But

the microscopic evidence of their assumption and the physical mechanism behind the phenomena are still lacking.

In this chapter, we investigate the effects of interface atomic structures on the Schottky-barrier heights (SBH) for Ni/ZrO_2 interfaces.[6] The choice of this model structure is due to that ZrO_2 has been studied extensively[7, 8] and stands out as one of the leading contenders as alternative gate dielectric; while Ni shows the potential to be alternative gate material compatible with high-*k* oxides for advanced MOSFET applications because of its high work function and relatively high thermal stability [1, 2]. And its lattice structure could be well matched with cubic ZrO_2 by 45^o rotation along [100] direction. Therefore, the Ni/ZrO_2 (001) interface is a desirable model structure to study the interface effect on the physical properties of metal/high-κ stack. Using *ab initio* calculations, Beltran *et al.* [9] have predicted the strong chemical bonds at the Ni (001)/cubic-ZrO_2 (001) polar interfaces. However, the Schottky-barrier heights and their dependence on interface structures were not discussed.

4.2 Growth of Ni thin film on ZrO_2 (001) in UHV

The deposition of metal Ni was performed by Omicron EFM3 e-beam evaporator in the X-ray photoemission spectroscopy (XPS) preparation chamber with a base pressure of 5.0×10^{-10} mbar. The *e*-beam evaporator works with evaporating the atoms of the source rod by electron beam bombardment from a hot filament. In this experiment, Ni overlayer with thickness of ~3.0 nm was deposited from a high-purity (99.99%) wire using the e-beam evaporator onto yttrium-stabilized ZrO_2 (YSZ) substrates at a deposition rate of 1.0 Å/min. Before the deposition of metal Ni, single crystal cubic yttrium-stabilized ZrO_2 (YSZ) was pre-cleaned by dipping in Acetone and 10% nitride acid solution in sequence. Then the substrates were annealed for 5 min at 600 ºC to

remove carbon contamination in the XPS chamber with base pressure of 1.0×10^{-10} mbar. The interface reaction was monitored by *in situ* x-ray photoemission (XPS). The thin film microstructure and thickness were observed by cross section TEM.

XPS measurements were performed in a VG ESCALAB 220i-XL system using a monochromatic Al $K_{\alpha 1}$ source (1486.6 eV). The pass energy of analyzer was set to 10 eV to have high measurement accuracy. The binding energy scale was calibrated with pure gold, silver and copper by setting the Au $4f_{7/2}$, Ag $3d_{5/2}$ and Cu $2p_{3/2}$ at binding energy of 83.93 eV, 368.26 eV and 932.67 eV, respectively. The structural information at the Ni/ZrO_2(001) interface was investigated by high-resolution transmission electron microscopy (HRTEM) using a Philips CM 300. The accelerating voltage is 300 kV, which has a point-to-point spatial resolution of 1.7 Å.

4.2.1 *In situ* XPS measurements for Ni/ZrO_2(001) interfaces

After the ultra-thin (~3 nm) Ni film was deposited on YSZ (001) by e-beam evaporation in the XPS preparation chamber, the sample was transferred to the XPS analysis chamber without the breaking of ultrahigh vacuum (UHV). As the sampling depth of X-ray photoelectron with energy of 1486.6 eV can be up to 10.0 nm, the information from both the metal thin film and oxide substrate can be seen from photoemission spectra simultaneously, as shown in Fig. 4. 1.

Figure 4.2 shows the Ni 2p XPS spectra for ultrathin (~ 3 nm) Ni film grown at 300^{o}C on YSZ (001) substrate. The energy positions of Ni $2p_{3/2}$ and $2p_{1/2}$ peaks were at 853.0 and 870.3 eV respectively, which are in good agreement with that for bulk fcc-Ni and reveal the 3-D and metallic feature of Ni crystallites. In addition, there is a well resolved satellite (as denoted by the arrow in Fig.4.2) at 859.0 eV, which is the

characteristic of metallic Ni. This so called "6-eV satellite" is a result of photoelectron final state effects.

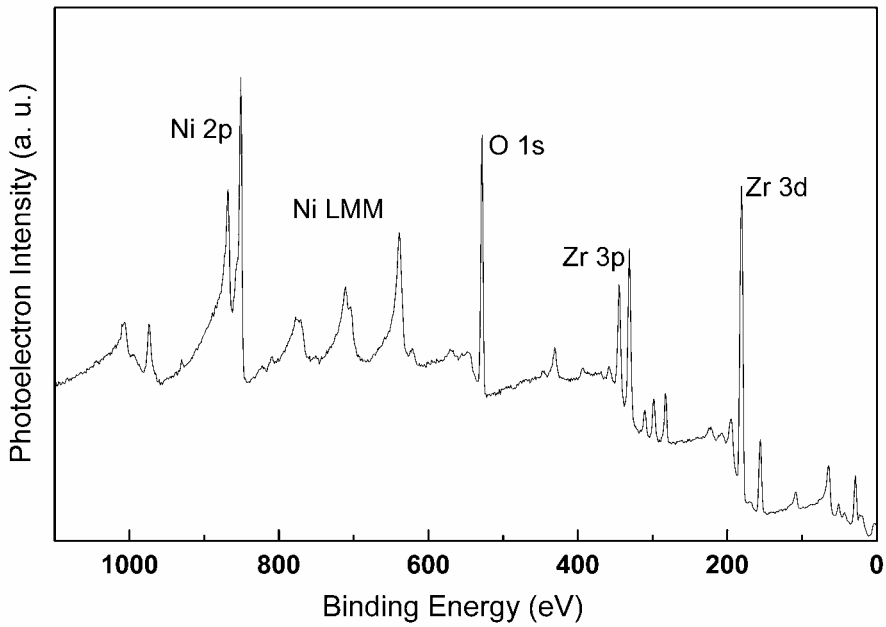

Fig. 4.1 XPS survey spectra for 3.0 nm Ni/YSZ(001) interface.

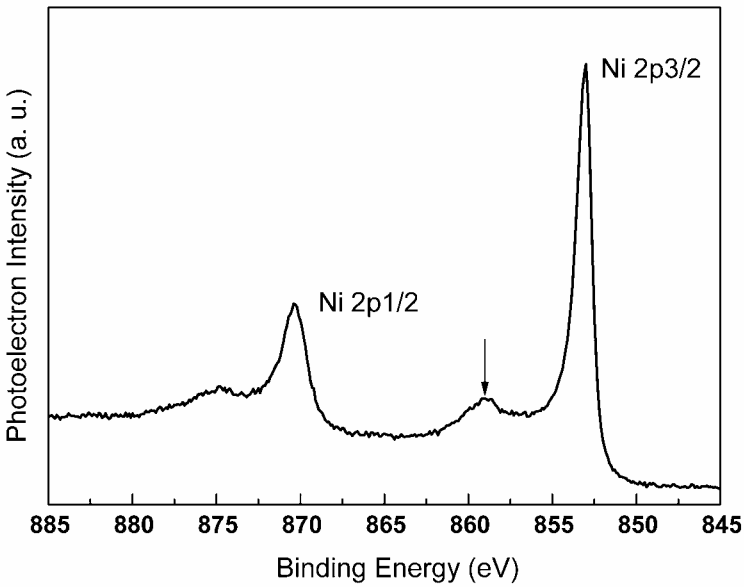

Fig. 4.2 Ni 2p XPS spectra for 3.0 nm Ni/YSZ(001) interface

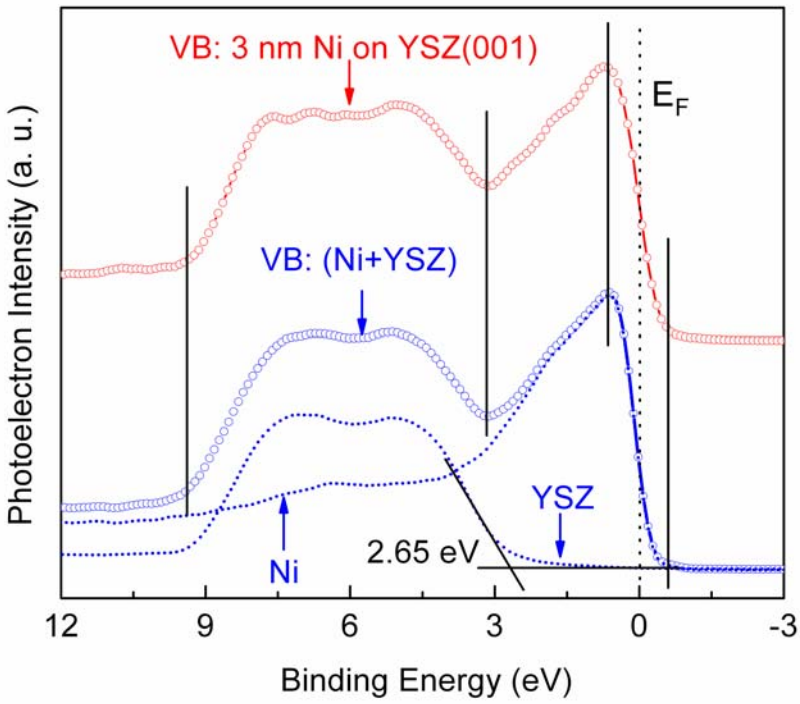

Fig. 4.3 Comparison of the actual XPS valence band spectra for the 3.0 nm Ni/YSZ(001) interface and the simulated one (Ni+YSZ).

The metallic characters of the ultrathin Ni film were also demonstrated by the valence band (VB) spectra of the sample, as show in Fig. 4.3. The valence band spectra for the 3.0 nm Ni/YSZ(001) interface are metallic with a sharp cutoff at the Fermi level (zero energy position as denoted by the dotted line in Fig. 4.3). The high density of states near the Fermi level originates from the localized Ni d valence electrons, which buries the valence band edge of YSZ(001) substrate. Summing the appropriately shifted and weighted VB spectra of pure YSZ (001) substrate and bulk-Ni, we simulated the valence band spectra for Ni/YSZ interface, as shown in Fig. 4.3. Agreement between the actual VB spectra and the simulated one for Ni/ZrO_2 interface is rather good with regard to the positions and relative intensities of all features. Further more, the *p*-type Schottky barrier height, defined as the energy difference between the metal Fermi level and the VB edge of ZrO_2, was measured readily to be 2.65 ± 0.05 eV from Fig. 4.3 with the VB edge determined accurately by the linear method. [10]

4.2.2 *Ex situ* HRTEM for Ni/ZrO_2 interfaces

Transmission electron microscopy (TEM) and, in particular, high resolution transmission electron microscopy (HRTEM), is one of the most useful techniques for studying the atomistic structures of the interface. TEM techniques have been successfully applied to various metal/ceramic and ceramic/ceramic interfaces.[11] For the present case, Ni/ZrO_2 interface, there is a challenge due to the small lattice constant (0.35 nm) of Ni, which results in very small inter-plane distances, 0.17 nm in the <001> direction, 0.12 nm in the <011> direction, and 0.20 nm in the <111> direction. These small inter-plane distances are around or even below the resolution of our state-of-the-art HRTEM. So it is very difficult to discern the single Ni atoms even in

HRTEM images. However, it is expected that growth orientation of Ni on ZrO_2 can be decided from the HRTEM images. Because of the small lattice mismatch (~2%) between Ni and ZrO_2 and the strong bonding strength at Ni(001)/ZrO_2(001) interfaces, epitaxial growth of Ni on ZrO_2(001) surface is quite possible under certain growth conditions (*e.g.*, thermodynamic dominated situations with relative high growth temperature and very low growth rate). In this section, we will investigate the effect of growth conditions on the structure of Ni/ZrO_2(001) interfaces by *ex-situ* HRTEM.

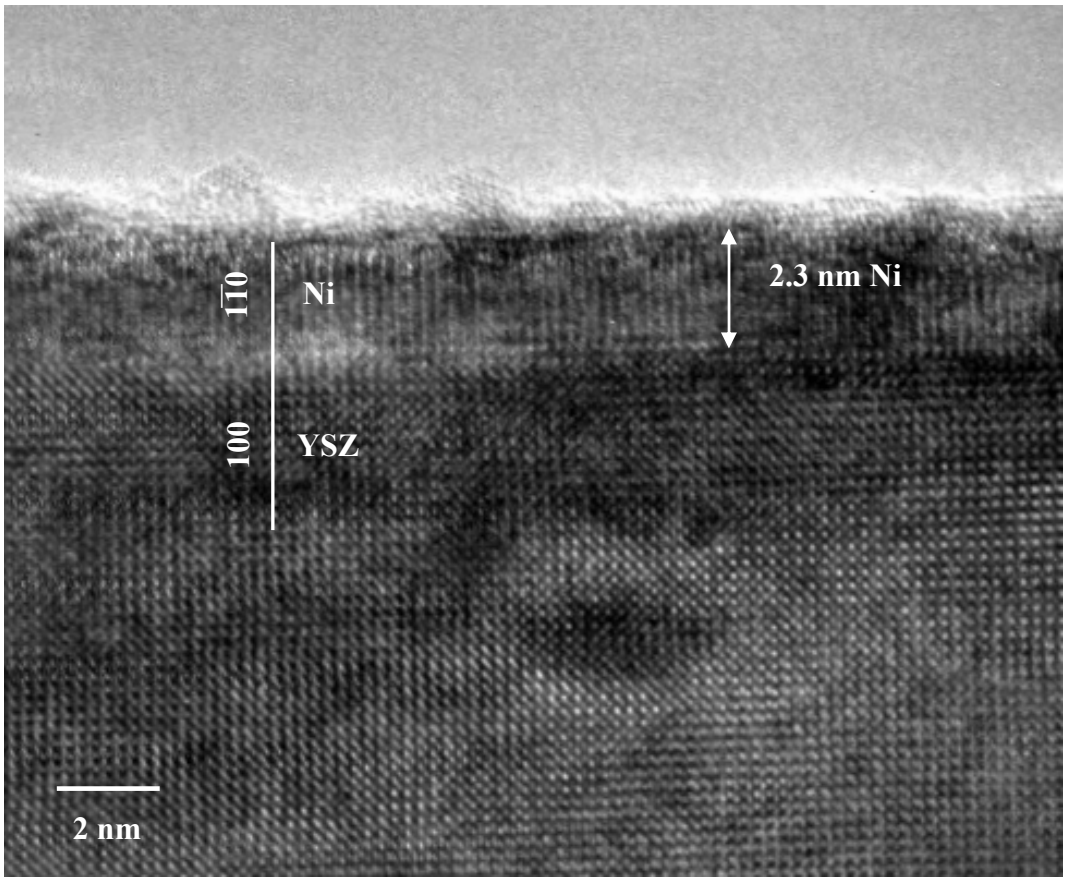

Fig. 4.4 Cross sectional HRTEM micrograph of the epitaxial Ni/YSZ(001) interface with the incident electron beam parallel to $[010]_{YSZ}//[110]_{Ni}$.

Ultra-thin (~2.3 nm) Ni film was deposited on YSZ (001) surface at 300^0 C by e-beam evaporation in the XPS preparation chamber with a base pressure of 5.0×10^{-10} mbar. The deposition rate was very low, around 6 nm/hour or 1.0 Å/min. The relative high deposition temperature and very small deposition rate guarantee that thermodynamic parameters dominate the growth of thin film, where adatoms have enough time and activation energy to move to the most energy-favorable positions at the initial growth stage. We note here that higher deposition temperature is unfavorable because of the high oxygen ion mobility in YSZ at elevated temperature. Our XPS experiments have demonstrated that ultrathin Ni overlayer was partially oxidized when Ni was deposited on YSZ(001) surface at temperature higher than 400^0C.

Figure 4.4 shows the cross sectional HRTEM image for the Ni thin film grown at 300^0C on YSZ(001) substrate. It is clear that epitaxial Ni ultra-thin film on YSZ(001) has been obtained with the epitaxial relationship as $[010]_{YSZ}$// $[110]_{Ni}$ and $(001)_{Ni}$//$(001)_{YSZ}$. The interface between nickel and YSZ is rather sharp with only a few steps, which is due to the flat surface of YSZ(001) after high-temperature (upper to 600^0C) annealing. In addition, few misfit dislocations with Burgers vector parallel to the interface can be observed between $(100)_{YSZ}$ and $(1\bar{1}0)_{Ni}$ planes. That is to say, the $(100)_{YSZ}$ planes almost coincide with the $(1\bar{1}0)_{Ni}$ planes, which is due to the small lattice mismatch between Ni and YSZ after the 45^0 rotation of Ni in (001) plane ($(\sqrt{2}a_{Ni}-a_{YSZ})/a_{YSZ}=2\%$). Notice that all $(100)_{YSZ}$ planes are clearly seen in the cross sectional HRTEM image; while only half of the $(1\bar{1}0)_{Ni}$ planes are visible because of the small inter-plane distance (0.12 nm) for $(1\bar{1}0)_{Ni}$ planes.

From the above analysis for the cross sectional HRTEM micrograph, one can see that epitaxial structure was obtained for Ni/YSZ(001) interface under relative high

growth temperature (300^0 C) and very low growth rate (~6 nm/hour). However, the most abundant surface for fcc-metal is (111), which is more stable than (001) surface. Therefore, without the strong perturbation of substrate, Ni overlayer tends to grow along [111] direction. However, the interaction between the substrate and the adatoms makes the initial growth of Ni on YSZ (001) rather complex. On one hand, the epitaxial growth along <001> direction would give a strong interface formation energy because of the strong interface bonding. On the other hand, Ni itself tends to growth along the [111] direction because of the smaller surface energy. The above competition between the interface and surface energy is only based on a thermodynamic consideration. In real thin film growth, kinetics also plays important role. We will show how the Ni thin film on YSZ (001) interface structure can be changed by controlling the growth conditions.

This time, the deposition of the Ni metal overlayer was performed at room temperature in a multiple-chamber ultrahigh-vacuum (UHV) sputtering system with a base pressure of 5.0×10^{-10} mbar. The deposition rate, ~2 nm/min, was fast compared to the above growth at 300^0 C. Then the as-grown Ni/YSZ interface was annealed at 300^0 C for 2 hours in UHV environments.

Figure 4.5 shows the cross sectional HRTEM image for the Ni thin film on YSZ(001) substrate after annealing. As shown in the HRTEM image, the annealed Ni thin film has high quality with a [111] growth orientation instead of the epitaxial growth for the former sample. This can be seen clearly from the amplified interface as shown in the inset in Fig. 4.5, where the (111) planes parallel to the interface on the Ni side has an inter-plane distance of ~2.0 Å. However, the Ni atoms at the interface region (about two layers in thickness or 4 Å) lack the clear orientation. This is because the surface unit cell for YSZ(001) does not match with that for Ni (111) surface and

one thin layer of interface layer was necessary for the transformation from the square unit cell [YSZ(001)] to the hexagonal one [Ni(111)].

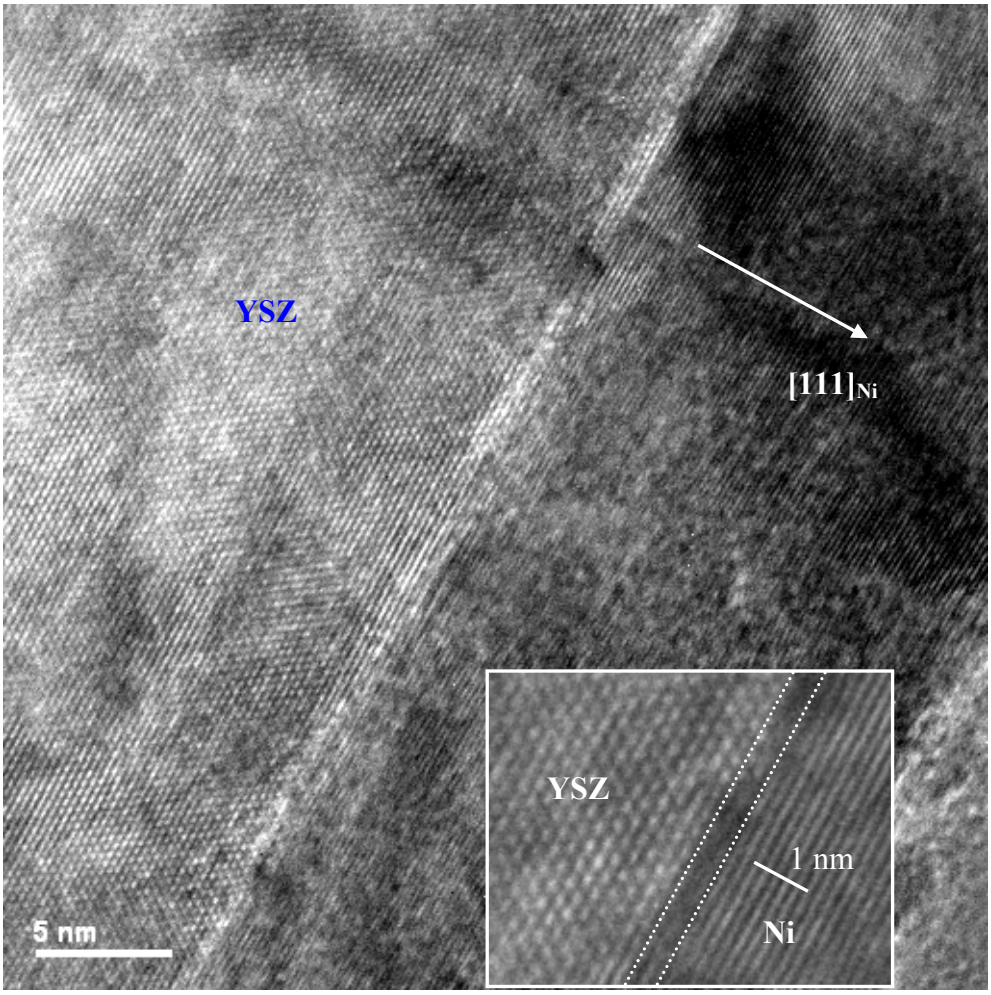

Fig. 4.5 Cross-sectional HRTEM micrograph of the Ni/YSZ(001) with the incident electron beam parallel to $[110]_{YSZ}$. The inset shows one amplified interface region.

4. 3 Impact of interface structure on Schottky-barrier height

4.3.1 SBHs for different Ni/ZrO_2(001) interfaces

To investigate the impact of interface structure on Schottky-barrier height (SBH), we fabricated two kinds of YSZ (001) surfaces: one is the ideal YSZ(001) surface terminated by a layer of oxygen ions at atmosphere oxygen pressure and room

temperature; the other was intentionally sputtered by Ar^+ ion at the energy of 1 KeV for 2 min to obtain defect–rich or Zr-terminated surface. The former was annealed for 5 min at 600 ºC to remove carbon contamination in the XPS chamber with base pressure of 1.0×10^{-10} mbar; while the latter was sputtered by Ar^+ ion after the 600 ºC anneal. We note that under the UHV condition, where oxygen partial pressure is very low, there would be some oxygen vacancies on the ideal YSZ(001) surface according to the surface structure dependence on the oxygen chemical potential.[12] But the density of surface oxygen vacancies for the ideal surface is much smaller than that for the sputtered surface. Then the metal Ni was deposited at room temperature on the two kinds of YSZ(001) surfaces by e-beam evaporator at a deposition rate of 1.0 Å/min in the X-ray photoemission spectroscopy (XPS) preparation chamber with a base pressure of 5.0×10^{-10} mbar. The growth rate of Ni film was measured by *ex situ* TEM.

The *x*-ray photoemission method used to determine the band alignment of heterostructure is based on the assumption that the energy difference between the valence-band edge and the core-level peak for substrate is constant with/without the deposition of overlayer.[13] This method has been widely used to determine the band discontinuities at the interfaces of metal/semiconductor, insulator/semiconductor, and semiconductor/semiconductor.[14, 15, 16] Here, for the case of Ni film on ZrO_2 substrate, the valence-band and Zr 3d core-level spectra from substrate can be used as reference to determine the value of Schottky-barrier height at the Ni/ZrO_2 interface.

Figure 4.6 (a) shows the valence-band spectra for pure YSZ and Ar^+-sputtered YSZ (S-YSZ). There was a small bump at the binding energy of zero (Fermi energy) for S-YSZ spectra, which indicates that after sputtering with Ar^+ ions, the ZrO_2 surface was defect-rich with the generation of O vacancies or the exposure of Zr ions. This implies that the ZrO_2 surface becomes metallic after sputtering. Except for the small bump, the

valence-band spectra for these two samples (YSZ and S-YSZ) were almost the same, which suggests that the defects due to sputtering are only at the near-surface region (within several angstroms). The leading edges of the valence bands were determined by the intersection of the regression-determined line segments defining the edge and the flat energy distribution curve in the energy band gap region as shown in Fig. 4.6 (a). The energy positions of valence band edges were the same (2.6 eV) for the two samples, which confirmed that the defects were localized at the surface.

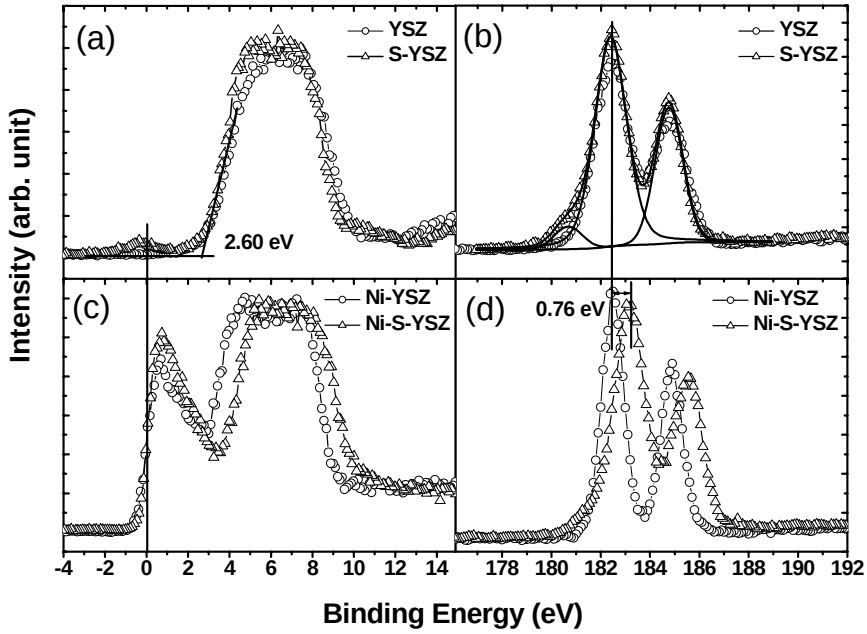

Fig. 4.6 (a) Valence-band spectra for pure YSZ and Ar^+-sputtered YSZ (S-YSZ). (b) Zr 3d core-level spectra for YSZ and S-YSZ. (c) Valence-band spectra for 25 Å Ni on pure YSZ (Ni-YSZ) and S-YSZ (Ni-S-YSZ). (d) Zr 3d core-level spectra for Ni-YSZ and Ni-S-YSZ.

The Zr 3d spectra for YSZ and S-YSZ are shown in Fig. 4.6 (b). The spin-orbital split of the Zr spin-orbital doublets (Zr $3d_{5/2}$ and Zr $3d_{3/2}$) has a value of 2.37 eV, which is in good agreement with that in the literature.[17] While for S-YSZ there was an additional small peak at the lower energy (1.76 eV lower than that of Zr $3d_{5/2}$ for pure

YSZ surface), which corresponds to the energy position of metallic or sub-oxidized Zr on the surface. Notice that the Zr 3d peak energy of Zr metal feature is about 3.0 eV lower than that of fully oxidized Zr. This indicates that the metallic character of S-YSZ surface comes from the sub-oxidized surface Zr ions. It is clear from Figs. 4.6 (a) and (b) that the energy difference between the energy position of Zr $3d_{5/2}$ peak and the leading edge of the valence bands ($\Delta E = E_{Zr-3d_{5/2}} - E_{VBM}$, 179.62 ± 0.05 eV in this case) was the same in these two samples within the measurement accuracy even though they are supposed to have totally different surfaces. This is because that ΔE can be viewed as a bulk property with no relation to the surface status or the overlayer on the ZrO_2 surface. This finding is consistent with earlier observations for another high-*k* oxide $SrTiO_3$ suggesting that the energy difference between valence band edge and shallow core level is not related to the surface structures. [18]

The Schottky-barrier height for Ni/ZrO_2 interface can be determined by measuring the energy difference between the Fermi level of the Ni/ZrO_2 stack and the leading edges of the valence bands in the bulk region of ZrO_2. Then, the *p*(*n*)-type Schottky-barrier height Φ_p (Φ_n) can be obtained using the simple equations

$$\Phi_p = (E_{Zr-3d})_{Ni/ZrO_2} - \Delta E \tag{4.1}$$

and

$$\Phi_n = E_g - \Phi_p \tag{4.2}$$

where $(E_{Zr-3d})_{Ni/ZrO_2}$ is the peak position of Zr 3d core level spectra in Ni/ZrO_2 stack, E_g the band gap of ZrO_2 (5.80 eV for the YSZ sample in our experiment), and $\Delta E = E_{Zr-3d_{5/2}} - E_{VBM}$. Eq. (4.1) expresses the conventional approach to SBH measurements by monitoring the position of substrate core level. [19] The substrate core level can also be used as the reference so that the SBH can be read directly from the

energy difference of the substrate valence band edge before metal deposition and the FL of the metal/oxide interface.

Figures 4.6 (c) and (d) show the valence-band and Zr 3d core level spectra of 25 Å Ni on YSZ and S-YSZ. The energy positions have been aligned using the Fermi level (at energy zero) of metal Ni, where the half intensity of valence edge is set to be the binding energy of zero. It can be seen that there is a 0.76 eV energy difference for the peak position of Zr 3d spectra between the two samples with different interface structure (The Ni-YSZ interface is O-rich, while the Ni-S-YSZ is O-deficient.). P-type SBHs were read in Fig. 4.6 directly to be 2.60 eV for the Ni-YSZ interface and (2.60+0.76) eV for the Ni-S-YSZ interface.

4.3.2 A modified charge neutrality level (CNL) model

The measured *p*-type SBHs for Ni/ZrO_2 interfaces are dependent on the initial structure and chemical composition of the ZrO_2 surface or interface-structure dependent. A possible explanation for this interface-structure dependent SBH at Ni/ZrO_2 interfaces is that the local interface dipole is created mainly by charge transfer between the metal and oxide. This will be discussed firstly in the framework of metal induced gap states (MIGS) model as following. Then a detailed consideration based on first-principles calculations will be given in next section.

In the conventional MIGS model for the formation of Schottky barrier height at metal/semiconductor interfaces, charge neutrality level (CNL) serves as the “Fermi level” in the semiconductor side to align the energy bands at the interface. If the energy position of CNL in the semiconductor is higher than that of Fermi level in the metal, electrons will flow from the semiconductor into the metal and *vise versa*, as shown in Fig. 4.7(a). To offer a simple scheme to predict SBH from the bulk properties

of the two components (metal and semiconductor) only, with no need for the detail interface information, one often assumes CNL as a bulk property with no relation to the surface states of the semiconductor. However, if one wants to characterize the Schottky barrier height in the framework of MIGS model only, he would better admit that CNL includes both intrinsic and extrinsic parts.[20] For Schottky barriers, the semiconductor CNL may depend on the geometry of the interface, which has been demonstrated widely in various metal/semiconductor interfaces. It was proposed to distinguish the intrinsic and extrinsic charge neutrality levels: the intrinsic one is associated with an ideal, broad and structureless, metal induced density of states while the extrinsic one depends on the specific characteristics of each interface. Obviously, intrinsic CNL only depends on the bulk properties of the semiconductor. It is associated with the branch points of the complex band structure of the semiconductor, [21, 22] and can be evaluated from the calculation of actual complex band structures.[23] The extrinsic CNL depends on the specific characteristics of each interface, and thus different surface status will strongly modify the energy position of the charge neutrality level. For narrow band gap semiconductors, such as Si and GaAs, the allowed range of modification for CNL is within several tenths eV. Superficially, the variation range of CNL for Si or GaAs is restricted by its band gap. The physical mechanism behind it is the strong MIGS screening in such narrow band gap semiconductors and intrinsic CNL dominates the formation of Schottky barrier for these semiconductors. However, for wide band gap semiconductors or insulators, the variation range of CNL modification can be as large as several eV. Without the consideration of the influence of specific interface characteristics, appropriate conclusions cannot be drawn. Metal gate/high-k dielectric interfaces belong to the latter situation.

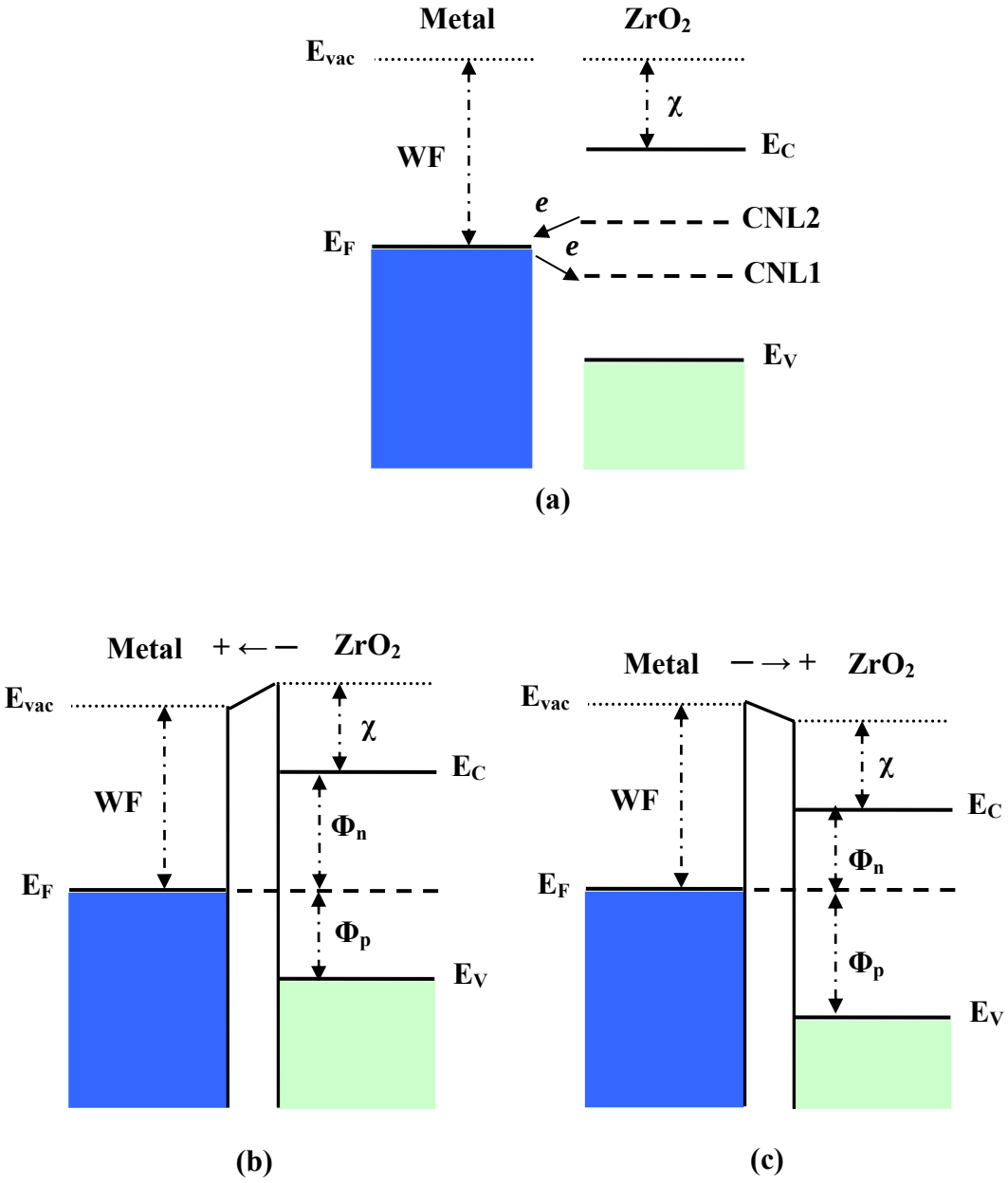

Fig. 4.7 Energy band diagram for (a) separated Ni (001) surface and ZrO_2(001) surfaces with different surface status; (b) Ni-YSZ interface (oxygen-rich); and (c) Ni-S-YSZ interface (oxygen-deficient). WF is the vacuum work function of Ni (001) with a value of 5.22 eV. χ denotes the electronegativity of ZrO_2 with an estimated value of 2.5 eV. Φ_p and Φ_n denote the *p*- and *n*-type SBH.

Figure 4.7 (a) shows the isolated energy diagrams of metal and oxide immediately before they combine to form interfaces. Figs. 4.7 (b) and (c) illustrate the different charge transfer at the two kinds of Ni/ZrO_2 interfaces, oxygen-rich (Ni-YSZ) and oxygen-deficient (Ni-S-YSZ) interfaces. Charge neutrality level (CNL), defined as the energy above which the surface states are empty for a neutral surface, serves as "Fermi level" for oxide surfaces. Generally, the energy positions of the metal Fermi level and the oxide CNL are not at the same height, which will incur charge transfer after the metal and oxide contact to form interface.

According to the above discussion, the charge neutrality level not only depends on the bulk properties of the material (intrinsic CNL) but also is strongly related to the surface status of the material (extrinsic CNL). Therefore, it is expected that the ideal YSZ(001) surface and the sputtered YSZ(001) surface have totally different energy positions of "Fermi levels" or CNL, with CNL1 for the former and CNL2 for the latter, as shown in Fig. 4.7 (a). For Ni-YSZ interface, the energy position of CNL1 is lower than that of the metal Fermi level, which leads electrons to transfer from metal side to oxide side when the two sides combine to form interface. When equilibrium is reached, the energy band diagram is shown in Fig. 4.7 (b), where an interface dipole forms and points towards the metal side. For Ni-S-YSZ interface, the charge transfer is in an inverse direction, from oxide to metal. Thus the interface dipole points towards the oxide side, as shown in Fig. 4.7 (c). It is the different interface dipole that shifts the energy bands in the two sides and induces the variation of band alignment. Notice that the above argument is only based on a phenomenal electrostatic picture. One important question remains, that is, why CNL1 for O-terminated surface lies below CNL2 for Zr-terminated surface. In next section (Sec. 4.4), our first-principles calculations would provide a microscopic explanation for such variation.

4.4 Atomistic modeling for Ni/ZrO_2(001) interfaces

4.4.1 Methods and models

The first-principles calculations were performed by using VASP[24, 25] code with Vanderbilt ultrasoft pseudopotentials[26] and the generalized gradient approximation (GGA) [27] for the exchange-correlation potential. Spin-polarization effects were included. The plane-wave basis cutoff is 350 eV.

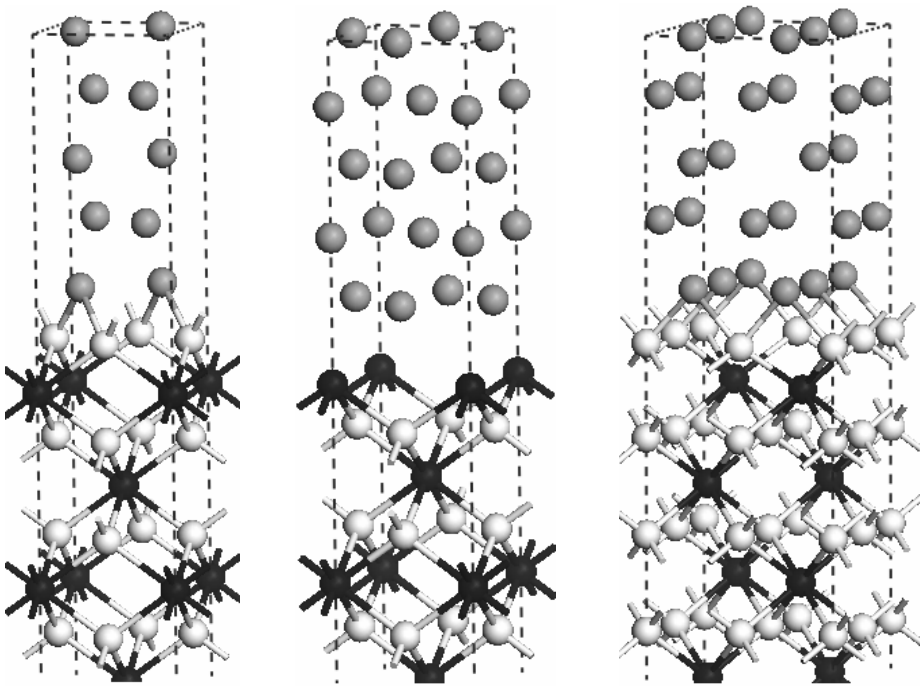

(a) (b) (c)

Fig. 4.8 Supercell structures for O-t (a), Zr-t (b) and O-v (c) interfaces， half of the supercell shown (Grey: Ni; Black: Zr; Light: O).

In order to study the interface structure dependence of SBH, we have considered three types of Ni/ZrO_2 interface: O | Ni or the ZrO_2 terminated with O atom layer (referred as O-t interface), Zr | Ni or the ZrO_2 terminated with Zr atom layer (referred as Zr-t interface), and O | Ni with O vacancy at the interface (referred as O-v interface), as shown in Fig. 4.8. In our supercell, cubic ZrO_2 (c-ZrO_2) and fcc-Ni were

stacked along [001] alternatingly with c-ZrO_2 [110] aligned with Ni [100]. We used 1×1 supercell geometry for O-t and Zr-t interface with 9 layers of Ni, 7 layers of Zr, 8/6 layers of O and no vacuum. In O-v interface, an O vacancy is introduced in the O-Ni interface by removing one out of four O atoms in the interface, which corresponds to the interface with $3.76\times10^{14}/cm^2$ oxygen vacancies. For the 1×1 interface supercells, we have used $8\times8\times1$ **k**-mesh. The lateral lattice constant was constrained to bulk c-ZrO2 ($a_{c-ZrO_2}/\sqrt{2} = 3.647$ Å). The atomic coordinates and the vertical lattice vector were then optimized to minimize the total energy. The relaxations were performed under the respective high-symmetry restriction for O-t and Zr-t interfaces. For O-v interface, atoms in ZrO_2 side were kept frozen except for the first two layers of O and Zr atoms at the interface, which prevent the cubic-to-tetragonal phase-transition in ZrO_2 side. Otherwise, the ZrO_2 bulk phase-transition will overwhelm the interface effect we should focus on.

4.4.2 Interface energetics and electronic structures

The actual interface stability of each interface is given by the interface formation energy or interface tension, namely E_{form}, defined as the Gibbs free energy normalized by the cross-sectional area.[28] Assuming that the interface is in thermodynamic equilibrium, neglecting the vibrational entropy contributions and enthalpy changes due to finite temperature, E_{form} can be directly obtained from the DFT total energy calculations:

$$E_{form} = (1/2A)[E_{ZrO_2/Ni} - (nE_{Ni} + mE_{ZrO_2} \pm l\mu_O)] \quad (4.3)$$

where $E_{ZrO_2/Ni}$ is the DFT total energy of the interface supercell, *n* and *m* are the numbers of Ni atoms and ZrO_2 bulk units in the supercell, respectively, E_{Ni} and E_{ZrO_2} the total energy per Ni and ZrO_2 bulk unit respectively, *l* is the number of oxygen atoms added (+, for O-rich situation) or removed (-, for Zr-rich) to create the interface, μ_O the chemical potential of oxygen in the interface supercell, and *A* the basal area of the interface supercell. Owing to the fact that our supercells are nonstoichiometric, the formation energy was expressed as a function of oxygen chemical potential μ_O as shown in the above formula, where μ_O is allowed to vary over the range[29]

$$\frac{1}{2}(E_{O_2} + H_f) \le \mu_O \le \frac{1}{2}E_{O_2} \tag{4.4}$$

where E_{O_2} is the DFT total energy per oxygen molecule, and H_f=—11.37 eV [9] is the formation enthalpy (by convention is negative) per formula unit for *c*-ZrO_2. The interface tension as a function of oxygen chemical potential was shown in Fig. 4.9. The left and right boundaries of Fig. 4.9 correspond to a system in thermodynamic contact with *hcp*-Zr bulk and O_2 gas respectively.[30] It can be seen that both interfaces have a comparable range of thermodynamic stability, indicating that either O-t or Zr-t interface could be formed depending on whether growth occurs in O-rich or Zr-rich conditions. Alternatively, the interface tension can be expressed as a function of Zr chemical potential as shown in Fig. 4.10, where μ_O is allowed to vary over the range:

$$E_{Zr} + H_f \le \mu_{Zr} \le E_{Zr} \tag{4.5}$$

where E_{Zr} is the DFT total energy per Zr atom in *hcp*-Zr metal. Then the left and right boundaries of Fig. 4.10 correspond to a system in thermodynamic contact with O_2 gas and *hcp*-Zr bulk respectively.

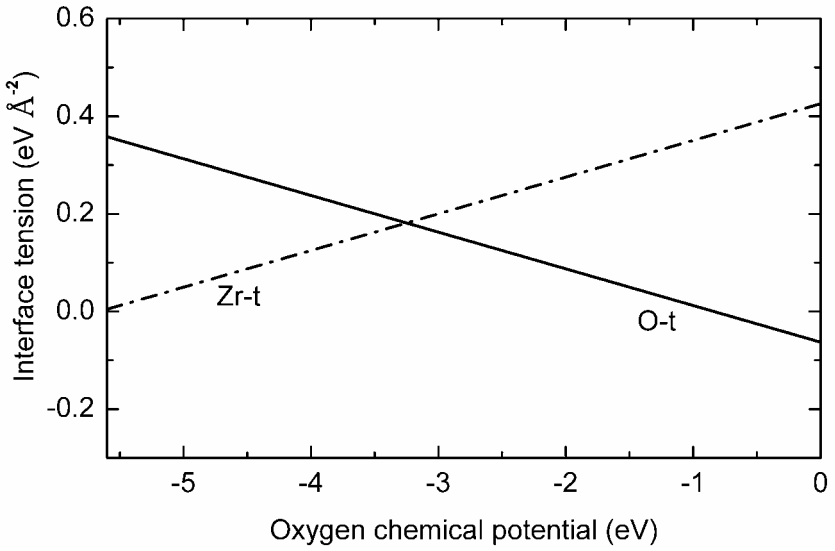

Fig. 4.9 Interface tension as a function of oxygen chemical potential for O-t (solid line) and Zr-t (dash-dotted line) interfaces.

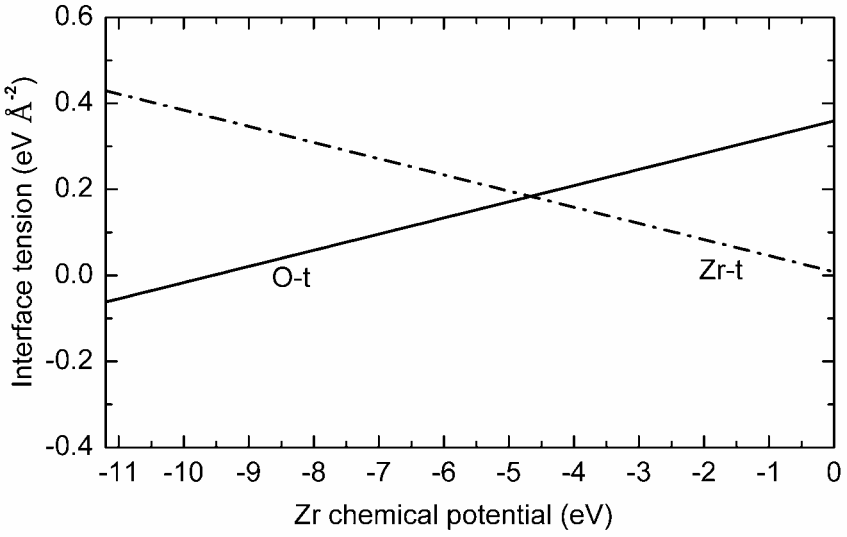

Fig. 4.10 Interface tension as a function of Zr chemical potential for O-t (solid line) and Zr-t (dash-dotted line) interfaces.

In addition to the interface tension, another important fundamental quantity which controls the mechanical strength of metal-ceramic interfaces is the work of separation (W_{sep}), the reversible work needed to separate the interface into two interfaces.[31] Although the energy needed in a cleavage experiment will always exceed W_{sep}, but, with other things being equal, the greater W_{sep}, the greater the energy needed to cleave the interface. Here, we evaluate the work of separation from the energy difference between the total energies of each interface supercell and the sum of the energies of the isolated Ni and ZrO_2 surface slabs. The unrelaxed surface slab (same as that in the interface slab) was used instead of the relaxed surface slab, because the former (unrelaxed) is useful in interpreting the nature of bonding at the interface while the latter (relaxed) has thermodynamic significance.[32] The bond strength can be estimated from the unrelaxed energies directly. The DFT total energy calculations yield work of separation of 288.5 meV/Å^2 for Zr-t interface and 372.2 meV/ Å^2 for O-t interface. The magnitudes of the work of separations correspond to rather strong metal-ceramic bonding. Notice that for Nb/Al_2O_3 interface, a system with an extremely good adherence, the work of separation is 611.7 meV Å^2, [33] comparable to that obtained for Ni/ZrO_2 interfaces. The bond strength was estimated to be 0.95 eV for interface Zr—Ni bonds and 1.24 eV for interface O—Ni bonds respectively. The magnitudes of bond strength obtained here are in good agreement with that from Beltran *et al.*[9] for the same interfaces, Ni(001)/ZrO_2(001) interfaces. Compared to the Ni(111)/ZrO_2(111) interface,[34] the bond strength for Ni(001)/ZrO_2(001) interfaces is around five times larger. Therefore, the Ni(001)/ZrO_2(001) interface has much stronger interface bonds and larger metal-ceramic adhesion energy. The strong bonding at Ni(001)/ZrO_2(001) interfaces also explains why epitaxial growth of Ni on ZrO_2(001) is possible at growth

situations where thermodynamic parameters dominate, *e.g.*, high temperature and low growth rate, as discussed in Sec. 4.2.2.

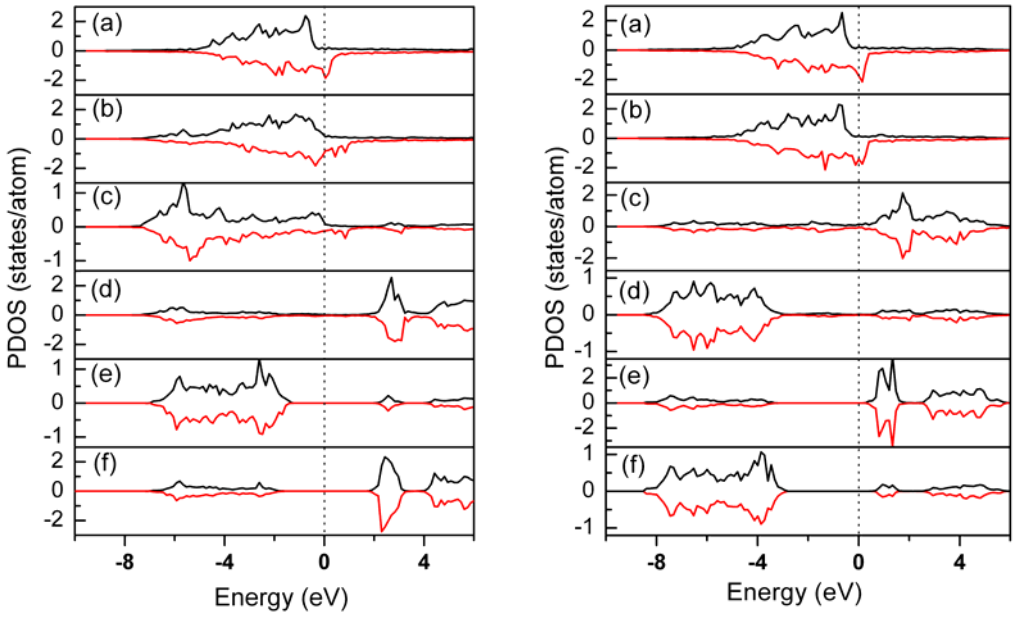

Fig. 4.11 Spin-resolved and atom-projected density of states (PDOS) for O-t (left panel) and Zr-t (right panel) interfaces. For left panel, (a) bulk-Ni, (b) interface-Ni, (c) interface-O in directly bonding with Ni, (d) interface-Zr below interface-O, (e) bulk-O, and (f) bulk-Zr. For right panel, (a) bulk-Ni, (b) interface-Ni, (c) interface-Zr in directly bonding with Ni, (d) interface-O below interface-Zr, (e) bulk-Zr, and (f) bulk-O.

Figure 4.11 shows the spin-resolved and atom-projected density of states (PDOS) for O-t (left panel) and Zr-t (right panel) interfaces. The PDOS in the central layer of Ni and ZrO_2 planes are very close those of the respective bulk crystals. Interface effects are restricted to the atomic planes in contact. For the metal side, they are already screened at the second layer because of the small Thomas-Fermi screening length. The PDOS for interfacial O (Zr) atoms are perturbed by the formation of interface, with not only the appearance of metal induced gap states (MIGS), but also bonding peaks at well-defined energy position. However, both types of interface states

are rather localized at the interface and disappear beyond the second layer from the interface. One important difference between the PDOS for O-t and Zr-t interfaces is the location of the Fermi level in the central layer of the oxide, which is shifted towards the conduction band minimum (CBM) from O-t to Zr-t interface. Notice that this shift is not due to the finite size of the slab, but indicates the variation of Schottky barrier height due to the different interface bonding.

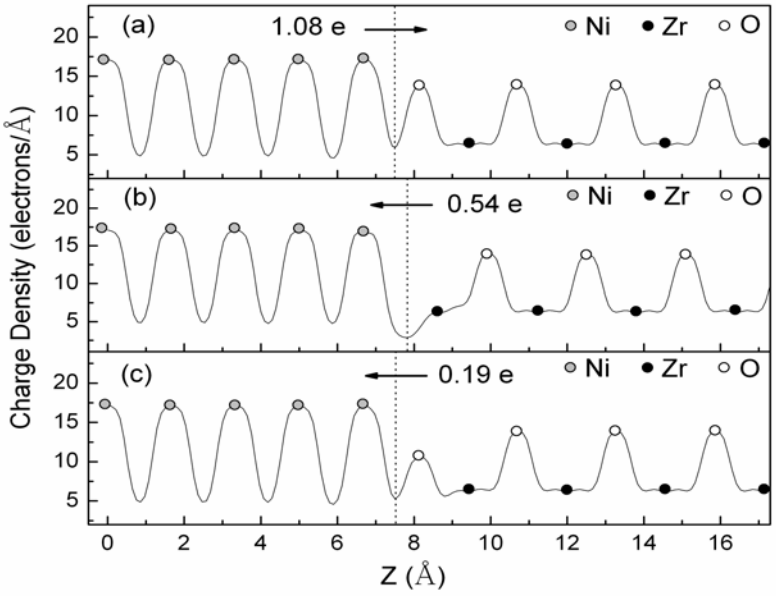

Fig. 4.12 Charge-density distribution for O-t (a), Zr-t (b) and O-v (c) interface supercells along the Z axis, as totaled in the x-y plane. The vertical dotted lines mark the interface between the Ni and *c*-ZrO_2.

The charge-density is plane-totaled in the plane parallel to the interface (x-y plane) and is plotted in the direction perpendicular to the interface or Z axis, as shown in Fig. 4.12. Half of the supercell is shown. It is important to note that the interface O atom in O-t is still negatively charged and the interface Zr atom in Zr-t is positively charged. Such ionic charge is supposed to induce image charge in the metal side. We assumed the minimum of the charge density between Ni and ZrO_2 (as shown in Fig. 4.12 by the dotted lines) to be the separation of two sides. The calculated charge transfer is 1.08,

0.54 and 0.19 electrons per 1×1 basal area for O-t, Zr-t and O-v interface respectively. For O-t interface, electrons are transferred from Ni side to ZrO_2 side; while for Zr-t and O-v interfaces, the direction of charge transfer is reversed.

4.4.3 Calculations of SBHs for model Ni/ZrO_2 interfaces

In this study, the p-type SBH for the Zr-t, O-t and O-v interfaces have been determined from the DFT-GGA calculations adopting the standard "bulk plus lineup" procedure[35, 36]:

$$\Phi_p = \Delta E_p + \Delta V \tag{4.6}$$

where ΔE_p is the energy difference between the metal Fermi level and the oxide valence band maximum (VBM), each measured relative to the average total-potential in the corresponding crystal, and ΔV is the total-potential lineup through the interface. The total local potential includes two parts: electrostatic part and exchange-correlation part. The band-structure term ΔE_p is only the characteristic of the two bulk components and is not related to the interface structure; while the lineup term ΔV summarizes all the intrinsic interface effects, such as the interface chemical composition, orientation and defects in the interface. [37]

To get more accurate results comparable to the experimental results, ΔE_p should include quasiparticle and spin-orbital corrections. As a ground state property, ΔV is accurately determined within DFT. For transition metal Ni, -0.29 eV correction (The negative sign means the FL correction will decrease the p-type SBH.) was added by comparing our DFT GGA calculations value (4.93 eV) and the experimental value (5.22 eV) for the work function of Ni (001) surface. For oxide, we neglect spin-orbit corrections, as the valence states are oxygen-derived. The quasiparticle corrections to

the oxide bulk valence-band edges at the GW level are essential because the corrections are substantial for oxides. We apply +1.23 eV for ZrO_2 [38] valence-band maximum (The positive sign means that the valence band shift will increase the *p*-type SBH.). The overall corrections, +0.94 eV, will be used in the following SBH calculation.

Figure 4.13 shows the in-plane-averaged total potential and the potential line-up using the double-macroscopic average technique[39] for Zr-t, O-t and O-v supercells. The potential line-up ΔV is defined as the difference between the two plateau values residing in the respective bulk-like regions (far enough from the interface). The GGA values for the *p*-type SBH were calculated from Eq. (4.6) using the above values of ΔV and the band structure term ΔE_p (3.55 eV+0.94 eV, the calculated GGA plus correction value), as shown in Fig. 4.13.

The dramatically different SBH values between different Ni/ZrO_2 interface structures indicates that Schottky-barrier height does depend on the interface-specific features, in contrast with the traditional FL pinning model[40] where the pinning position in the MIGS' was intrinsic to the respective semiconductors at a defect-free interface. The SBH dependence on the interfacial structures has also been found for metal-semiconductor contacts both experimentally and theoretically. [41, 42, 43, 28] The interface dependence of SBH for Ni/ZrO_2 stack can be understood in terms of surface charge and image-charge effects. There is a potential difference established between the surface ionic charge and the induced image charge. For anion termination (O-t interface), the interface dipole shifts the average potential energy in the oxide upward with respect to the value in the metal, decreasing Φ_p; while for cation termination (Zr-t interface), the interface dipole shifts the potential in the oxide downward,

increasing Φ_p. The interface oxygen vacancies tend to increase the SBH because of the disappearance of some negatively charged oxygen anions.

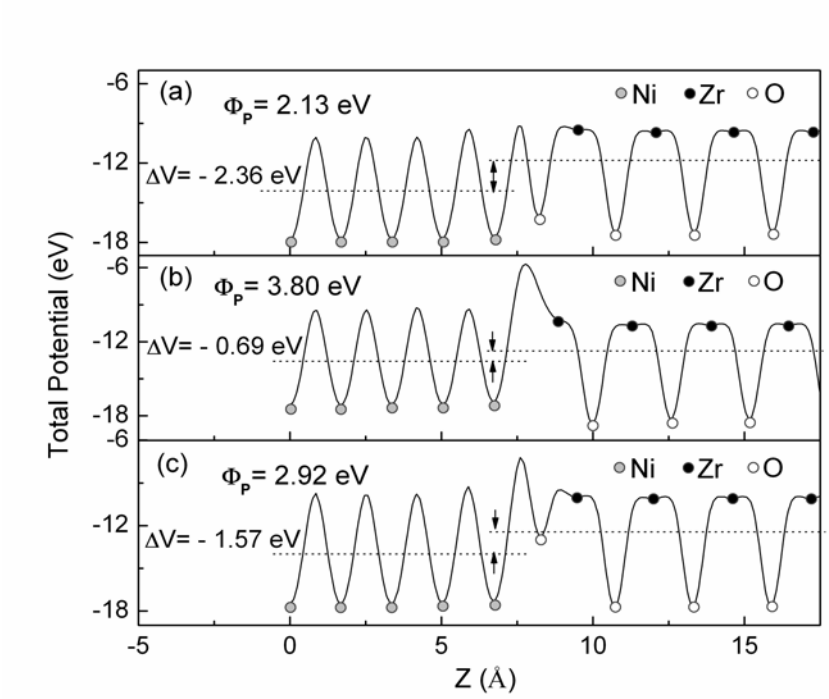

Fig. 4.13 In-plane-averaged total potential for O-t (a), Zr-t (b) and O-v (c) interfaces, half of the supercell shown. ΔV stands for the line up and Φ_P for the p-type SBH.

Table 4.1 Comparison of calculated (DFT-GGA) and experimental values of Schottky barrier heights for Ni/ZrO_2 interfaces.

Method	Structure	Φ_P (eV)	Φ_n (eV)
DFT-GGA	O-t	2.13	3.67
	Zr-t	3.80	2.00
	O-v	2.92	2.88
XPS	O-rich	2.60	3.20
	O-deficient	3.36	2.44
IPE[a]		2.2	3.2

[a] Reference 44.

In Table 4.1, we summarized the calculated and experimental *p*(*n*)-type SBH Φ_p (Φ_n). The calculated differences in SBH are larger than the experimental ones, which is attributed to the structure differences between the experiment and calculation. In the calculation, O-t structure corresponds to the limit situation of O-rich interface, while in the experiment, annealing in UHV will incur the losing of some surface-oxygen, making the interface somewhat O-v structure like. What we want to emphasize here is the variation trend of the SBH, which is confirmed by both the experimental and theoretical results. That is, interface Ni-O bonds tend to decrease Φ_p, while Ni-Zr bonds or O-vacancies increasing it. Using internal electron photoemission (IPE), Afanas'ev *et al.* [44] have measured the Φ_n for Ni on nanometer-thin ZrO_2 to be 3.2 eV (or 2.2 eV for Φ_p using the band gap value of ZrO_2 therein), which is in good agreement with our results for O-rich interface.

4.4 Chapter Summary

High-quality fcc-Ni was grown epitaxially on yttrium-stabilized cubic ZrO_2(001) surfaces in ultrahigh vacuum (UHV). The epitaxial relationship was determined by *ex situ* high resolution TEM (HRTEM) to be Ni(001)//ZrO_2(001) and Ni[110]//ZrO_2[100]. *In-situ* x-ray photoemission methods were applied to accurately determine the Schottky barrier height for Ni/ZrO_2(001) interfaces. Depending on different surface treatment of ZrO_2(001) surfaces, *e.g.,* ideal ZrO_2(001) surface terminated by oxygen layer and Ar^+ ions sputtered surface with many oxygen vacancies, the interface effects on SBH were investigated. It was found that O-rich interface has a lower SBH than O-deficient interface (2.60 eV vs. 3.36 eV). Such interface dependence of SBH has been explained by first-principles calculations for three types of Ni/ZrO_2 model interfaces:

oxygen-terminated interface full of Ni-O interfacial bonds, zirconium-terminated interface full of Ni-Zr interfacial bonds, and interfaces incorporating oxygen vacancies The interface dipole formed by Ni-O bonds at the interface tends to decrease p-type SBH, while Ni-Zr bonds or oxygen vacancies at the interface increasing it. The results show that the SBH at Ni/ZrO_2 interfaces can be engineered for the metal gate application in CMOS devices through the interface structure-control.

References

[1] The International Technology Roadmap for Semiconductor 2005, URL: http://public.itrs.net.

[2] Yee-Chia Yeo, Tsu-Jae King, and Chenming Hu, J. Appl. Phys. **92**, 7266 (2002).

[3] J. Robertson and C. W. Chen, Appl. Phys. Lett. **74**, 1168 (1999).

[4] I. De, D. Johri, A. Srivastava, and C. M. Osburn, Solid-State Electron. **44**, 1077 (2000).

[5] J. K. Schaeffer, L. R. C. Fonseca, S. B. Samavedam, Y. Liang, P. J. Tobin, and B. E. White, Appl. Phys. Lett. **85**, 1826 (2004).

[6] Y. F. Dong, S. J. Wang, J. W. Chai, Y. P. Feng, and A. C. H. Huan, Appl. Phys. Lett. **86**, 132103 (2005).

[7] G. D. Wilk, R. M. Wallace, and J. M. Anthony, J. Appl. Phys. **89**, 5243 (2001).

[8] S. J. Wang and C. K. Ong, Appl. Phys. Lett. **80**, 2541 (2002).

[9] J. I. Beltran, S. Gallego, J. Cerda, J. S. Moya, and M. C. Munoz, Phys. Rev. B **68**, 075401 (2003).

[10] S. A. Chambers, T. Droubay, T. C. Kaspar, M. Gutowski, and M. van Schilfgaarde, Surf. Sci. **554**, 81 (2004).

[11] F. Ernst, P. Pirouz, and A. H. Heuer, Philos. Mag. A **63**, 258 (1991).

[12] Andreas Eichler and Georg Kresse, Phys. Rev. B **69**, 045402 (2004).

[13] E. A. Kraut, R. W. Grant, J. R. Waldrop, and S. P. Kowalczyk, Phys. Rev. Lett. **44**, 1620 (1980).

[14] R. A. McKee, F. J. Walker, M. B. Nardelli, W. A. Shelton, and G. M. Stocks, Science **300**, 1726 (2003).

[15] A. C. Tuan, T. C. Kaspar, T. Droubay, J. W. Rogers, and S. A. Chambers, Appl. Phys. Lett. **83**, 3734 (2003).

[16] S. J. Wang, A. C. H Huan, Y. L. Foo, J. W. Chai, J. S. Pan, Q. Li, Y. F. Dong, Y. P. Feng, and C. K. Ong, Appl. Phys. Lett. **85**, 4418 (2004).

[17] M. J. Guittet, J. P. Crocombette, and M. Gautier-Soyer, Phys. Rev. B **63**, 125117 (2001).

[18] S. A. Chambers, Y. Liang, Z. Yu, R. Droopad, J. Ramdani, and K. Eisenbeiser, Appl. Phys. Lett. **77**, 1662 (2000).

[19] M. Copel, P. R. Duncombe, D. A. Neumayer, T. M. Shaw, and R. M. Tromp, Appl. Phys. Lett. **70**, 3227 (1997).

[20] F. Flores, A. Muñoz, and J. C. Durán, Appl. Surf. Sci. **41/42**, 144 (1989).

[21] John Robertson, J. Vac. Sci. Technol. B **18**, 1785 (2000).

[22] J. Tersoff, Phys. Rev. B **30**, 4874 (1984).

[23] A. A. Demkov, L. R. C. Fonseca, E. Verret, J. Tomfohr, and O. F. Sankey, Phys. Rev. B **71**, 195306 (2005).

[24] G. Kresse and J. Hafner, Phys. Rev. B **47**, 558 (1993); G. Kresse and J. Hafner, Phys. Rev. B **48**, 13115 (1993).

[25] G. Kresse and J. Furthmuller, Comput. Mater. Sci. **6**, 15 (1996); G. Kresse and J. Furthmuller, Phys. Rev. B **54**, 11169 (1996).

[26] D. Vanderbilt, Phys. Rev. B **41**, 7892 (1990).

[27] J. P. Perdew, J. A. Chevary, S. H. Vosko, K. A. Jackson, M. R. Pederson, D. J. Singh, and C. Fiolhais, Phys. Rev. B **46**, 6671 (1992).

[28] J. Padilla and David Vanderbilt, Phys. Rev. B **56**, 1625 (1997).

[29] K. Reuter and M. Scheffler, Phys. Rev. B **65**, 035406 (2002).

[30] A. Eichler and G. Kresse, Phys. Rev. B **69**, 045402 (2004).

[31] M. W. Finnis, J. Phys.: Condens. Matter **8**, 5811 (1996).

[32] I. G. Batirev, A. Alavi, M. W. Finnis, and T. Deutsch, Phys. Rev. Lett. **82**, 1510 (1999).

[33] W. Zhang and J. R. Smith, Phys. Rev. Lett. **82**, 3105 (1999).

[34] A. Christensen and Emily A. Carter, J. Chem. Phys. **114**, 5816 (2001).

[35] S. H. Wei and A. Zunger, Phys. Rev. Lett**. 59**, 144 (1987).

[36] M. Peressi, N. Binggeli, and A. Baldereschi, J. Phys. D **31**, 1273 (1998).

[37] Alfonso Franciosi and Chris G. Van de Walle, Surf. Sci. Rep. **25**, 1 (1996).

[38] B. Kralik, E. K. Chang, and S. G. Louie, Phys. Rev. B **57**, 7027 (1998).

[39] A. Baldereschi, S. Baroni, and R. Resta, Phys. Rev. Lett. **61**, 734 (1988).

[40] J. Tersoff, Phys. Rev. Lett **52**, 465 (1984).

[41] Raymond T. Tung, Phys. Rev. Lett. **84**, 6078 (2000).

[42] M. van Schilfgaarde and N. Newman, Phys. Rev. Lett. **65**, 2728 (1990).

[43] D. A. Ricci, T. Miller, and T.-C. Chiang, Phys. Rev. Lett. **93**, 136801 (2004).

[44] V. V. Afanas'ev, M. Houssa, and A. Stesmans, J. Appl. Phys. **91**, 3079 (2002).

Chapter 5

Chemical tuning of band alignments for metal gate/high-*k* oxide interfaces

5.1 Introduction

As discussed in Chapter 1, the continual downscaling of semiconductor devices into the "nano" era requires not only the replacement of silicon dioxide (SiO_2) gate dielectric by high dielectric constant (high-*k*) materials, [1, 2, 3, 4, 5, 6] but also that of polycrystalline Si (poly-Si) gate electrodes by metal gates. [7, 8, 9] This is because poly-Si electrodes have serious problems related to gate depletion, boron penetration, high gate resistance, and poor compatibility with high-*k* gate dielectric, such as ZrO_2 and HfO_2. In an actual metal-oxide-semiconductor field-effect transistor (MOSFET) device, it is the effective work function of metal gate ($\Phi_{m,eff}$), the energy position of metal Fermi level in the Si channel, that determines the effective confinement of carriers and the gate threshold voltage. The integration of metal gate with high-*k* gate dielectric requires the effective metal work functions ($\Phi_{m,eff}$) to be within ±0.1 eV of the Si valence- and conduction-band edges for *p*- and *n*-channel MOSFETs, respectively. [10] However, to find two metals with suitable work functions and to integrate them with current semiconductor technology remain a challenge. In addition, the selection of metal gate materials is not straightforward because the effective work function of a metal depends on the underlying gate dielectrics and could differ appreciably from the metal work function in vacuum ($\Phi_{m,vac}$)[7, 11]. In order to identify the right metal gate

material, understanding and controlling the interfaces between metal gate electrode and high-κ dielectric at the atomic scale is essential.

In this chapter, we propose a method for atomic-level chemical tuning of band alignment for metal gate on high-*k* dielectric, which aims to provide not only a practical way of modifying the band alignments for metal gate/high-*k* oxide interfaces to satisfy the engineering requirement for the metal gate technology, but also fundamental understanding of the metal-dielectric interfaces at atomic scale.[12]

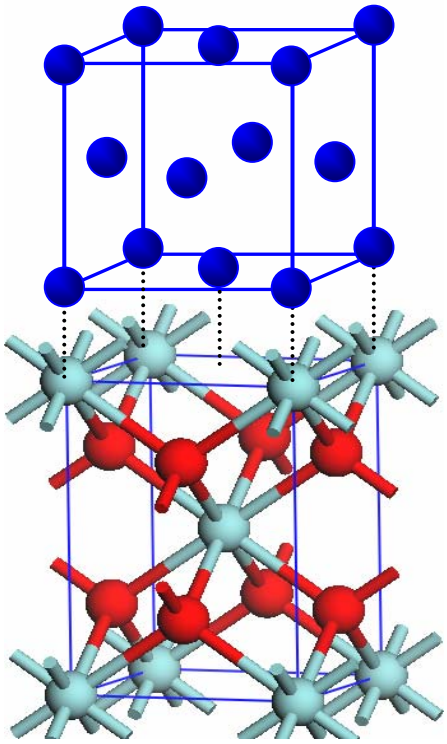

Instead of growing the metal directly on the oxide, we proposed to include a layer of heterovalent metal *m* (*m* = Au, Pt, Ru, Mo, Al, V, Zr, Ti and W) between them. Due to different electronegativity of the heterovalent metal atoms, the interlayer is expected to change the interface electric dipole moment and result in changes in the band alignment at the metal-oxide interfaces. Chemical tuning of Schottky barrier height (SBH) and effective metal work function can be achieved by using different metals or different coverage for the interlayer.

Fig. 5.1 Lattice matching between fcc-Ni (up) and cubic-ZrO_2 (down) along [001].

5.2 Models and calculation

Cubic ZrO_2 (*c*-ZrO_2) and fcc Ni were used in our study as the prototypes for the high-*k* dielectric gate oxides and metal gate electrodes, respectively. Ni has very good lattice match to ZrO_2 after relative 45^0 rotation in (001) plane, as shown in Fig. 5.1, which allows fabrication of high quality metal-oxide interface.

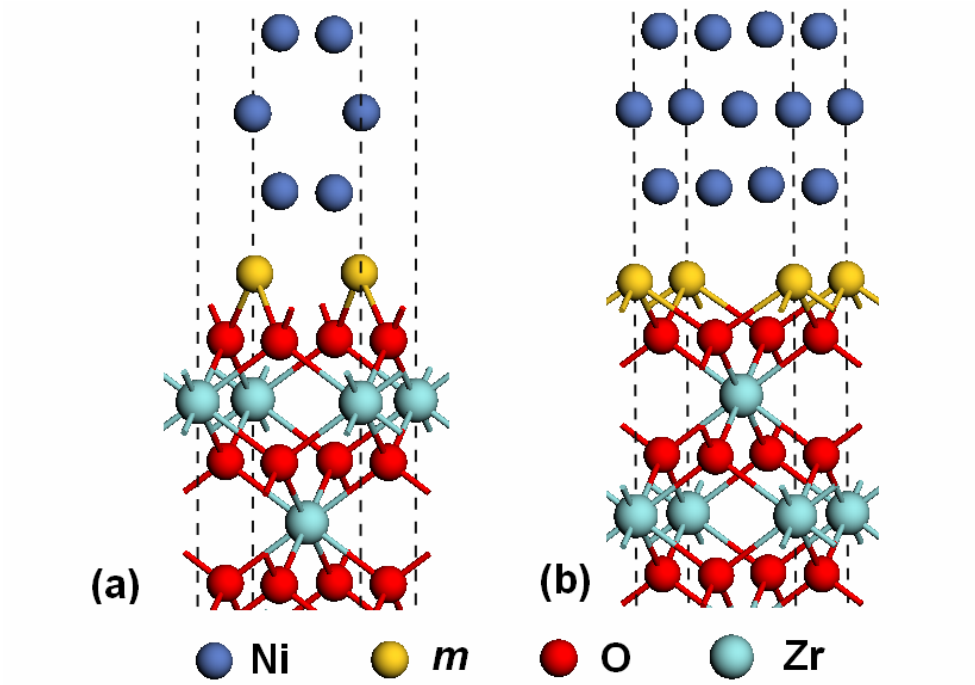

Fig. 5.2 Supercells for the Ni-*m*-ZrO_2 interfaces, (a) with one monolayer metal *m* (*m*=Ni, V, and Al), (b) with half monolayer metal *m* (m=Au, Pt, Ni, Ru, Mo, Al, V, Zr and W). The interface is formed using *c*-ZrO_2(001) and fcc Ni(001) surfaces, with either half or one monolayer of heterovalent metal (*m*) between them.

We consider two models, one with a full monolayer of heterovalent atoms (Fig. 5. 2-a) and the other with half monolayer (Fig. 5. 2-b) between an oxygen-terminated ZrO_2 (001) surface and Ni (001). First-principles method based on the spin-polarized density functional theory (SDFT) was used to investigate the structure and properties of the Ni(001)-*m*-ZrO_2(001) interfaces. Total energy calculations were carried out using the Vienna *ab-initio* simulation package (VASP)[13, 14], with Vanderbilt ultrasoft pseudopotentials[15], and the generalized gradient approximation (GGA) [16] for exchange and correlation. A plane-wave cut-off corresponding to a kinetic energy of 350 eV was used. A **k** point mesh of 8×8×1 was used to sample the (1×1) interface supercell (3.647 Å×3.647 Å). In the plane parallel to the interface (*xy* plane), the lattice constant was constrained to that of bulk *c*-ZrO_2. The lattice constant normal to the interface (*z*-

direction) and atomic positions were fully optimized to minimize the total energy. Density of states (DOS) were calculated with finer **k**-meshes (~ 0.02 $Å^{-1}$) using the tetrahedron method with Blöchl corrections[17] as implemented in VASP. The atom-projected DOS (PDOS) was obtained by projecting electronic Blöch states onto spherical harmonics inside spheres, centered at each ionic site. The choice of radii corresponds to volume-conserving spheres at the equilibrium lattice constants for respective bulk materials.[18] For example, the radius of Ni was set to be 1.38 Å so that the sum of the spheres is close to the total volume of the cell (fcc-Ni at its equilibrium lattice constant). For binary system, *e.g.* ZrO_2, we set $r_{Zr} \sim r_{ps}^{r}$, where r_{ps}^{r} is the pseudization radium for Zr and determine r_O from the volume conserving requirements for *c*-ZrO_2 at the equilibrium lattice constant.

5.3 Electronic structures at interfaces: MIGS versus chemical bonding

Figures 5. 3 (a) and (b) show the spin-resolved and atomic site-projected density of states (PDOS) of two interfaces, Ni-Pt-ZrO_2 and Ni-Al-ZrO_2 with half monolayer of Pt and Al, respectively. In these and all systems being studied, the PDOS of atoms far from the interface (bulk region) are essentially the same as those in bulk fcc Ni or *c*-ZrO_2. But the position of the Fermi level in the band gap of bulk oxide is strongly dependant on the interfacial metal *m*. This is an indication that inclusion of the heterovalent metal changes interface dipoles. The interface oxygen ions are noticeably perturbed by the formation of the interface, with not only the gap states appearing in the PDOS of interface oxygen at the gap region, but also bonding peaks related to interfacial bonds at well-defined energy positions. For metal induced gap sates (MIGS), it is continuous, structureless, and only appears in the oxide band gap energy

region;[19] while for the interface state induced by interface bonding, it is at well-defined energies (not only in the oxide band gap energy range).[20, 21] The shape of PDOS for interfacial oxygen (O-Int in Fig. 5.3.) has been modulated by that of the interfacial metal atom, which is attributed to the formation of interfacial oxygen-metal chemical bonds. It is convenient to consider two sources for the gap states, contribution from the interfacial chemical bonds and contribution from the tails of the metallic wave functions which tunnel into the oxide band gaps or conventional metal induced gap states (MIGS)[22]. The former is localized in the interfacial bond region, while MIGS decay exponentially inside the oxide.

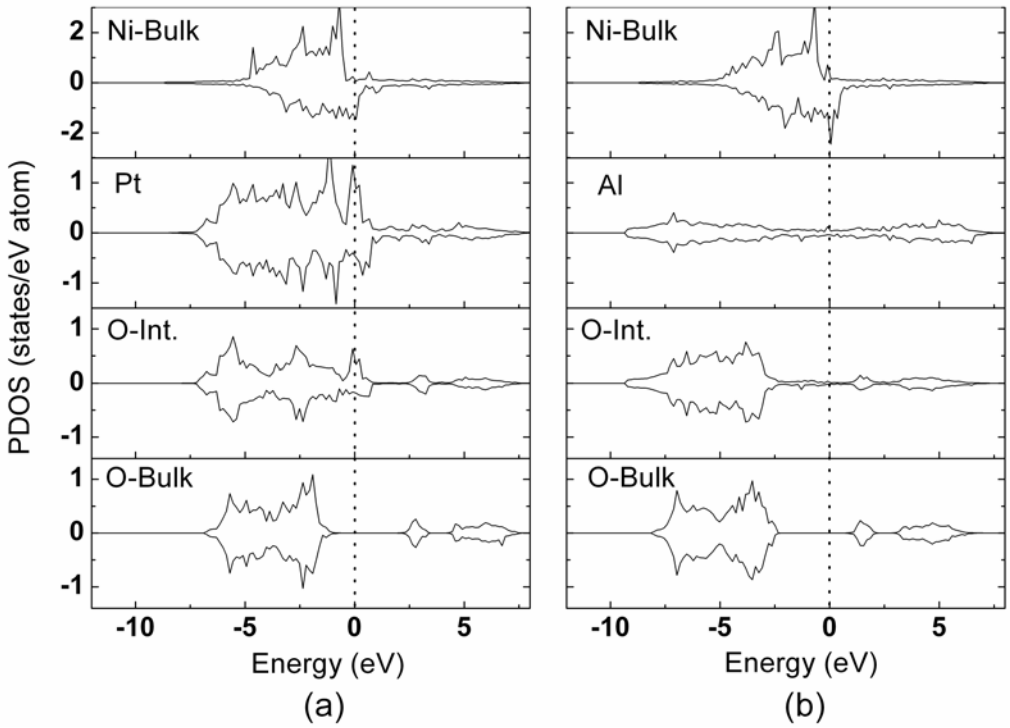

Fig. 5.3 Spin resolved and atomic site-projected density of states (PDOS) for (a) Ni-Pt-ZrO_2 interface and (b) Ni-Al-ZrO_2 interface, with half monolayer of metal insertion. The PDOS for the Ni in the bulk region (Ni-bulk), interface metal *m* (Pt or Al), interface oxygen (O-Int.), and oxygen in the bulk region (O-bulk) are shown.

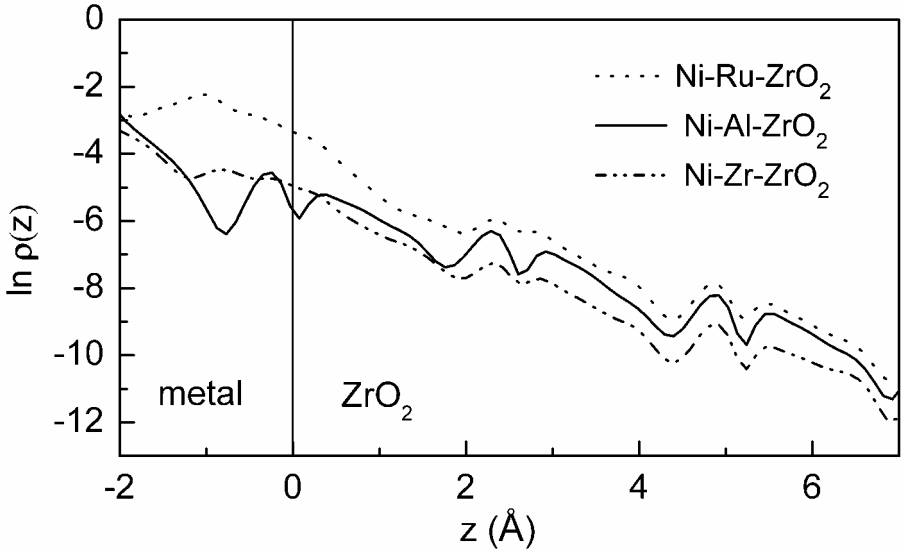

Fig. 5.4 Penetration of electronic density $\rho(z)$ of the gap states into the ZrO_2 of Ni-*m*- ZrO_2 (*m* = Ru, Al, Zr) interfaces. Position of the surface oxygen is set to *z* = 0 Å. The penetration profiles for other Ni-*m*-ZrO2 interfaces are similar and are not shown.

To closely examine the spatial dispersion of the occupied gap states, we calculated the corresponding charge density profile along the normal direction of the interface

$$\rho(z) = A^{-1}(E_F - E_{VBM})^{-1}\int_{E_{VBM}}^{E_F} \rho(x,y,z)dEdxdy \qquad (5.1)$$

where the *xy* plane coincides with the interface and *z*-direction is along the interface normal, *A* is the basal area of interface supercell. The calculated charge density profile is shown as a function of *z* in Fig. 5. 4. Apart from the oscillations around the atom cores, the charge density decreases exponentially inside the oxide, with a decay length of $\lambda_{ZrO_2} \sim 0.9$ Å which is nearly independent of the type of the metal and should be viewed as a property of *c*-ZrO_2 bulk. This decay length is rather short compared to that in Si (3.0 Å) and GaAs (2.8 Å) [23], which is consistent with the relatively larger Schottky pinning parameter (S, 0 corresponding to the Barding limit of strong pinning, 1 to the Schottky-Mott picture) for high-*k* oxides than for Si and GaAs in the MIGS model. [24, 25] With the short decay length, MIGS is not expected to contribute

considerably to the band alignment between the metal and high-*k* oxide because the electrostatic potential from the interface dipole cannot be efficiently screened by MIGS.

5.4 Schottky barrier height at Ni/m/ZrO_2(001) interfaces

The *p*-type Schottky barrier height (*p*-SBH) Φ_p was determined using the standard bulk-plus-lineup[26, 27] approach, with the average electrostatic potential at the ion core (V_{core}) in the "bulk" region as reference energy,

$$\Phi_p = \Delta E_b + \Delta V \tag{5.2}$$

where ΔE_b is the difference between the Fermi energy of Ni and the energy of the valence band maximum (VBM) of the oxide, each measured relative to V_{core} of the corresponding "bulk" ions, and ΔV is the lineup of V_{core} through the interface.

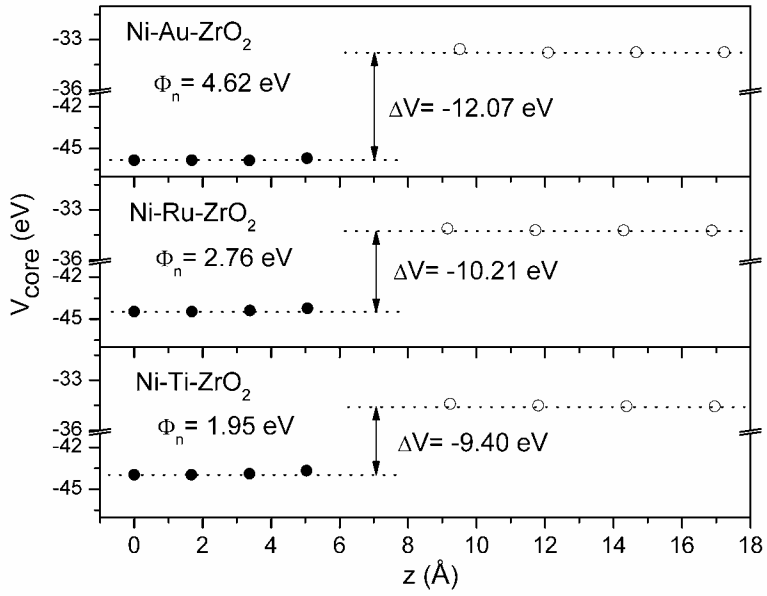

Fig. 5.5 Average electrostatic potential at the cores (V_{core}) of Ni (filled dark circle) and Zr (open circle) as a function of the distance from the interface for Ni-*m*-ZrO_2 interfaces (*m*= Au, Ru, Ti) with half monolayer metal insertion. Breaks were introduced in the vertical axis (V_{core}) between - 41 eV and -36 eV.

The average electrostatic potential V_{core} of Zr ions in the oxide and that of Ni atoms in the Ni-*m*-ZrO_2 interfaces are shown as a function of distance from the interface in Fig. 5. 5. The V_{core} of the Ni ions near the interface were perturbed by the interface dipole, but quickly recovered its value in bulk region. On the oxide side, V_{core} for Zr ions have converged to its bulk value at the second Zr layer which is consistent with the short decay length of MIGS in ZrO_2. ΔV was evaluated from the difference in V_{core} of the Zr and Ni ions in their respective bulk regions.

The *p*-SBHs (Φ_p) were calculated from Eq. (2) for various Ni-*m*-ZrO_2 interfaces using the calculated ΔV and the quasiparticle[28, 29] and spin-orbital corrected ΔE_b. The *n*-SBH (Φ_n) was derived from $\Phi_n = E_g - \Phi_p$, where E_g is the energy gap of the dielectric. The experimental band gap of 5.82 eV[30] was used here instead of the DFT-GGA result because of the well-known underestimation of the latter. The effective metal work function ($\Phi_{m,eff}$) on the oxide was evaluated using the formula $\Phi_{m,eff} = \Phi_n - CBO + EA$, where CBO is the conduction band offset between the oxide and the Si substrate (1.75 eV from Ref. 22), and EA is the electron affinity of Si (4.05 eV). The Mulliken charges (in Table I) for interface metal *m* were calculated using Cambridge sequential total energy package (CASTEP).[31]

The calculated *n*-SBHs and effective metal work functions are listed in Table 5.1 for the Ni-*m*-ZrO_2 interfaces with various interlayer metals. The corresponding Fermi levels of metal gate electrodes in Ni-*m*-ZrO_2-Si capacitors (the coverage of interlayer metal *m* is 0.5.) were also depicted in Fig. 5. 6. It can be seen that a tunability as wide as 2.8 eV for Φ_n ($\Phi_{m,eff}$) can be achieved for Ni-*m*-ZrO_2 interfaces by simply introducing half or one monolayer of heterovalent metal *m* between Ni and ZrO_2. Furthermore, we found that *n*-SBHs and effective metal work functions follow a crude

chemical tuning trend: for a given metal *m* coverage (half or one monolayer), the *n*-SBH (effective work function) increases linearly with the electronegativity (χ) of the interlayer metal atom *m*. The effective work function data for the Ni-ZrO_2-Si MOS structures with half monolayer of metal *m* between Ni and ZrO_2 were fitted to a straight-line, as shown in Fig. 5.7. The simple linear relationship between $\Phi_{m,eff}$ and χ is obeyed by most transition metals except Al and W. The exceptional case of Al is probably due to its simple metal character (*s* and *p* valence electrons), in contrast to the transition metals (including *d* valence electrons). But reason is not clear for the exceptional behavior of tungsten.

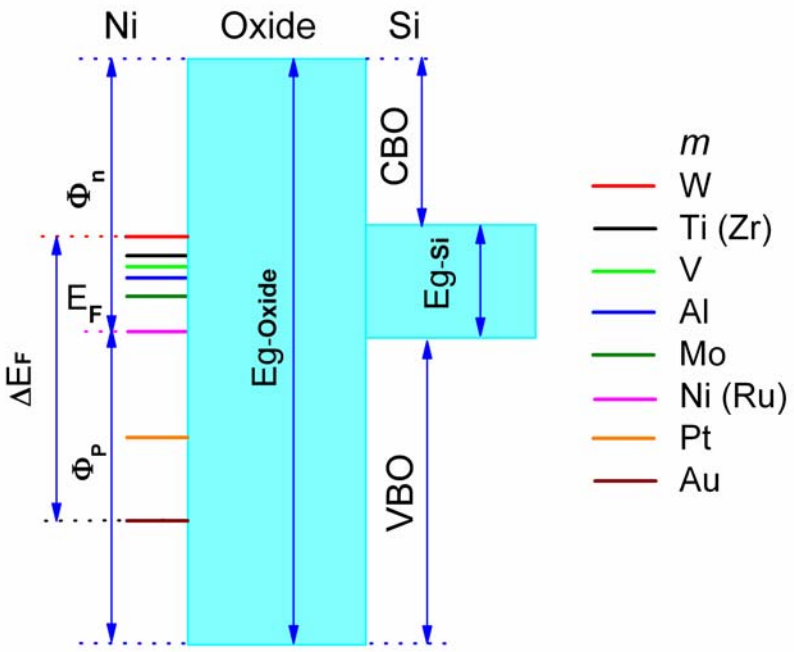

Fig. 5.6 Energy band diagram of Ni-ZrO_2-Si (MOS) structures with an interlayer of heterovalent metal *m* between Ni and ZrO_2. The *n* (*p*)-type Schottky barrier height Φ_n (Φ_p), the conduction band offset (CBO), and valence band offset (VBO), were shown. The energy positions of Fermi level for different interlayer metal *m* were denoted by colored lines (The lines' sequence was shown on the right side.). The tuning range (ΔE_F) of $\Phi_{m,eff}$, by inserting half monolayer of heterovalent metal *m* between Ni and ZrO_2, was also shown.

Table 5.1 Interface metal coverage (θ), electronegativity [a] of metal atom *m* (χ, Mulliken scale, in eV), work function [b] of metal *m* in vacuum ($\Phi_{m,vac}$, in eV), Mulliken charge (Q_m, in *e*), *n*-SBHs (Φ_n, in eV) for Ni-*m*-ZrO_2 interfaces, and effective metal work functions ($\Phi_{m,eff}$, in eV) for Ni-*m*-ZrO_2-Si capacitors.

m	θ	χ	$\Phi_{m,vac}$	Q_m	Φ_n	$\Phi_{m,eff}$
Au	0.5	5.77	5.1	0.16	4.62	6.92
Pt	0.5	5.6	5.65	0.16	3.84	6.14
Ni	0.5	4.40	5.15	0.37	2.76	5.06
Ru	0.5	4.5	4.71	0.27	2.76	5.06
Mo	0.5	3.9	4.6	0.51	2.38	4.68
Al	0.5	3.23	4.28	1.06	2.18	4.48
V	0.5	3.6	4.3	0.69	2.09	4.39
Zr	0.5	3.64	4.05	1.01	1.96	4.26
Ti	0.5	3.45	4.33	0.80	1.95	4.25
W	0.5	4.40	4.55	0.15	1.80	4.10
Ni	1	4.40	5.15	0.24	3.63	5.93
V	1	3.6	4.3	0.44	2.65	4.95
Al	1	3.23	4.28	0.63	1.82	4.12

[a]Ref. [32]; [b]Ref. [33]

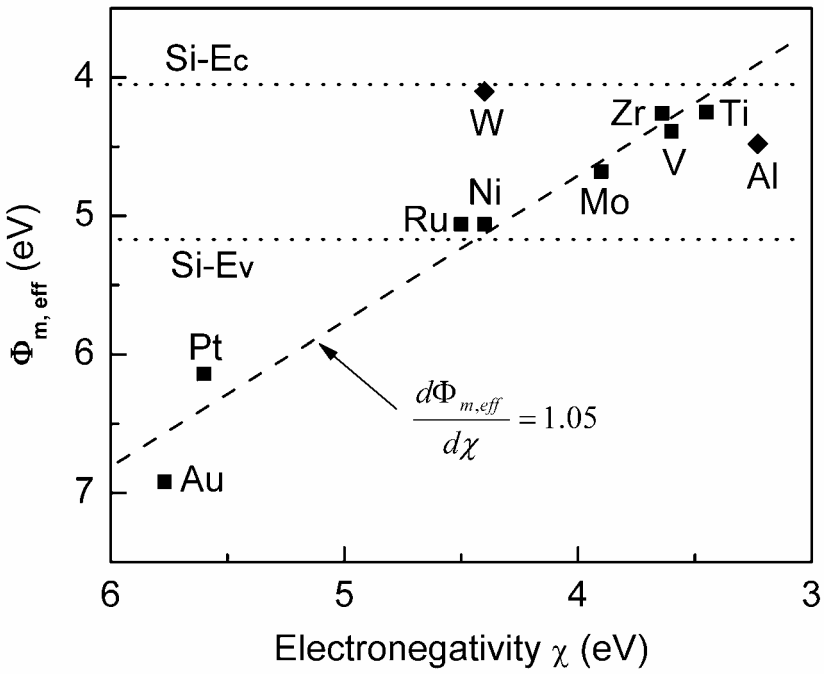

Fig. 5.7 Effective work functions ($\Phi_{m,eff}$) of Ni-ZrO_2-Si structures with half monolayer of heterovalent metal *m* between Ni and ZrO_2 are shown as a function of electronegativity of interlayer metal *m*. The straight line is a least-square fit to data points shown in filled squares (Al and W are not included). The Si conduction band edge (E_C) and valence band edge (E_V) are at 4.05 eV and 5.17 eV, respectively.

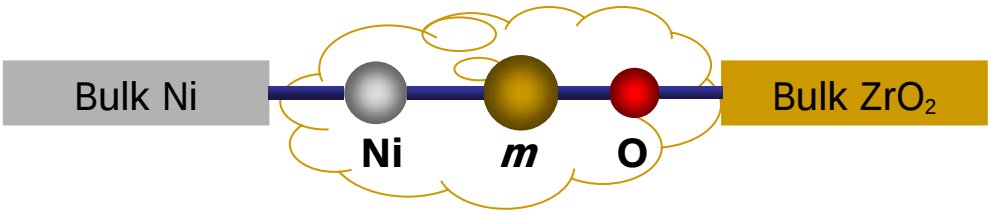

Fig. 5.8 Carton of Ni-*m*-ZrO_2 interfaces illustrating the interface bonding.

The above linear chemical tuning trend is certainly due to the localized interfacial dipole formed by different interfacial chemical bonds. Because of the short decay length (0.9 Å) of MIGS in ZrO_2, the localized interface dipole formed by interfacial polarized bonds plays a dominating role compared to MIGS in the determination of Schottky barrier heights for the metal-dielectric oxide interfaces. We may regard the

interface region as a large "molecule"[34] which connects the Ni bulk reservoir on one side and ZrO_2 bulk reservoir on the other side, so that the Ni-*m*-ZrO_2 interface takes the form of (Ni-Bulk)–Ni–*m*–O–(ZrO_2-bulk), with –Ni–*m*–O– being the interface specific region, as shown in Fig. 5. 8. The interface dipole comprises two parts, one from the ionic *m*-O bonds, the other from the positively charged metal layer and its image charge in the metal (Ni) side. The former raises all energy levels on the oxide side with respect to the values in the metal, thus increases *n*-SBH, while the latter decreases *n*-SBH. With decreasing electronegativity of *m*, both types of dipole increase. But *n*-SBH decreases which indicates that the net interface dipole is pointing from the metal to the oxide, and the dipole formed by the *m* cation layer and its image charge plays the dominant role in the determination of SBH. This may be the basis for observed chemical tuning trend. The above argument is only based on a phenomenal electrostatic model. We note that without detailed knowledge of the charge redistribution profile, and the microscopic dielectric constant at the interface, the shift of SBH cannot be derived exactly from electrostatic models, although such shift has been obtained self-consistently in our first-principles calculations.

For a comparative study, we also considered Ni(001) surfaces covered by half monolayer of metal atom *m*, using a model system which consists of 9 layers of Ni in the $p(2\times2)$ form with a half monolayer of *m* covering the two identical surfaces of the Ni slab, and a vacuum region of 14 Å thick. In Fig. 5.9, the calculations of vacuum work functions from the slab supercells for Ni(001) surface covered by half monolayer of Pt or Ti are shown. The energy positions of Fermi level were aligned at energy zero and the vacuum work function was evaluated as the energy difference between the respective vacuum level (E_{Vac}) and Fermi level (E_F). One can see that half monolayer

of heterovalent metal overlayer can dramatically change the work function of Ni(001). This result is consistent with that of Park *et al.*'s calculations.[35]

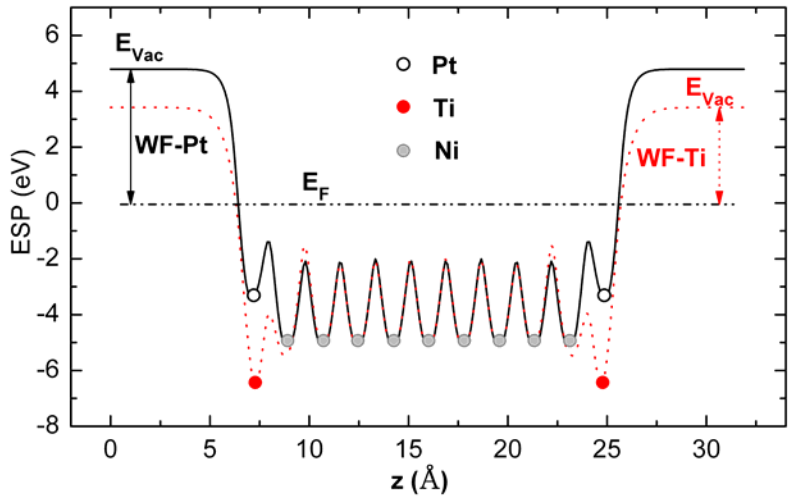

Fig. 5.9 Electrostatic potential (ESP) for Ni(001) surface covered by half monolayer of Pt (solid line) or Ti (dotted line). The Fermi levels were aligned at energy zero and the work functions (WF) were evaluated as the energy difference between the respective vacuum level (E_{Vac}) and Fermi level (E_F).

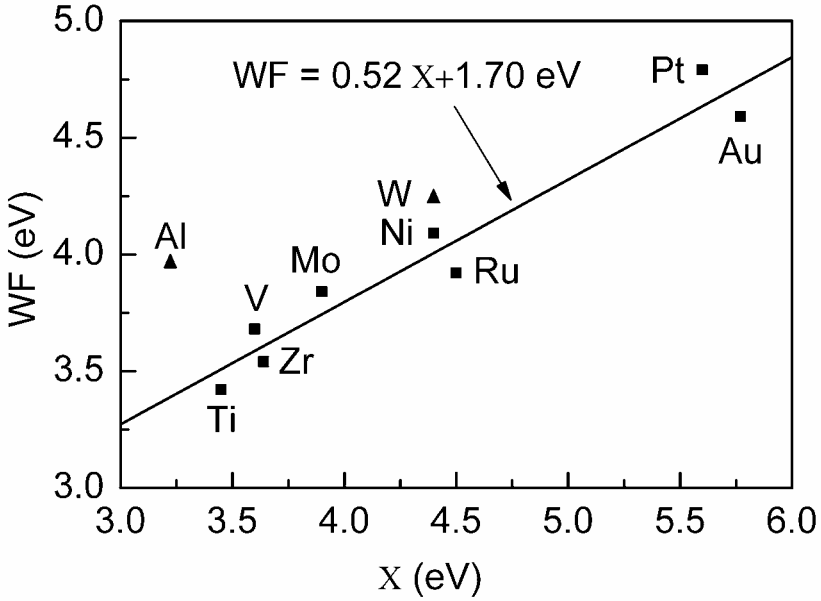

Fig. 5.10 Work functions of Ni(001) with half monolayer of metal *m* coverage are shown as a function of electronegativity (Mulliken scale) of *m*. The straight line is a least-squares fit to data points shown in filled squares.

The calculated work functions (WF) are shown as a function of electronegativity (χ) of atom *m* in Fig. 5. 10. Again, a simple linear relation between WF and χ was found for most of the transition metals considered, with the only exception being Al and W. This is in agreement with the generally accepted concept that if the surface adatom is more electronegative than the substrate, electrons transfer from the substrate to the adsorbate and thus the work function deceases, and vice versa. If we compare the slopes of the straight lines for SBH(χ) in Fig. 5.6 and WF(χ) in Fig. 5.10, although their trends are the same, the chemical tuning effect for the vacuum work function is considerably smaller than that for the SBH. This cautions us that the results obtained from metal vacuum work function studies cannot be directly applied to the estimation of effective work functions for metal-dielectric contacts, and it may not be appropriate for the general practice of deriving effective work function from bulk or pseudo-bulk properties of the component materials (*e.g.*, metal work function and dielectric material charge neutrality level) while disregarding the interface effects.

Recently, Ricci *et al.* [36] demonstrated chemical tuning of metal-Si interfaces by measuring the SBHs with angle-resolved photoemission. The chemical tuning trend for the SBH of metal-Si interfaces obtained in their study is the same as what we found here for the metal-dielectric oxide interfaces, thus lending supports to our finding that interface dipole formed by interfacial metal cation layer and its image charge in the metal plays an important role in the formation of Schottky barrier height. However, the dependence of SBH on electronegativity of interfacial metal is much weaker for the metal-Si interfaces than for the metal-ZrO_2 interfaces, which may be due to the efficient MIGS screening of Si substrate.

In addition to the chemical effects, structural effects, such as interfacial metal *m* coverage, also play important roles in determining Schottky barrier heights. Ni-*m*-ZrO_2

interfaces with one monolayer coverage of Al, V and Ni were investigated similarly. The results shown in Table I indicate that SBH also strongly depends on interfacial structure.

For a comparison of our results with experiments, a few cautions should be in mind. The model assumes that heterovalent metal atoms form a complete layer structure right at the interface, which is a very restrictive condition. The real metal/metal-oxide interface structures should be deposition-process-dependent and there would be many disorders or defects at real metal/metal-oxide interfaces. For example, oxygen-rich or -deficient conditions result in different surface[37] or interface structures[9]; diffusion or aggregation of the interfacial heterovalent metal atoms may be expected at elevated temperature or even at room temperature. The resulting compositional and morphological inhomogeneities will lead to charge rearrangement at the interface which may damp the expected chemical tuning effects.

5.5 Chemical tuning of SBH: experimental evidence

The vapor deposition of metal film onto well-defined oxide surfaces under the clean conditions of ultrahigh vacuum (UHV) provides a controlled method for studying fundamental details concerning metal/oxide interfaces.[38] To experimentally demonstrate the chemical tuning effects of Schottky barrier height (SBH) between Ni and ZrO_2 interfaces, one stringent requirement is to keep the sub-monolayer of heterovalent metal at the Ni-ZrO_2 interface in a two-dimension(2D) geometry instead of aggregating to 3D clusters. Whether the sub-monolayer of metal can "wet" the oxide surface or not depends the competition of adatom-oxide interaction and intra-adatom interaction.[39] If the former is strong enough, all the metal adatoms can have

bonds with the oxide surface and a 2D geometry is formed; otherwise, 3D cluster geometry is preferred for metal adatoms.

Aluminum has high affinities for oxygen (i. e., large negative heat of formation of metal oxide, ~550 kJ per mole O). Thus it is expected that the adsorption energy is high for the adsorption of aluminum on ZrO_2 (001) surface, which is terminated by a layer of oxygen ions. Actually, for sub-monolayer of adatoms, the adsorption energies are determined by the strength of local chemical bonds formed at the interface, Al-O bonds for the case of sub-monolayer Al on ZrO_2 (001) surface. First-principles calculations were carried out to calculate the adsorption of 0.5 ML Al on c-ZrO_2 (001) surfaces. The results show that Al-O bonding is rather strong, with the adsorption energy of 8.89 eV/Al-adatom or 10.71 J/m^2. Notice that the reported work of separation for the Nb-Al_2O_3 interface,[40] which is known to be a system with an extremely good adherence, is 9.80 J/m^2. It is thus safe to expect that 0.5 ML of Al can "wet" the ZrO_2(001) surface and be appropriately included between Ni thin film and ZrO_2 substrate.

The deposition of the ultra-thin metal layers was performed in a multiple-chamber ultrahigh-vacuum (UHV) sputtering system with a base pressure of 5.0×10^{-10} mbar. Firstly, 0.5 ML of Al was deposited on clean YSZ(001) surface, which was followed by covering 5 nm thick Ni thin film. Then, 5 nm thick Ta film was deposited to cap the Ni-Al-YSZ(001) interface, which can efficiently preclude the oxygen diffusion into the interface after the exposure of the sample to air. After moving the sample to XPS chamber, the Ta cap layer and its oxide (the upper layer of Ta was oxidized after its exposure to the air.) was removed by Ar^+ ions sputtering, which was monitored by XPS measurement. XPS measurements were performed in a VG ESCALAB 220i-XL system using a monochromatic Al $K_{\alpha 1}$ source (1486.6 eV). The pass energy of

analyzer was set to 10 eV to have high measurement accuracy. The binding energy scale was calibrated with pure gold, silver and copper by setting the Au $4f_{7/2}$, Ag $3d_{5/2}$ and Cu $2p_{3/2}$ at binding energy of 83.93 eV, 368.26 eV and 932.67 eV, respectively.

Figures 5.11 and 5.12 show the survey spectra for Ni-Al(0.5 ML)-YSZ(001) and Ni-YSZ (001) stacks respectively. The small peak around 118.0 eV corresponds to the Al 2s, as indicated by the arrow in Fig. 5.11. The peak adjacent to Al 2s in the lower energy of 111.0 eV is for Ni 3s, as shown in the same energy position in Fig. 5.12. The intensity of Al 2s peak is so weak that it almost pushes to the resolution limit of XPS instrument. Therefore the chemical state (metallic or oxidized) of the interfacial Al atoms cannot be identified from the XPS spectra. The weak intensity of Al 2s spectra is due to the small amount of Al and the attenuation of the signal through the upper Ni layer. For a comparison, the survey spectra for Ni-YSZ(001) interface without interfacial layer is shown in Fig. 5.12. The two spectra are identical except the additional Al 2s spectra for Ni/Al(0.5 ML)/ZrO_2 stacks in Fig. 5.11. The existence of Al at the interface is obvious.

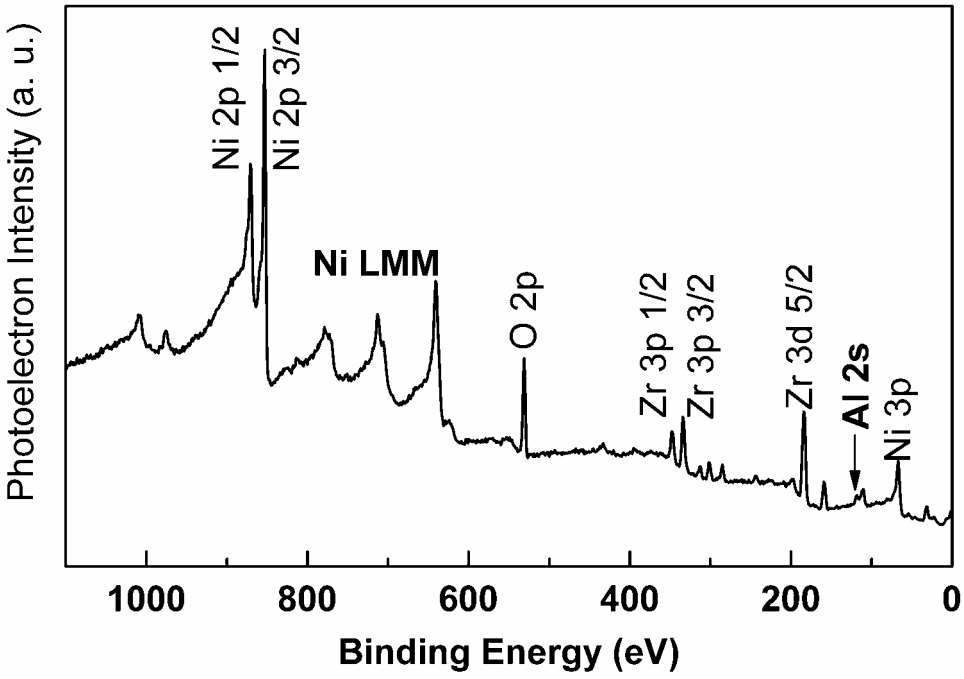

Fig. 5.11 Survey spectra for 4 nm thick Ni-Al (0.5 ML)-YSZ (001) interfaces.

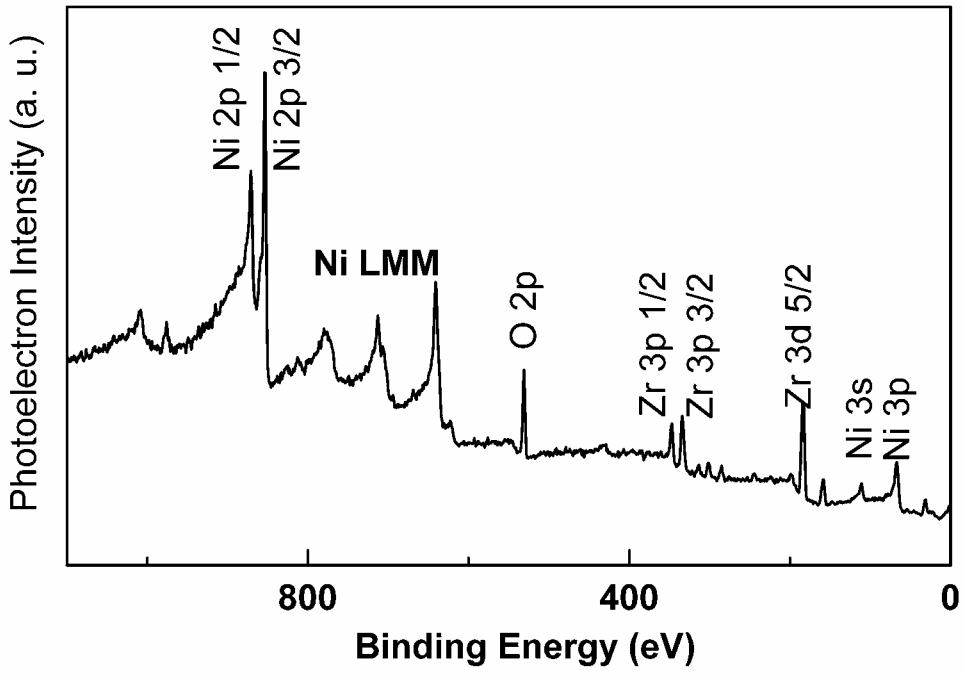

Fig. 5.12 Survey spectra for 4 nm thick Ni on YSZ (001) interfaces.

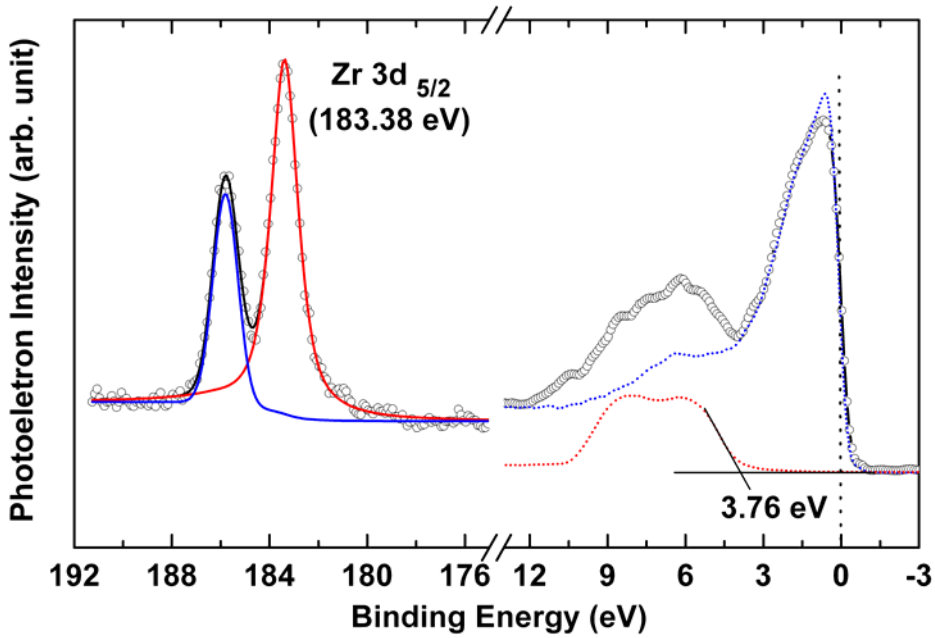

Fig. 5.13 XPS spectra for Zr 3d and valence band for 4 nm thick Ni-Al (0.5 ML)-YSZ (001) interfaces. The dotted lines show the valence bands for Ni bulk and YSZ(001) substrate respectively. The Fermi level is at energy zero.

The *p*-type Schottky barrier height was evaluated by the core-level-based method [41] as introduced in Chapter 4. One recalls that the energy difference between the energy position of Zr $3d_{5/2}$ peak and the leading edge of the valence bands ($\Delta E = E_{Zr-3d5/2} - E_{VBM}$, 179.62 ± 0.05 eV in this case of Ni on ZrO_2 substrate.) can be viewed as a bulk property with no relation to the surface status or the overlayer on the ZrO_2 surface. Then, the *p*(*n*)-type Schottky-barrier height Φ_p (Φ_n) can be obtained using the simple equations

$$\Phi_p = (E_{Zr-3d5/2})_{Ni/ZrO_2} - \Delta E \tag{5.3}$$

and

$$\Phi_n = E_g - \Phi_p \tag{5.4}$$

where $(E_{Zr-3d5/2})_{Ni/ZrO_2}$ is the peak position of Zr 3d core level spectra in Ni/*m*/ZrO_2 stack, E_g the band gap of ZrO_2 (5.80 eV for the ZrO_2 sample in our experiment).

Figure 5.13 shows the Zr 3d and valence band spectra for the 4 nm Ni-Al (0.5 ML)-YSZ (001) interfaces. The dotted lines show the valence bands for Ni bulk and YSZ(001) substrate respectively. The Fermi level is at energy zero. One can see the valence band spectra for Ni bulk is slightly sharper than that for Ni ultrathin film on YSZ substrate. This is due to the small contribution from the interfacial Al layer. The *p*-type SBH was evaluated to be 3.76 ± 0.05 eV by using Eq. (5.3) and was check by decomposing the valence band of the stack to that of Ni and ZrO_2 components, as shown in Fig. 5.13. The inclusion of half monolayer of Al between Ni and ZrO_2 dramatically changes the band alignment between metal and oxide, from 2.60 eV for Ni/ZrO_2 interface to 3.76 eV for Ni/Al(0.5 ML)/ZrO_2 interface. Furthermore, the measured SBH (3.76 eV) for Ni/Al (0.5 ML)/ZrO_2 interface is in good agreement with the calculated value (3.62 eV). Considering the accuracy of the experimental and calculation methods (both around 0.1 eV), this consistency is rather satisfying and serves as a strong evidence that the band alignment between high-*k* dielectric and metal gate can be tuned chemically by including only half monolayer of heterovalent metal at the interface.

Table 5.2 summarizes the experimental and calculated values of SBHs for Ni-ZrO_2(001) interfaces with different interfacial chemical compositions and interface coverage. For Ni-ZrO_2(001) interface with no heterovalent interfacial metal, the experimental SBH takes a value between that of one monolayer coverage of Ni and that of half monolayer. One possible reason is that Ni-Ni(0.5 ML)-ZrO_2 and Ni-Ni(1 ML)-ZrO_2 have similar interface formation energies so that the actual interface

structure takes a coverage between 0.5 and 1. So the resultant SBH takes an average. For the chemical tuning effects, the most important feature here is that the inclusion of a layer of low work function metal (Al) between high work function metal (Ni) and gate dielectric could tune the effective work function of metal gate or SBH up to ~ 1.2 eV. This experimentally and theoretically proven tuning ability is of great importance. It provides not only a practical way of modifying the band alignments for metal gate/high-κ oxide interfaces to satisfy the engineering requirement for the metal gate technology, but also fundamental understanding of the metal gate/high-*k* dielectric interfaces on the atomic scale.

Table 5.2 Comparison of calculated (DFT-GGA) and XPS experimental values of Schottky barrier heights for Ni-*m*-ZrO_2 (*m*= Ni or Al) interfaces.

Structure	Coverage	Method	Φ_P (eV)	Φ_n (eV)
	0.5	DFT-GGA	3.02	2.76
Ni-ZrO_2	1	DFT-GGA	2.17	3.63
	0.5~1	XPS	2.60	3.20
	0.5	DFT-GGA	3.62	2.18
Ni-Al-ZrO_2	1	DFT-GGA	4.98	1.82
	~0.5	XPS	3.76	2.04

5.5 Chapter summary

In conclusion, chemical tuning of the band alignment for Ni-ZrO_2 interfaces by introducing heterovalent metal interlayer has been studied using first-principles calculations. A remarkable tuning range (2.8 eV) for effective metal work function ($\Phi_{m,eff}$) was achieved theoretically. Furthermore, a general chemical tuning trend was established for most of the transition metals considered, that is, $\Phi_{m,eff}$ increases linearly with the electronegativity of the interfacial metal atom. Although the complicated situations in real metal gate/dielectric oxides interfaces limit the predictive power of our results, the simple linear relationship between $\Phi_{m,eff}$ and the electronegativity of interfacial metal atom would provide a valuable guide in tuning the effective work function of metal gate on high-*k* dielectric. In addition, this chemical tuning effect was demonstrated by Ni/Al/ZrO_2 interface experimentally. The XPS observed values for SBH was tuned up to ~1.2 eV by including only a layer of Al metal at the interface, in good agreement with the predicted magnitude.

References

[1] The International Technology Roadmap for Semiconductor 2005, URL: http://public.itrs.net.

[2] G. D. Wilk, R. M. Wallace, and J. M. Anthony, J. Appl. Phys. **89**, 5243 (2001).

[3] S. J. Wang and C. K. Ong, Appl. Phys. Lett. **80**, 2541 (2002).

[4] P. W. Peacock and J. Robertson, Phys. Rev. Lett. **92**, 057601 (2004).

5 C. J. Först, C. R. Ashman, K. Schwarz, and P. E. Blöchl, Nature (London) **427**, 53 (2004).

[6] Y. F. Dong, Y. P. Feng, S. J. Wang, and A. C. H. Huan, Phys. Rev. B **72**, 045327 (2005).

[7] Yee-Chia Yeo, Tsu-Jae King, and Chenming Hu, J. Appl. Phys. **92**, 7266 (2002).

[8] V. V. Afanas'ev, M. Houssa, A Stesmans, and M. M. Heyns, J. Appl. Phys. **91**, 3079 (2002).

[9] Y. F. Dong, S. J. Wang, J. W. Chai, Y. P. Feng, and A. C. H. Huan, Appl. Phys. Lett. **86**, 132103 (2005).

[10] I. De, D. Johri, A. Srivastava, and C. M. Osburn, Solid-State Electron. **44**, 1077 (2000).

[11] A. A. Knizhnik, I. M. Iskandarova, A. A. Bagatur'yants, B. V. Potapkin, and L. R. C. Fonseca, J. Appl. Phys. **97**, 064911 (2005).

[12] Y. F. Dong, S. J. Wang, Y. P. Feng, and A. C. H. Huan, Phys. Rev. B **73**, 045302 (2006).

[13] G. Kresse and J. Hafner, Phys. Rev. B **47**, R558 (1993); G. Kresse and J. Hafner, Phys. Rev. B **48**, 13115 (1993).

[14] G. Kresse and J. Furthmuller, Comput. Mater. Sci. **6**, 15 (1996); G. Kresse and J. Furthmuller, Phys. Rev. B **54**, 11169 (1996).

[15] D. Vanderbilt, Phys. Rev. B **41**, R7892 (1990).

[16] J. P. Perdew, J. A. Chevary, S. H. Vosko, K. A. Jackson, M. R. Pederson, D. J. Singh, and C. Fiolhais, Phys. Rev. B **46**, 6671 (1992).

[17] Peter E. Blöchl, O. Jepsen, and O. K. Andersen, Phys. Rev. B **49**, 16223 (1994).

[18] A. Christensen and E. A. Carter, J. Chem. Phys. **114**, 5816 (2001).

[19] G. Bordier and C. Norguera, Phys. Rev. B **44**, 6361 (1991).

[20] R. T. Tung, Mater. Sci. and Eng. R **35**, 1 (2001).

[21] J. Goniakowski and C. Noguera, Interface. Sci. **12**, 93 (2004).

[22] J. Tersoff, Phys. Rev. Lett **52**, 465 (1984).

[23] S. G. Louie, J. R. Chelikowsky, and M. L. Cohen, Phys. Rev. B **15**, 2154 (1977).

[24] John Robertson, J. Vac. Sci. Technol. B **18**, 1785 (2000).

[25] Winfried Mönch, Appl. Phys. Lett. **86**, 122101 (2005).

[26] M. Peressi, N. Binggeli, and A. Baldereschi, J. Phys. D **31**, 1273 (1998).

[27] S. H. Wei and A. Zunger, Phys. Rev. Lett. **59**, 144 (1987).

[28] B. Králik, E. K. Chang, and S. G. Louie, Phys. Rev. B **57**, 7027 (1998).

[29] V. Fiorentini and G. Gulleri, Phys. Rev. Lett. **89**, 2661011 (2002).

[30] S. J. Wang, A. C. H. Huan, Y. L. Foo, J. W. Chai, J. S. Pan, Q. Li, Y. F. Dong, Y. P. Feng, and C. K. Ong, Appl. Phys. Lett. **85**, 4418 (2004).

[31] M. D. Segall, P.L. D. Lindan, M. J. Probert, C. J. Pickard, P. J. Hasnip, S. J. Clark, and M. C. Payne, J. Phys.: Condens. Matter **14**, 2717 (2002).

[32] R. G. Pearson, Inorg.Chem **27**, 734 (1988); R. S. Mulliken, J. Chem. Phys. **2**, 782 (1934).

[33] H. B. Michaelson, J. Appl. Phys. **48**, 4729 (1977).

[34] R. T. Tung, Phys. Rev. Lett. **84**, 6078 (2000).

[35] Seongjun Park, Luigi Colombo, Yoshio Nishi, and Kyeongjae Cho, Appl. Phys. Lett. **86**, 073118 (2005).

[36] D. A. Ricci, T. Miller, and T.-C. Chiang, Phys. Rev. Lett. **93**, 136801 (2004).

[37] Andreas Eichler and Georg Kresse, Phys. Rev. B **69**, 045402 (2004).

[38] V. E. Henrich, P. A. Cox, *The surface Science of Metal Oxides* (Canbridge University Press, Cambridge, 1994)

[39] C. T. Campbell, Surf. Sci. Rep. **27**, 1 (1997).

[40] Y.F. Zhukovskii, E.A. Kotomin, P.W.M. Jacobs, and A.M. Stoneham, Phys. Rev. Lett. **84**, 1256 (2000).

[41] S. A. Chambers, Y. Liang, Z. Yu, R. Droopad, J. Ramdani, and K. Eisenbeiser, Appl. Phys. Lett. **77**, 1662 (2000).

Chapter 6

Concluding remarks

6.1 Conclusion

In this research, various characterization techniques and first principles calculations based on density functional theory were used as tools in exploring how the atomic-level interface structures affect the properties of metal gate/high-*k* dielectric oxide/Si stacks. Crystalline ZrO_2 and Ni were used as the prototypes for high-*k* gate dielectric and metal gate respectively.

For high-*k* dielectric oxide/Si interfaces, epitaxial ZrO_2 on silicon structures have been studied as alternative gate dielectric, including film growth, interface characterization, and electronic structure calculations. Using a combinational characterization tools, including high-resolution transmission electron microscopy (HRTEM), and X-ray photoelectron spectroscopy (XPS), in conjunction with first-principles calculations based on the density functional theory (DFT), the interfacial atomic structure and band discontinuity at the ZrO_2/Si interfaces were studied. The HRTEM images show that the crystalline interface has a high symmetry cube-on-cube epitaxial structure with no interfacial amorphous silica or silicate layers between the metal oxide and Si substrate. The epitaxial interfaces also have sufficient band offsets for carrier barriers. Such structure could fundamentally change the scaling laws for the silicon-based transistor technology by virtue of its higher dielectric constant.

Various ZrO_2/Si interface structures based on the HRTEM images have been proposed. The results for the calculation of interface formation energy show that Zr-terminated interfaces only exist in metal-rich atmosphere. The electronic structures of the various interfaces were also discussed to verify the general bonding rules for constructing insulating interfaces without gap states, which is a key criterion for high-*k* applications. The calculated band offsets were compared with the experimental values. The strain modes (free-standing and Si-substrate mode) effects and interface structure effects on band offsets were discussed. The band offsets are found strongly dependent on the strain modes and interface structures. The results show that in epitaxial growth of ZrO_2 on Si for gate dielectric applications, the chemical environment should be carefully controlled to get desired and reproducible band offsets.

For metal gate/high-*k* dielectric interfaces, high-quality fcc-Ni was grown epitaxially on yttrium-stabilized cubic ZrO_2(001) surfaces in ultrahigh vacuum (UHV). The epitaxial relationship was determined by *ex situ* high resolution TEM (HRTEM) to be Ni(001)//ZrO_2(001) and Ni[110]//ZrO_2[100]. *In-situ* x-ray photoemission methods were applied to accurately determine the Schottky barrier height for Ni/ZrO_2(001) interfaces. It was found that band alignment between Ni and ZrO2 is strongly dependent on the interface structures and O-rich interface has a lower SBH than O-deficient interface (2.60 eV vs. 3.36 eV). Such interface dependence of SBH was further investigated by first-principles calculations for three types of Ni/ZrO_2 model interfaces: O-*t* interface full of Ni-O interfacial bonds, Zt-*t* interface full of Ni-Zr interfacial bonds, and interfaces incorporating oxygen vacancies (O-*v*). The interface dipole formed by Ni-O bonds at the interface tends to decrease p-type SBH, while Ni-Zr bonds or oxygen vacancies at the interface increasing it. The results show that the

SBH at Ni/ZrO_2 can be engineered for the metal gate application in CMOS devices through the interface structure-control.

A novel method for chemical tuning of the band alignment for Ni-ZrO_2 interfaces has been proposed by introducing heterovalent metal interlayer. A remarkable tuning range (2.8 eV) for effective metal work function ($\Phi_{m,eff}$) was achieved theoretically. Furthermore, a general chemical tuning trend was established for most of the transition metals considered, that is, $\Phi_{m,eff}$ increases linearly with the electronegativity of the interfacial metal atom. Although the complicated situations in real metal gate/dielectric oxides interfaces limit the predictive power of our results, the simple linear relationship between $\Phi_{m,eff}$ and the electronegativity of interfacial metal atom would provide a valuable guide in tuning the effective work function of metal gate on high-*k* dielectric. In addition, this chemical tuning effect was demonstrated by Ni/Al/ZrO_2 interfaces experimentally. The XPS observed values for SBH was tuned up to ~1.2 eV by including only a layer of Al metal at the interface, in good agreement with the predicted magnitude.

6.2 Future works

We readily acknowledge that our study is only based on prototypes of metal gate and high-*k* oxide materials, *e.g.*, crystalline interfaces at metal gate/high-*k* oxide/silicon stacks, which represent ideal situations compared with the much more complicated situations in real metal gate and high-*k* materials applications. Future work would be needed to identify to what extent the results (e.g., the dependence of band alignments on interface structures) found here can be applied to amorphous metal

gate and high-*k* oxide materials. For example, as a first approximation, the non-polar interfaces between the most abundant high-*k* oxide and metal surfaces, such as Ni (111) and ZrO_2 (111) surface, could be studied. Our preliminary studies[1] have shown that non-polar Ni(111)/HfO_2(111) interface has much weaker interface tension (at least five times smaller) than that for polar Ni(001)/HfO_2(001) interface, which already indicate different types of interface interaction for polar and non-polar metal gate/high-*k* interfaces. This would have significant effects on the interface electronic structures and properties. Further studies to explore the chemical tuning effects for non-polar metal gate/high-*k* interfaces are highly recommended.

Further studies may also extend the present work for defect-free interfaces to study the interfaces incorporating defects, *e.g.*, oxygen vacancies,[2, 3] hydrogen-related defects,[4] and their complex. It is well known that high-*k* dielectric material have much more defects than SiO_2 and the defects at high-*k* oxide/silicon interfaces heavily degrade the channel mobility.[5] But the physical mechanism behind this mobility degrading is not clear yet. In addition, to couple the oxygen vacancies at high-*k* oxide and preclude the substantial formation of interfacial silicon oxide layer, nitridation of high-*k* oxide is being intensively studied[6,7] Therefore, further studies to explore the role of incorporation of nitrogen at high-*k* dielectric/silicon interfaces would also be an interesting subject.

References

[1] Q. Li, Y. F. Dong, S. J. Wang, A. C. H. Huan, Y. P. Feng, and C. K. Ong, *Appl. Phys. Lett.* **88**, 222102 (2006).

[2] A. S. Foster, F. Lopez Gejo, A. L. Shluger, and R. M. Nieminen, Phys. Rev. B **65**, 174117 (2002).

[3] Y. P. Feng, A. T. L. Lim, and M. F. Li, Appl. Phys. Lett. **87**, 062105 (2005).

[4] Joongoo Kang, E.-C. Lee, K. J. Chang, and Young-Gu Jin, Appl. Phys. Lett. **84**, 3894 (2004).

[5] J. Robertson, Eur. Phys. J. Appl. Phys. **28**, 265 (2004).

[6] S. Sayan, N. V. Nguyen, and J. Ehrstein, *et al.*, Appl. Phys. Lett. **87**, 212905 (2005).

[7] Satoshi Toyoda, Jun Okabayashi, and Haruhiko Takahashi, *et al.*, Appl. Phys. Lett. **87**, 182908 (2005).